Designing singularities in electronic dispersions

Designing singularities in electronic dispersions

A dissertation presented

by

Oleksandr Shtyk

to

The Department of Physics

in partial fulfillment of the requirements

for the degree of

Doctor of Philosophy

in the subject of

Physics

Harvard University

Cambridge, Massachusetts

June 2018

Dissertation Advisor:
Claudio Chamon

Author:
Oleksandr Shtyk

Designing singularities in electronic dispersions

Abstract

This dissertation is devoted to the study of singularities in electronic dispersions and their implications for electronic systems.

First, we consider two-dimensional interacting electrons at a monkey saddle with dispersion $\propto p_x^3 - 3p_x p_y^2$. Such dispersion naturally arises as a singularity when three van Hove saddles merge in an elliptical umbilic elementary catastrophe and can be interpreted as a multicritical Lifshitz point. It can be realized in biased bilayer graphene and can be identified by its signature Landau level behavior $E_m \propto (B_m)^{3/2}$ and related oscillations in thermodynamic and transport properties, such as Shubnikov-de Haas oscillations, whose period triples as the system crosses the singularity. We show, in the case of a single monkey saddle, that the non-interacting electron fixed point is unstable to interactions under the renormalization group flow, developing either a superconducting instability or non-Fermi liquid features. Biased bilayer graphene, where there are two non-nested monkey saddles at the K and K' points, exhibits an interplay of competing many-body instabilities, namely $s-$wave superconductivity, ferromagnetism, and spin- and charge-density wave.

Next, we show that electronic bands in silicon have nontrivial topological structures that are captured by a network of Berry flux lines. These flux lines link at points of high symmetry in the Brillouin zone, forming singular ice-nodal points where fluxes satisfy ice rules, making silicon a "nodal-chain insulator". This complex Berry-flux network implies a topologically stable two-fold degeneracy along the X-W direction in all of silicon bands. Similarly to nodal-chain semimetals, we find drumhead-like states in the regions that are delimited by the projections of the bulk Berry flux network on the surface Brillouin zone.

Finally, we discuss Meissner effect in a nonequilibrium superconducting state. By carefully tuning the system so as to match electron and hole velocities, a singularity in the effective density of states can be achieved leading to a strong non-BCS pairing. We calculate the superfluid density for such a nonequilibrium paired state, and find it to be positive for repulsive interactions and interband pairing. The positivity of the superfluid density implies the stability of the photo-induced superconducting state as well as the existence of the Meissner effect.

Contents

List of Tables

List of Figures

Introduction

Generally, as we vary a single parameter of the system such as temperature or pressure, we expect to encounter only a simple phase transition between two phases of matter. Only when we start controlling at least two parameters we can hope to find special points, where more than two phases coexist together. A bright illustration can be given by water. A first set of examples of phase transitions, known to humanity from the dawn of times for at least several million years [1], long before the creation of foundations of thermodynamics or the conception of the idea of phase transition itself, are melting of ice and freezing of water. Both are observed as seasons change and during travels across different climatic regions. A second set of examples is ubiquitous in the life of a modern human and is a boiling of water and condensation of water vapor. It is safe to assume this phase transition of water didn't become pervasive until the advent of sophisticated cooking, at least 50000 years ago [2, 3]. Finally, it is not until year 1873 that J. Thomson predicted existence of triple points, where solid, liquid and gaseous states coexist [4].

Similarly to controlling temperature and pressure in water, having control over several experimental "knobs" allows to achieve novel exotic electronic dispersions and properties. As we explain in the abstract, we study three systems: bilayer graphene, silicon and optically-pumped semiconductor, each exhibiting singularity of their own kind: monkey saddle, ice nodal points of crossing Berry flux lines, and an effectively flat dispersion. In the end of the first chapter we also discuss layered perovskite metal $Sr_3Ru_2O_7$ with a singularity of the X_9 type. Beside the systems discussed in the present text, a bright recent example was dubbed "twistronics" [5]: instead of controlling interlayer voltage bias in bilayer graphene, as we

suggest in the first chapter, one can control the angle between two sheets of graphene [6]. Certain "magic" angles result into formation of intrinsic unconventional superconductivity with a rather high transition temperature.

Scientific progress in recent years enabled incredible control over the properties of materials. Material engineering allows for atom-by-atom construction of electronic quantum devices [7], while cold atomic systems allow precise engineering of not only the underlying optical lattice, but also of inter-atomic interactions through the Feshbach resonance [8, 9]. We believe that ideas presented in this thesis can be generalized to other systems, perhaps by designing a layered system with higher order singularities in electronic dispersions. After all, the monkey saddle realized in bilayer graphene is a D_4^- elementary catastrophe, a *simplest* example of a cubic singularity!

Chapter 1

Monkey saddle in bilayer graphene

1.1 Introduction

Systems of two-dimensional (2D) electrons close to van Hove (vH) singularities [10, 11, 12, 13, 14, 15, 16, 17, 18] are of interest because of their displayed logarithmic enhancement of the electron density of states (DoS), which translates into a propensity to many-body instabilities[10]. Among many exciting possibilities opened by proximity to vH singularities is that unconventional $d + id$ chiral superconductivity could occur in strongly doped graphene monolayer [19].

The transition of the Fermi level through a vH singularity can be interpreted essentially as a Lifshitz transition of a neck-narrowing type [20], wherein two disconnected regions of the Fermi surface (FS) merge together. Alternatively, if the touching occurs at the edge of the Brillouin zone, as it happens for the square lattice, it may be interpreted as a FS turning inside out (from electron-like to hole-like). A multicritical Lifshitz point (MLP) arises as both a crossing of several Lifshitz transition lines, and as a singularity in the electronic dispersion $\xi(\boldsymbol{p})$. MLPs of bosonic type have been analyzed and classified in the context of phase transitions, where terms in the free-energy-density functional with higher-order derivatives of an order parameter, say the magnetization, need to be kept at special points in the phase diagram [21, 22, 23]. Yet, MLPs of fermionic type, with a singularity in the

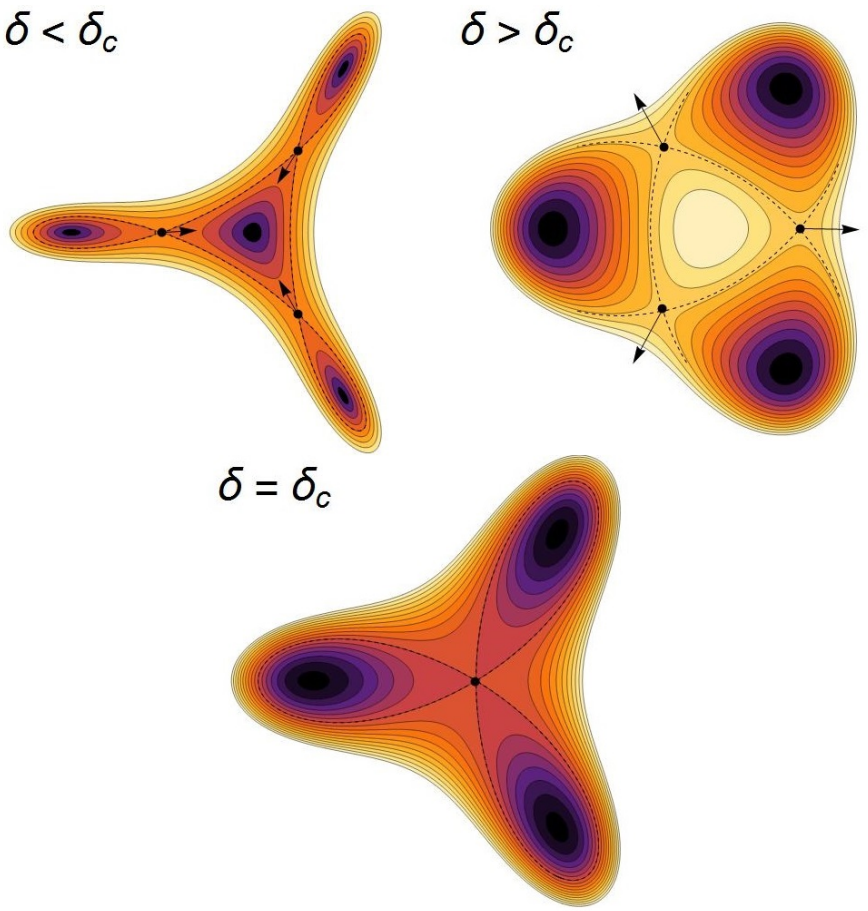

Figure 1.1: *Pictorial representation of Fermi surface families in a biased bilayer graphene system for three different values of the interlayer voltage bias δ. Three van Hove saddles with dispersions $\propto (p_x^2 - p_y^2)$ are shown with black dots ($\delta \neq \delta_c$) while arrows indicate their displacement upon increasing the value of δ. At the critical value of the bias δ_c they merge into a monkey saddle $\propto (p_x^3 - 3p_x p_y^2)$ that closes into a trifolium-shaped Fermi surface.*

fermionic dispersion $\xi(\boldsymbol{p})$, have been largely unexplored, only in a scenario involving Majorana fermions and spin liquids [24].

In this chapter we study fermionic MLPs, using biased bilayer graphene (BLG) as a concrete example of a physical realization. In the case of BLG, three vH saddles merge into a monkey saddle at critical value of the interlayer voltage bias (see Fig. 1.1 and Fig. 1.2 on page 7). Mathematically, the monkey saddle is a genuine mathematical singularity with a degenerate quadratic form as opposed to vH saddle, which is not a true singularity in a mathematical sense, having a non-degenerate quadratic form of the $(+-)$ signature,

$\propto p_x^2 - p_y^2$. Physically, we identify key differences between the case of a MLP and that of the usual vH singularity. First, the monkey-saddle-like dispersion $\propto p_x^3 - 3p_x p_y^2$ at the MLP exhibits a stronger, power-law divergence in the DoS and thus leads to even stronger many-body instabilities, with higher transition temperatures as a result. These stronger DoS divergences greatly simplify the renormalization group (RG) analysis of the problem, yielding a super-renormalizable theory. We find that the non-interacting electron fixed point is unstable to interactions, developing either a superconducting instability or non-Fermi liquid behavior. In the case of BLG, which has two non-nested monkey saddles at the K and K' points, interactions lead to instabilities to s-wave superconducting state, ferromagnetism, spin-, and charge density wave, depending on the nature of interactions. Second, the monkey saddle possesses a signature Landau level (LL) structure with energy levels $E_m \propto (Bm)^{3/2}$. In addition, oscillations in different thermodynamic and transport properties, such as de Haas-van Alphen and Shubnikov de Haas oscillations, for example, are sensitive to the presence of the multicritical point. The monkey saddle can be identified by the scaling of the period of these oscillations with the Fermi energy as $\Delta(1/B) \propto E_F^{2/3}$ and with an abrupt tripling of the period as Fermi level goes from below to above the saddle, due to a change of the FS topology.

The presentation of the results in this chapter is organized as follows. In Sec. 1.2 we present how the monkey saddle arises in voltage-biased BLG. We show how four different FS topologies can be attained by varying the bias voltage and the chemical potential, and identify the MLP in the phase diagram as the location where these four different phases meet at a point. There we also discuss the nature of the divergence in the density of states for the monkey saddle dispersion. In Sec. 1.3 we obtain the energies of the quantized Landau orbits within a quasiclassical approximation, and present arguments for the period tripling of the magnetic oscillations as the system undergoes a FS topology change; these features may serve as clear experimental telltales of the MLP in BLG. In Sec. 1.4 we give a lightning-quick introduction to imaginary path integral formalism and define an electron polarization operator. In Sec. 1.5 we present an RG analysis of the case when interactions

are present in a system with an isolated monkey saddle, where we show that the system is either unstable to superconductivity or flows to a non-Fermi liquid, depending on the sign of the interactions. The RG analysis for the case of BLG with two monkey saddles at the K and K' points is studied in Sec. 1.6, where we discuss the possible instabilities of the system. In Sec. 1.7 we discuss a another material,layered perovskite metal $Sr_3Ru_2O_7$, and argue that some of its unusual thermodynamic properties can be explained by the singularity in electronic dispersion. We close the chapter by summarizing the results and discussing open problem in Sec. 1.8.

1.2 Hamiltonian and dispersion

Here we explicitly show how the monkey saddle arises in BLG. We consider AB-type stacked BLG, with the layers labeled by 1 and 2, and the two sublattices within each layer labeled by A and B. The spinor representing the electronic amplitudes is chosen in the order $(A1, B1, A2, B2)$. We consider an extended tight-binding model that includes next-nearest neighbor hopping, where the Hamiltonian of the system linearized near the K point is [25]

$$\check{H}_0 = \begin{pmatrix} \frac{1}{2}V & vp_- & 0 & v_3p_+ \\ vp_+ & \frac{1}{2}V & \gamma_1 & 0 \\ 0 & \gamma_1 & -\frac{1}{2}V & vp_- \\ v_3p_- & 0 & vp_+ & -\frac{1}{2}V \end{pmatrix}. \tag{1.1}$$

Here v is the band velocity of monolayer graphene, $\gamma_1 = 0.4$ eV is an interlayer coupling constant and $v_3 \approx 0.1v$ describes trigonal warping that arises as a result of the next-nearest-neighbor hopping. V is an interlayer voltage bias and $p_\pm = p_x \pm ip_y$ is the momentum. BLG has four energy bands and in this thesis we are focused solely on the lowest upper band with an electron dispersion [26]

$$\xi^2(\boldsymbol{p}) = \frac{V^2}{4}\left(1 - 2\frac{v^2p^2}{\gamma_1^2}\right)^2 + v_3^2p^2 + 2\frac{v_3v^2}{\gamma_1}p^3\cos 3\phi + \frac{v^4p^4}{\gamma_1^2}. \tag{1.2}$$

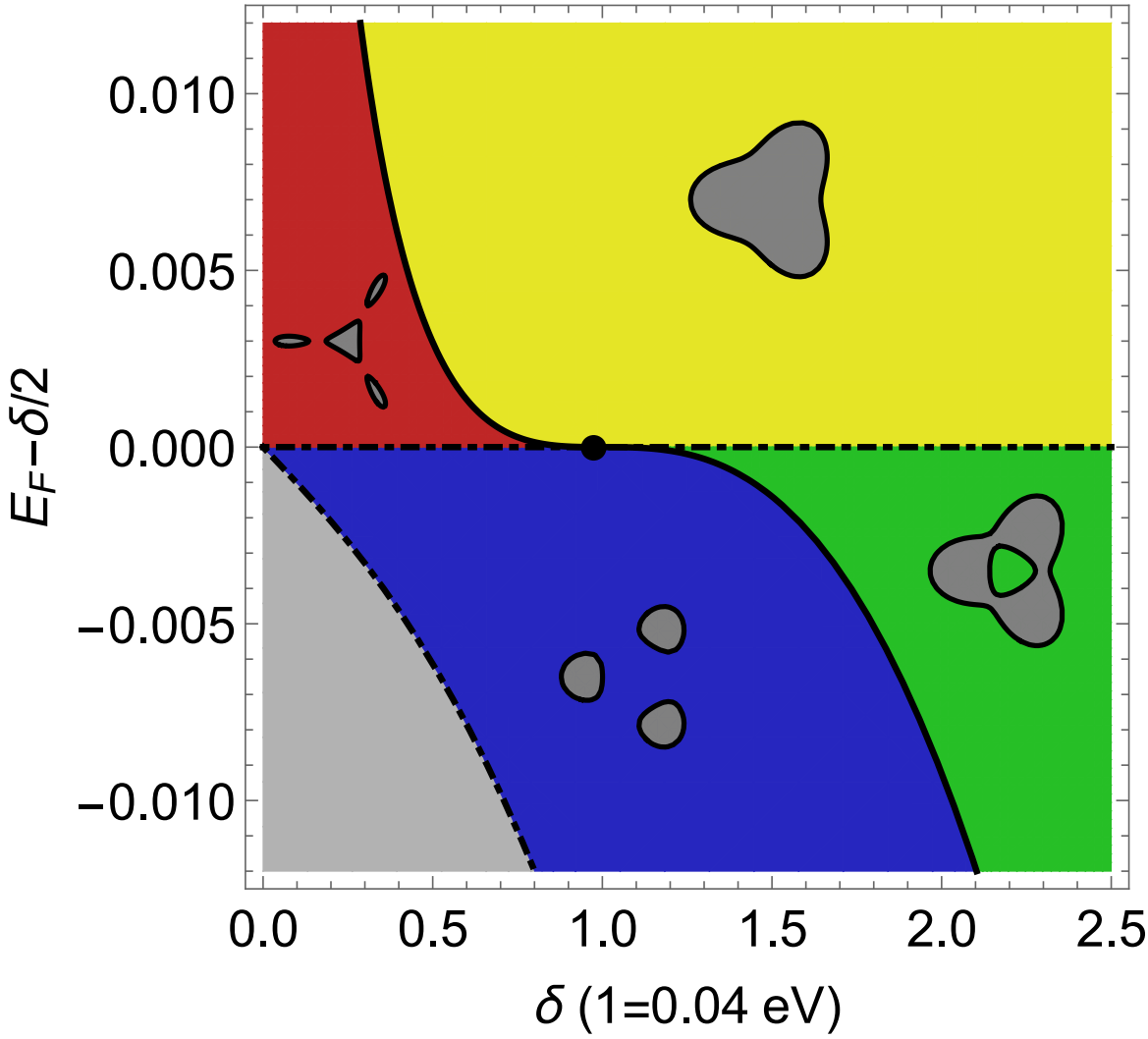

Figure 1.2: *There are four phases with different Fermi surface topologies in biased bilayer graphene. They are separated by two lines of phase transitions, one of a band-edge type (dash-dotted) and the other of the van Hove or equivalently a neck-narrowing type (solid). The multicritical Lifshitz point is located at the crossing of these two lines. In the gray area the Fermi level lies within the gap with no FS. Note different scales for the voltage δ and the Fermi energy E_F.*

For voltage biases V of the order of the trigonal warping energy scale γ_1 the $\propto p^4$ contribution arising from the first term can be safely neglected. It is convenient to introduce dimensionless variables, redefining energies as $\xi \to (v_3\gamma_1/v)\xi$ and momenta as $\boldsymbol{p} \to (v_3\gamma_1/v^2)\boldsymbol{p}$,

$$\xi^2(\boldsymbol{p}) = (\delta/2)^2 + u_3^2\left[(1-\delta^2)p^2 + 2p^3\cos 3\phi + p^4\right], \tag{1.3}$$

where $u_3 \equiv v_3/v \approx 0.1$ is a dimensionless measure of the warping strength and $\delta \equiv V/(v_3\gamma_1/v)$. The dispersion near the K' point can be obtained from the one near the K point by inversion, $\boldsymbol{p} \to -\boldsymbol{p}$.

Unlike in the case of a monolayer graphene, where the warping merely distorts the Dirac cone with low-energy dispersion unaffected, BLG behaves in a very different way. In the absence of interlayer voltage bias, the trigonal warping destroys the parabolic dispersion, breaking it down into four Dirac cones. A non-zero interlayer voltage V gaps out these Dirac cones while also gradually inverting the central electron pocket into a hole-like pocket at the critical value of the bias $V_c = (v_3/v)\gamma_1$ ($\delta_c = 1$ in dimensionless units introduced above). This critical value of the bias marks a singularity in the electronic dispersion $\xi(\boldsymbol{p})$.

At the subcritical interlayer voltage bias $\delta < 1$ the electronic dispersion $\xi(\boldsymbol{p})$ has seven extremal points, four electronic pockets and three vH saddle points. While the three outer electronic pockets are robust and are present at all voltage biases, the central extremum and three vH saddle points merge at the critical voltage falling apart again into three saddles and a hole-like pocket at the supercritical bias $\delta > 1$, see Fig. 1.1.

1.2.1 Monkey saddle as a D_4^- singularity

In the vicinity of the singular point, the behavior of the electronic dispersion is governed by the lowest powers of the momentum:

$$\xi(\boldsymbol{p}) \propto \underbrace{(1-\delta^2)p^2}_{\text{Pert(2,1)}} + \underbrace{p^3\cos 3\phi}_{\text{CG(2)}}. \tag{1.4}$$

This momentum behavior corresponds exactly to the symmetry-restricted elliptic umbilic elementary catastrophe (D_4^- within ADE classification) [27]. From the point of view of the

catastrophe theory the cubic term $p^3 \cos 3\phi \equiv$ CG(2) is a catastrophe germ defining the nature of the singularity in $\xi(\boldsymbol{p})$ function, while the quadratic term $(1-\delta^2)p^2 \equiv$ Pert(2,1) is a lattice-symmetry restricted perturbation, with one parameter δ, which regularizes the singularity. Qualitatively the behavior of the system can be viewed as a bifurcation of a monkey saddle $p^3 \cos 3\phi \equiv p_x^3 - 3p_x p_y^2$ into three vH(ordinary) saddles and a maximum/minimum:

$$\underbrace{p_x^3 - 3p_x p_y^2}_{\text{monkey saddle}} \longleftrightarrow 3 \times \underbrace{(p_x^2 - p_y^2)}_{\text{vH saddle}} + 1 \times \underbrace{p^2}_{\text{e/h pocket}}. \tag{1.5}$$

1.2.2 Fermi surface topology phase diagram

The electron FS at a given Fermi energy is defined as a cross-section of the electron dispersion $\xi(\boldsymbol{p}, \delta) = E_F$. There are four distinct Fermi surface topology phases within the (δ, E_F) plane (see Fig. 1.2). All of them have the same three-fold symmetry but can be discerned by their topological invariants, the number of connected components and the number of holes. Namely, in our case the four phases can be labeled uniquely by the first two Betti numbers of their FS (b_0, b_1) as (1,0), (4,0), (3,0), and (1,1).

These four phases are separated by two lines of topological phase transitions. One of the lines is of a weaker, band-edge transition type, while another is of a stronger vH type (the former has a jump in the DoS while the latter has a log-divergence). The multicritical Lifshitz point lies at the intersection of these two lines.

1.2.3 Divergent density of states

The monkey saddle leads to a strong IR divergence in the DoS. While the vH saddle has a logarithmic DoS, any generic higher order saddle $\xi(\boldsymbol{p}, n) = ap^n \cos n\phi$ has a power-law divergence in the DoS. To obtain the DoS for a higher order saddle, it is convenient to work on generalized hyperbolic coordinates $(\xi, \eta) = a(p^n \cos n\phi, p^n \sin n\phi)$ (where $n = 1, 2$ correspond to polar and hyperbolic coordinates, respectively). The dispersion of the saddle is given by the ξ variable, while η plays the role of the hyperbolic angle, parametrizing

displacements along the FS. The density of states is given by

$$\begin{aligned}\nu(\xi, n) &= \oint_{FS} \frac{(\mathrm{d}\boldsymbol{p})}{\mathrm{d}\xi} = \frac{a^{-2/n}}{(2\pi)^2 n} \int_{-\infty}^{+\infty} \frac{\mathrm{d}\eta}{\left(\xi^2+\eta^2\right)^{\frac{n-1}{n}}} \\ &= \frac{a^{-2/n}}{4n\pi^{3/2}} \frac{\Gamma\left(\frac{1}{2}-\frac{1}{n}\right)}{\Gamma\left(1-\frac{1}{n}\right)} \xi^{-\frac{n-2}{n}},\end{aligned} \tag{1.6}$$

where the $(\mathrm{d}\boldsymbol{p}) \equiv d^2p/(2\pi)^2$, and we set Planck's constant to unit ($\hbar = 1$). The case of the monkey saddle in BLG is $n = 3$, while in Sec 1.7 we discuss layered perovskite $Sr_3Ru_2O_7$ that hosts $n = 4$ saddle.

1.3 Magnetic oscillations at the monkey saddle

Within a quasiclassical approximation, the LLs can be obtained by quantization of the area enclosed by quasiparticle orbit in momentum space,

$$\int (d\boldsymbol{p}) \simeq \frac{m}{2\pi l_B^2}, \tag{1.7}$$

where $l_B = \sqrt{c/eB}$ is a magnetic length and m is the LL index. For a system tuned exactly to the monkey saddle (or any higher order saddle), the behavior is dominated by the singularity itself, so that

$$\begin{aligned}\int_0^{E_m} \nu(\xi) d\xi &= \frac{1}{8\pi^{1/2}} \frac{\Gamma\left(\frac{1}{2}-\frac{1}{n}\right)}{\Gamma\left(1-\frac{1}{n}\right)} \left(\frac{E_m}{a}\right)^{\frac{2}{n}} \\ \implies E_m &= \alpha \left(\frac{a}{l_B^n}\right) m^{n/2} \propto (Bm)^{n/2}\end{aligned} \tag{1.8}$$

with a numerical coefficient

$$\alpha = \left(4\sqrt{\pi} \frac{\Gamma\left(1-\frac{1}{n}\right)}{\Gamma\left(\frac{1}{2}-\frac{1}{n}\right)}\right)^{\frac{n}{2}} \underset{(n=3)}{=} 2.27. \tag{1.9}$$

As is often the case, LLs imply oscillations of various transport and thermodynamic properties in an applied magnetic field, since such oscillations happen as LLs cross the Fermi level of the system. At the critical voltage bias $\delta_c = 1$ but with a small positive detuning from the energy of the saddle point, *i.e.*, E_F slightly higher than $\delta_c/2$, we can see from Eq. (1.8)

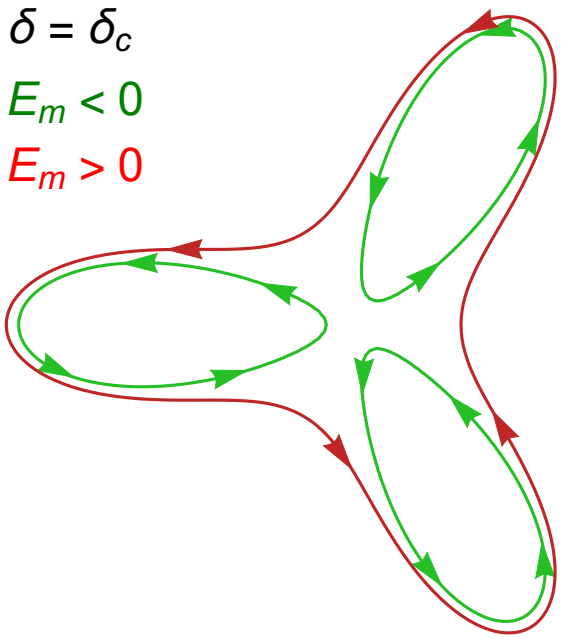

Figure 1.3: *Quasiclassical LL orbits in momentum space for energies slightly below and slightly above the monkey saddle (and critical voltage bias). The number of connected FS components changes from three to one as the Fermi level crosses zero.*

that we have a periodicity in inverse magnetic field with a period

$$\Delta\left(\frac{1}{B}\right) = \frac{e\hbar}{c}\left(\frac{E_F}{\alpha a}\right)^{2/n}, \tag{1.10}$$

where we reinserted Planck's constant $\hbar$.

Eqs. (1.8, 1.10) are given for positive LL energies, when E_F is slightly higher than $\delta_c/2$, and the FS consists of one connected component, see Figs. 1.1, 1.2. The situation is different for negative energies, when E_F is slightly lower than $\delta_c/2$ and the Fermi surface has three disconnected components. In this case the LLs are triply degenerate (on top of the valley degeneracy), and are three times as sparse,

$$E_{-m} = -\alpha a l_B^{-n}(3m)^{n/2}, \tag{1.11}$$

and oscillations period in inverse magnetic field is three times smaller as well. (All equations above are for spinless electrons: in a real system Zeeman splitting should be taken into

account as well.)

The tripling of the periodicity of oscillation is a telltale of the Fermi surface topology change, and can be viewed physically as follows. The area of the Fermi surface is not very different slightly before or slightly after it undergoes the topology change. At the critical point, the area that fits just one electron orbit is brought inside the Fermi surface upon insertion of a flux quantum. When there is a single surface, one can indeed fit a physical electron within that orbit. However, when the Fermi surface contains the three pockets, the additional area brought inside each pocket due to a single flux quantum insertion is only $1/3$ of what is needed to fit one electron. If there were quasiparticles with charge $1/3$, then they could fill separately the area in the three pockets; but there are no such particles in the system. Hence, the flux periodicity is tripled when the Fermi surfaces are disconnected, as one can only add a full electron at each pocket, requiring the addition of three flux quanta. This is the physical origin of the period tripling.

1.3.1 Cyclotron frequency

Since we deal with strongly non-parabolic dispersion, it is useful to calculate cyclotron frequency. Within quasiclassical approximation, electron orbits along the contours of constant energy $\xi(\boldsymbol{p}) = \text{const}$. The evolution of momentum in magnetic field is driven by the Lorentz force

$$\dot{\boldsymbol{p}} = -e\boldsymbol{v} \times \boldsymbol{B}. \tag{1.12}$$

In terms of components of momentum that are perpendicular and parallel to the surface of constant energy $p_\perp, p_\parallel$ we have

$$\dot{p}_\parallel = ev_\perp B \implies \mathrm{d}p_\parallel = ev_\perp B \mathrm{d}t \tag{1.13}$$

and hence the corresponding frequency of the orbital motion

$$\omega_c(\mu) = 2\pi \left[\oint_{\mathrm{FS}} \mathrm{d}t \right]^{-1} = 2\pi eB \left[\oint_{\mathrm{FS}} \frac{\mathrm{d}p_\parallel}{v_\perp} \right]^{-1}. \tag{1.14}$$

The quantity in the square brackets above is nothing else but the density of states:

$$\oint_{\mathrm{FS}} \frac{\mathrm{d}p_{\parallel}}{v_{\perp}} = \oint_{\mathrm{FS}} \frac{\mathrm{d}p_{\parallel}}{\partial\xi/\partial p_{\perp}} = \oint_{\mathrm{FS}} \frac{\mathrm{d}\boldsymbol{p}}{\mathrm{d}\xi} = (2\pi)^2 \nu(\mu), \tag{1.15}$$

since $\partial\xi/\partial p_{\parallel} \equiv 0$ by virtue of parallel component being tangent to the Fermi surface. The statement is valid only for $\mu > 0$ where the Fermi surface is composed of a single sheet. For $\mu < 0$ only a third of the integral is relevant for an electron along one of the three petals of the Fermi surface and thus

$$\omega_c(\mu) = \frac{eB}{2\pi\nu(\mu)} \times \begin{cases} 1 & \mu > 0 \\ & \\ 3 & \mu < 0 \end{cases}. \tag{1.16}$$

in full compliance with speculations in the previous subsection.

1.3.2 Effects of disorder

Magnetic oscillations can only be observed if the following conditions are satisfied:

- Low temperature

$$T < \omega_c \tag{1.17}$$

- Low scattering

$$\omega_c \tau > 1 \tag{1.18}$$

- Low magnetic field

$$\omega_c < \varepsilon_* \tag{1.19}$$

The most restricting is the low scattering condition, since in the absence of impurities $\tau = \infty$ satisfying the other two conditions is not an issue. This restriction is especially problematic in the case of the monkey saddle, since scattering rate is inversely proportional to the density of states [28]

$$\tau(\mu) \propto \nu(\mu)^{-1} \propto |\mu - \mu_c|^{1/3}. \tag{1.20}$$

Let us consider the worst possible situation to observe magnetic oscillations:

$$\omega_c \sim \varepsilon_*, \quad \omega_c \tau \sim 1 \implies \tau \sim \varepsilon_*^{-1}. \tag{1.21}$$

Given that the energy scale of the singularity is $\varepsilon_* \sim u_3^3 \gamma_1 = 0.4$ meV, this corresponds to times $\tau > 0.1$ ps. In order to compare with available experimental data for unbiased BLG away from the charge neutrality, we have to account for the density of states difference:

$$\nu(\varepsilon_*) \sim u_3^{-3} \nu_0, \tag{1.22}$$

as it follows from Eq. 1.3. Here ν_0 is the density of states of unbiased BLG, implying that $\tau_0 \sim u_3^{-3} \tau \sim 100$ ps. Achieving such scattering times may be challenging even in high-mobility BLG sheets [29], but magnetic oscillations can still observed in the regime $\omega_c \tau > 1$, albeit with a much fainter magnitude.

1.4 Imaginary time path integral

In subsequent sections we will be analyzing RG flow of a monkey saddle at finite temperature. In order to handle this task, we need to introduce imaginary time path integral.

The essence of the imaginary time path integral approach to the description of quantum systems at finite temperature lies in an analogy between the time evolution operator over time t

$$U(t) = \exp(iHt), \tag{1.23}$$

and the density matrix of the canonical ensemble at the temperature T

$$\rho(\beta) = \exp(-\beta H), \quad \beta = 1/T. \tag{1.24}$$

It can be readily inferred that the latter looks like a former taken at imaginary time $t = i\beta$:

$$\rho(\beta) = U(i\beta). \tag{1.25}$$

This simple but powerful connection allows to extend zero temperature field theory methods

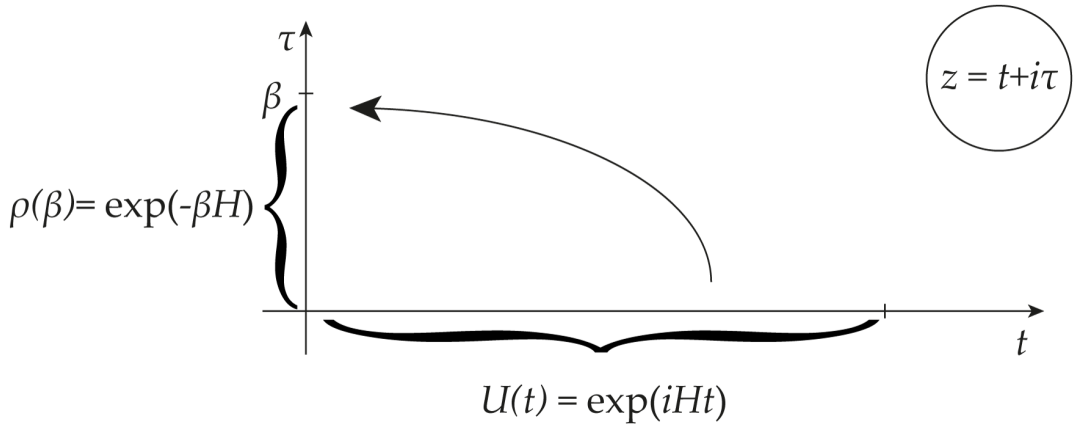

Figure 1.4: *Core idea behind imaginary time approach is the correspondence between the time evolution operator U and the density matrix ρ in the complex plane $t + i\tau$.*

to conquer the realm of finite temperatures. A pedagogical introduction can be found in Refs. [28, 30] and here we outline the prescription on how to deal with the formalism to extract quantities of interest for the present chapter.

1.4.1 Action

If we have a quantum system with Hamiltonian

$$\int \mathrm{d}\boldsymbol{r}\bar{\psi}[\widehat{H}(t,\boldsymbol{r})]\psi, \tag{1.26}$$

then the real time action can be constructed as

$$\mathcal{S}_0[\bar{\psi},\psi] = \int \mathrm{d}t \int \mathrm{d}\boldsymbol{r}\bar{\psi}[i\partial_t - \widehat{H}(t,\boldsymbol{r})]\psi \quad \text{(real time)}, \tag{1.27}$$

where $t, \boldsymbol{r}$ are time and coordinate and $\bar{\psi}, \psi$ are Grassmann anticommuting electron fields. Performing analytical continuation to imaginary times $t \to i\tau$, $\tau \in (0, \beta)$ we get imaginary time action

$$\mathcal{S}_0[\bar{\psi},\psi] = \int_0^\beta \mathrm{d}\tau \int \mathrm{d}\boldsymbol{r}\bar{\psi}[\partial_\tau - \widehat{H}(i\tau,\boldsymbol{r})]\psi \quad \text{(imaginary time)}, \tag{1.28}$$

and the missing "i" from the integration over time is absorbed into the definition of partition function (see below).

Electron Green's function can be interpreted as a propagator of Grassmann fields $\psi, \bar{\psi}$:

$$\begin{aligned} G_0(\tau_1 - \tau_2, \boldsymbol{r}_1 - \boldsymbol{r}_2) &= -\left\langle \psi(\tau_1, \boldsymbol{r}_1)\bar{\psi}(\tau_2, \boldsymbol{r}_2)\right\rangle_0 \\ &\equiv \int (\mathcal{D}\bar{\psi}\mathcal{D}\psi)(\psi_{\tau_1,\boldsymbol{r}_2}\bar{\psi}_{\tau_2,\boldsymbol{r}_2}) \exp\left(-\mathcal{S}_0[\bar{\psi}, \psi]\right) \\ &= \left[\partial_\tau - \widehat{H}(i\tau, \boldsymbol{r})\right]^{-1}\Big|_{\tau=\tau_1-\tau_2}, \end{aligned} \tag{1.29}$$

where "0" in $\langle \ldots \rangle_0$ means integrating out electron fields using free action weight $\exp(-\mathcal{S}_0)$. We assume time and space translation invariance, i.e. equilibrium and spatial homogeneity. The latter is not obvious *per se*, even in absence of disorder in the system spatial homogeneity may be spontaneously broken with a system undergoing a transition into phases such as charge-/spin-density wave or Fulde-Ferrel-Larkin-Ovchinnikov superconductivity. However, all such effects arise only as a consequence of electron-electron interactions.

Integration measure $\mathcal{D}\bar{\psi}\mathcal{D}\psi$ implies simply integrating out all electron fields. If we discretize space and time, it becomes

$$\mathcal{D}\bar{\psi}\mathcal{D}\psi = \prod_{\tau,\boldsymbol{r}} \mathrm{d}\bar{\psi}_{\tau,\boldsymbol{r}}\mathrm{d}\psi_{\tau,\boldsymbol{r}}. \tag{1.30}$$

In contrast with real-time approach, now the theory lives at a finite interval in imaginary time $(0, \beta)$ and hence we cannot work with continuous energy variables. Rather, we have to introduce half-integer Matsubara *frequencies*

$$\varepsilon_l = 2\pi T(l + 1/2), \quad l \in \mathrm{Z}, \tag{1.31}$$

such that the Green's function can be written in terms of it's Fourier components

$$G(\tau, \boldsymbol{r}) = T \sum_{l=-\infty}^{+\infty} G(i\varepsilon_l, \boldsymbol{r}), \tag{1.32}$$

$$G(i\varepsilon_l, \boldsymbol{r}) = \int_0^\beta \mathrm{d}\tau G(\tau, \boldsymbol{r}) \exp\left(i\varepsilon_l \tau\right). \tag{1.33}$$

(Both τ and ε_l are imaginary versions of time and energy, hence the Fourier exponent is still complex.) The 1/2 term in the definition of the Matsubara frequency ε_l has to do with the fermionic nature of the fields $\bar{\psi}, \psi$ [28]. If we look at a bosonic quantity, the right Matsubara

frequencies are integer,

$$\omega_n = 2\pi n, \quad n \in \mathrm{Z}. \tag{1.34}$$

1.4.2 Polarization operator

Polarization operator, an important quantity for this chapter, is an example of a bosonic case. Let us consider a simple single band electron system with dispersion $\xi(\boldsymbol{p})$:

$$\mathcal{S}_0[\bar{\psi}, \psi] = T \sum\!\!\!\!\!\!\int_l \mathrm{d}\boldsymbol{r} \bar{\psi}[i\varepsilon_l - \xi(-i\nabla_{\boldsymbol{r}}) + \mu]\psi, \tag{1.35}$$

where $\boldsymbol{p} \sim -i\nabla_{\boldsymbol{r}} \equiv -i\partial/\partial\boldsymbol{r}$ is electron momentum. Free electron propagator in terms of Matsubara frequency ε_l and momentum $\boldsymbol{p}$ is

$$G(i\varepsilon_l, \boldsymbol{p}) = \frac{1}{i\varepsilon_l - \xi(\boldsymbol{p}) + \mu}. \tag{1.36}$$

Let us now add an external scalar potential $V(t, \boldsymbol{r})$

$$\mathcal{S}_0[\bar{\psi}, \psi, V] = T \sum\!\!\!\!\!\!\int_l \mathrm{d}\boldsymbol{p} \bar{\psi}[i\varepsilon_l - \xi(\boldsymbol{p}) + \mu - V]\psi, \tag{1.37}$$

and introduce partition function

$$\mathcal{Z}[V] = \int (\mathcal{D}\bar{\psi}\mathcal{D}\psi) \exp(-\mathcal{S}_0[\bar{\psi}, \psi, V]). \tag{1.38}$$

Polarization operator describes density susceptibility to external scalar potential V and also determines its self-energy if we treat it as a scalar bosonic field. It is given by

$$\begin{aligned} \Pi(\tau_1 - \tau_2, \boldsymbol{r}_1 - \boldsymbol{r}_2) &= \left. \frac{\delta^2 \ln \mathcal{Z}[V]}{\delta V(\tau_1, \boldsymbol{r}_1) \delta V(\tau_2, \boldsymbol{r}_2)} \right|_{V=0} \\ &= \langle \bar{\psi}(\tau_1, \boldsymbol{r}_1)\psi(\tau_1, \boldsymbol{r}_1)\bar{\psi}(\tau_2, \boldsymbol{r}_2)\psi(\tau_2, \boldsymbol{r}_2)\rangle_0 \\ &= -G(\tau_1 - \tau_2, \boldsymbol{r}_1 - \boldsymbol{r}_2)G(\tau_2 - \tau_1, \boldsymbol{r}_2 - \boldsymbol{r}_1). \end{aligned} \tag{1.39}$$

Transforming to Matsubara frequency and momentum domains, we obtain

$$\begin{aligned} \Pi(i\omega_n, \boldsymbol{q}) &= -T \sum_{l=-\infty}^{+\infty} \int \mathrm{d}\boldsymbol{p} G(i\varepsilon_l, \boldsymbol{p}) G(i\varepsilon_{l+n}, \boldsymbol{p} + \boldsymbol{q}) \\ &= -T \sum_{l=-\infty}^{+\infty} \int \mathrm{d}\boldsymbol{p} \frac{1}{(i\varepsilon_l - \xi_{\boldsymbol{p}})(i\varepsilon_{l+n} - \xi_{\boldsymbol{p}+\boldsymbol{q}})}. \end{aligned} \tag{1.40}$$

In the static limit of almost uniform scalar potential (first we take the limit $\omega_m \to 0$, then $\boldsymbol{q} \to 0$) we should reproduce static compressibility of the system. This is indeed the case.

$$\begin{aligned}\Pi(0,\boldsymbol{q}) &= -T\sum_{l=-\infty}^{+\infty}\int \mathrm{d}\boldsymbol{p}\frac{1}{(i\varepsilon_l-\xi_{\boldsymbol{p}})(i\varepsilon_l-\xi_{\boldsymbol{p}+\boldsymbol{q}})}\\ &= -\int \mathrm{d}\boldsymbol{p}\frac{T}{\xi_{\boldsymbol{p}+\boldsymbol{q}}-\xi_{\boldsymbol{p}}}\sum_{l=-\infty}^{+\infty}\left[\frac{1}{i\varepsilon_l-\xi_{\boldsymbol{p}+\boldsymbol{q}}}-\frac{1}{i\varepsilon_l-\xi_{\boldsymbol{p}}}\right] = \frac{1}{2}\int \mathrm{d}\boldsymbol{p}\frac{f(\xi_{\boldsymbol{p}+\boldsymbol{q}})-f(\xi_{\boldsymbol{p}})}{\xi_{\boldsymbol{p}+\boldsymbol{q}}-\xi_{\boldsymbol{p}}}.\end{aligned} \tag{1.41}$$

To proceed we note that [28]

$$T\sum_{l=-\infty}^{+\infty}\frac{1}{i\varepsilon_l-\xi_{\boldsymbol{p}}} \equiv T\sum_{l=-\infty}^{+\infty}\frac{1}{2i\pi T(l+1/2)-\xi_{\boldsymbol{p}}} = -\frac{1}{2}f(\xi_{\boldsymbol{p}}), \tag{1.42}$$

where

$$f(x) = \tanh\frac{x}{2T} \tag{1.43}$$

is nothing else but the equilibrium distribution function. Taking the uniform limit $\boldsymbol{q} \to 0$,

$$\lim_{\boldsymbol{q}\to\boldsymbol{0}}\Pi(0,\boldsymbol{q}) = \frac{1}{2}\int \mathrm{d}\boldsymbol{p}\frac{\partial f(\xi_{\boldsymbol{p}})}{\partial\xi_{\boldsymbol{p}}} = \frac{1}{2}\int\left(\frac{\mathrm{d}\boldsymbol{p}}{\mathrm{d}\xi}\right)\mathrm{d}\xi\frac{\partial f(\xi)}{\partial\xi} \equiv \frac{1}{2}\int(\nu(\xi)\mathrm{d}\xi)\frac{\partial f(\xi)}{\partial\xi}, \tag{1.44}$$

where we switched to integration over the energy variable ξ and introduced the density of states $\nu(\xi)$. For the case of slowly varying density of states we have $\lim_{\boldsymbol{q}\to\boldsymbol{0}}\Pi(0,\boldsymbol{q}) \simeq \nu(0)$. (This is *not* applicable to the monkey saddle, where the density of states has a strong energy dependence.)

The polarization operator serves as an important building block for the RG flow in the following sections. Due to a more sophisticated dispersion in BLG that has several electron flavors (different spins $\uparrow\downarrow$ and valleys K/K'), we will have more than one type of polarization operator. Now we are ready to set up RG.

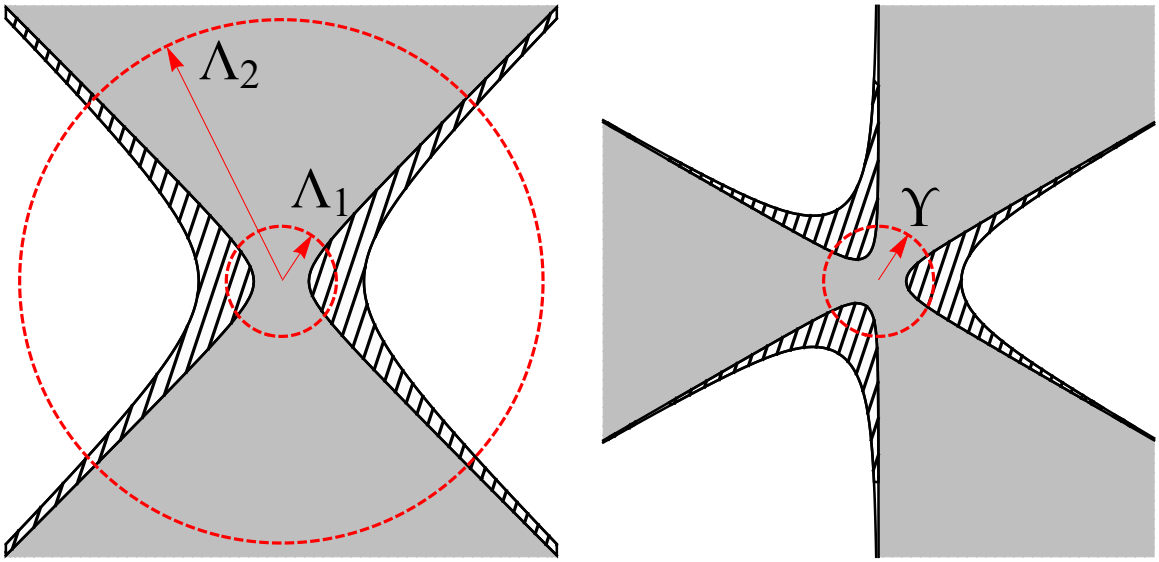

Figure 1.5: ***Left****: A Fermi surface near a van Hove saddle calls for a two-cutoff RG scheme. The grey area represents occupied electron states. The hatched region of the phase space corresponds to a step $d\xi$ in electron energy. Normally, one cutoff $d\Lambda_1 \sim d\xi$ is sufficient, but here we see that the logarithmic DoS at the van Hove saddle together with an open hyperbolic Fermi surface lead to tails of the hatched region that reach out to the rest of the Fermi surface away from the van Hove saddle. The purpose of the second cutoff Λ_2 is to cut these tails and isolate van Hove saddle.* ***Right****: No second cutoff is needed at the monkey saddle.*

1.5 RG flow at the single monkey saddle

Here we analyze a single monkey saddle within a one-loop RG framework. Assuming short-range interaction, an electron action is given by

$$\mathcal{S} = \int (\mathrm{d}\tau \mathrm{d}\boldsymbol{r}) \left[\psi^\dagger [\partial_\tau - \xi(-i\nabla) + \mu]\psi - \frac{g}{2}(\psi^\dagger\psi)^2 \right] \tag{1.45}$$

with interaction

$$\frac{g}{2}(\psi^\dagger\psi)^2 = g(\psi_\uparrow^\dagger \psi_\downarrow^\dagger \psi_\downarrow \psi_\uparrow). \tag{1.46}$$

We focus on the system tuned exactly to the monkey saddle, so that the dispersion is determined by the catastrophe germ $\xi(\boldsymbol{p}) = p^3 \cos 3\phi$ and the non-singular part of FS is irrelevant (see Fig. 1.5). Tree-level RG involves rescaling of frequency and momenta as

$$\omega \to s^{-1}\omega,\ \boldsymbol{p} \to s^{-1/3}\boldsymbol{p},\ \psi \to s^{-1/3}\psi, \tag{1.47}$$

and results in the interaction constant scaling as

$$g \to g s^{+1/3}, \tag{1.48}$$

entailing super-renormalizability of the theory.

Super-renormalizability brings crucial simplifications with respect to the case of the ordinary vH saddle: while the separation of the saddle from the non-singular part of the FS requires two cut-offs in the case of vH singularities ($n = 2$), it requires only one cut-off for higher order singularities ($n > 2$), see Fig. 1.5. This difference can be traced back to the behavior of DoS obtained in Eq.(1.6). In the case of the vH saddle ($n = 2$), the integral over the angle-like variable η diverges logarithmically, requiring an additional cut-off in the problem that is interpreted as a Fermi velocity cut-off in Refs. [20, 18]. In contrast, for any higher-order saddle with $n > 2$, the DoS at a given energy is well-defined and is determined solely by the saddle and does not require a large momentum cut-off. This means that for $n > 2$ the theory is free of UV divergences and contains only (meaningful) IR divergences that are regularized by temperature T and chemical potential μ.

We introduce a dimensionless coupling constant in a natural way as

$$\lambda(\mathrm{Y}) = \nu(\mathrm{Y}) g(\mathrm{Y}), \tag{1.49}$$

with a smooth *infrared* cutoff Y that we take to be either μ or T.

1.5.1 Beta function

The RG flow equation for the dimensionless interaction λ constant is connected to renormalization of the dimensional coupling constant g as

$$\frac{\mathrm{d}\lambda}{\mathrm{d}\ln\nu} = \frac{\mathrm{d}(\nu g)}{\mathrm{d}\ln\nu} = \lambda + \nu^2 \frac{\mathrm{d}g}{\mathrm{d}\nu}. \tag{1.50}$$

The one-loop renormalization of g is given by two diagrams shown in Fig. 1.6 and yield

$$\delta g = -g^2 \Pi_{pp}(\mu, T) + g^2 \Pi_{ph}(\mu, T). \tag{1.51}$$

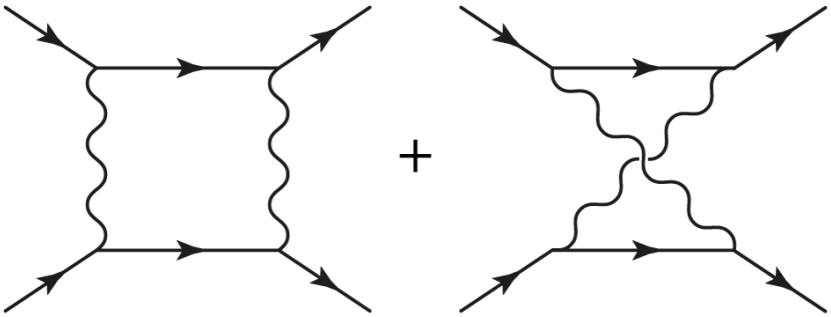

Figure 1.6: *One-loop contribution to renormalization of the interaction constant for an isolated monkey saddle.*

Combining Eqs. (1.50) and (1.51) we obtain the RG equation for λ,

$$\frac{\mathrm{d}\lambda}{\mathrm{d}\ln\nu(\mathrm{Y})} = \lambda - c\lambda^2, \tag{1.52}$$

where c is a non-negative coefficient

$$c = \frac{\mathrm{d}\Pi_{pp}}{\mathrm{d}\nu(\mathrm{Y})} - \frac{\mathrm{d}\Pi_{ph}}{\mathrm{d}\nu(\mathrm{Y})} \geq 0. \tag{1.53}$$

The polarization operators are defined as

$$\Pi_{ph}(\boldsymbol{q},\mu,T) = -T\sum\!\!\!\!\!\!\int_{l,\boldsymbol{p}} G(i\varepsilon_l,\boldsymbol{p}+\boldsymbol{q})G(i\varepsilon_l,\boldsymbol{p}), \tag{1.54}$$

$$\Pi_{pp}(\boldsymbol{q},\mu,T) = T\sum\!\!\!\!\!\!\int_{l,\boldsymbol{p}} G(i\varepsilon_l,\boldsymbol{p}+\boldsymbol{q})G(-i\varepsilon_l,-\boldsymbol{p}), \tag{1.55}$$

and the particle-hole polarization operator can be evaluated to be

$$\Pi_{ph} = -T\int_{\boldsymbol{p}}\sum_l \frac{1}{i\varepsilon_l - \xi_{\boldsymbol{p}+\boldsymbol{q}}+\mu}\frac{1}{i\varepsilon_l - \xi_{\boldsymbol{p}}+\mu} \tag{1.56}$$

$$= \frac{1}{2}\int_{\boldsymbol{p}} \frac{f(\xi_{\boldsymbol{p}+\boldsymbol{q}}-\mu) - f(\xi_{\boldsymbol{p}}-\mu)}{\xi_{\boldsymbol{p}+\boldsymbol{q}}-\xi_{\boldsymbol{p}}} \tag{1.57}$$

$$\underset{\boldsymbol{q}\to 0}{=} \frac{1}{2}\int \nu(\xi)\, f'(\xi-\mu)\,\mathrm{d}\xi\,, \tag{1.58}$$

where $f(\xi) = \tanh\xi/2T$.

Similarly, the particle-particle polarization operator is

$$\Pi_{pp} = \frac{1}{2}\int_{\boldsymbol{p}} \frac{f(\xi_{\boldsymbol{p}}-\mu)+f(\xi_{-\boldsymbol{p}}-\mu)}{\xi_{\boldsymbol{p}}+\xi_{-\boldsymbol{p}}-2\mu} \tag{1.59}$$

$$= \frac{1}{2}\int \nu(\xi)\,\frac{f(\xi+\mu)-f(\xi-\mu)}{2\mu}\,\mathrm{d}\xi\,. \tag{1.60}$$

The difference of polarization operators that drives RG flow has the following asymptotic behavior:

$$\Pi_{pp}-\Pi_{ph} = \begin{cases} 0 & \mu = 0,\ T \neq 0 \\ \dfrac{1}{2}\nu(\mu) & T = 0,\ \mu \neq 0 \end{cases}, \tag{1.61}$$

where the cancellation at $\mu = 0$ in fact holds for any external frequency and momentum.

The chemical potential also has a correction due to a Hartree-type diagram,

$$\delta\mu = g \fint_{l,\boldsymbol{p}} G(i\varepsilon_l, \boldsymbol{p}), \tag{1.62}$$

corresponding to the shift in the monkey saddle's Fermi energy. (This contribution is the equivalent of the fluctuational renormalization of the critical temperature in thermodynamic phase transitions.)

Finally, we point out that the cancellation of the one-loop contribution at $\mu = 0$ is a feature specific to odd saddles. For an n-th order saddle with a dispersion $\xi = p^n \cos n\phi$ the DoS behaves as $\nu(\varepsilon) \propto \varepsilon^{-(n-2)/n}$, while the polarization operators behave as

$$\Pi_{pp}-\Pi_{ph} = \begin{cases} \frac{1+(-1)^n}{n} C_n \nu(\mu) & \mu = 0,\ T \neq 0 \\ \frac{n-2}{2}\nu(\mu) & T = 0,\ \mu \neq 0 \end{cases}, \tag{1.63}$$

with a (positive) numerical constant

$$C_n = \int_0^\infty \mathrm{d}x\, x^{-(n-2)/n} (2\cosh^2(x/2))^{-1} = 2(2^{2/n}-1)\Gamma\left(2-\frac{2}{n}\right)\left[-\zeta\left(1-\frac{2}{n}\right)\right]. \tag{1.64}$$

As we mentioned previously in the text, this difference leads to non-Fermi-liquid and marginal Fermi liquid behavior for odd and even saddles, respectively.

1.5.2 Analysis of the RG flow

Now let's analyze the obtained beta function (1.52). The scaling behavior of the system strongly resembles that of 1D interacting electrons. Namely, exactly at the monkey saddle at $\mu = 0$ the one-loop contribution to beta function vanishes, leaving a critical theory with tree-level scaling only

$$\frac{\mathrm{d}\lambda}{\mathrm{d}\ln\nu(T)} = \lambda \quad (\mu = 0, \forall T). \tag{1.65}$$

This behavior is linked to an additional symmetry [18] that arises exactly at the monkey saddle, and is a combination of time-reversal transformation $(\varepsilon, \boldsymbol{p}) \to (-\varepsilon, -\boldsymbol{p})$ plus a particle-hole transformation $\psi^\dagger \rightleftharpoons \psi$. This symmetry is present only for odd saddles with $\xi(-\boldsymbol{p}) = -\xi(\boldsymbol{p})$ and is absent for even saddles that have a dispersion that is invariant under spatial inversion.

At the same time, away from the monkey saddle

$$\frac{\mathrm{d}\lambda}{\mathrm{d}\ln\nu(\mu)} = \lambda - \frac{1}{2}\lambda^2 \quad (T \ll |\mu| \neq 0), \tag{1.66}$$

and the system either flows to a non-trivial fixed point $\lambda = 2$ for any positive initial coupling constant $\lambda_0 > 0$ or develops a superconducting instability with λ diverging as (for $\lambda_0 < 0$)

$$\lambda(\mu) = \frac{\nu(\mu) g_0}{1 + 2g_0[\nu(\mu) - \nu_0]} \simeq \frac{3\mu_c}{2(\mu_c - \mu)}. \tag{1.67}$$

Here ν_0 and g_0 are the DoS and coupling constant at the initial energy scale, while μ_c marks the energy scale corresponding to the instability. This leads to a non-BCS type of behavior for the critical energy scale

$$\mu_c, T_c \propto g_0^{\frac{n}{n-2}} \underset{(n=3)}{=} g_0^3. \tag{1.68}$$

In fact, the one-loop RG equations can be integrated out for any μ, T and the solution is equivalent to resummation of a leading diagrammatic series in the language of Feynman diagrams. The resulting expression for a dimensional coupling constant g reads as

$$g^{-1}|_{(\mu,T)} = \left(\Pi_{pp} - \Pi_{ph}\right)|_{(\mu,T)} + g_0^{-1}, \tag{1.69}$$

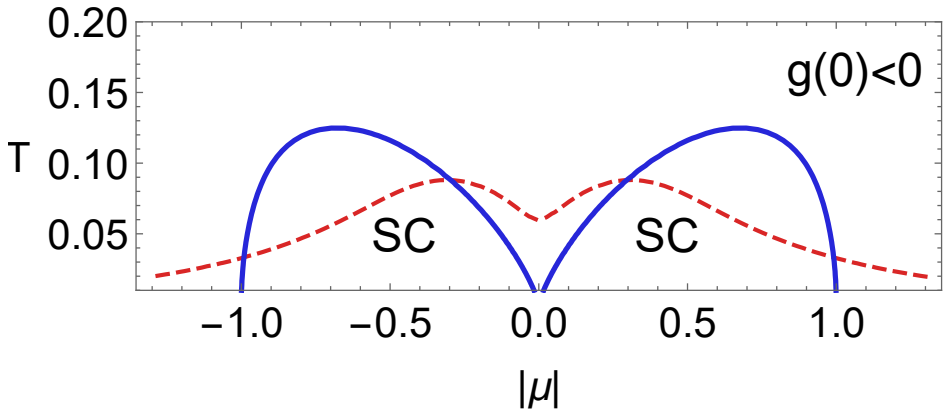

Figure 1.7: *Phase diagram (blue solid line) for an isolated monkey saddle and attractive coupling constant. Critical chemical potential is determined by the equation* $|g_0|\nu(\mu_c) = 2$ *and the plot is given in units of* μ_c *for both temperature and chemical potential. Any odd saddle* ($n = 3, 5, \ldots$) *has qualitatively same phase diagram, but the situation is different for even saddles* ($n = 2, 4, \ldots$). *Even case is illustrated with red dashed line for* $n = 4$.

Thus, within a one-loop approximation, the phase transition line for attractive interaction $g < 0$ is determined by the equation

$$g_0 \left(\Pi_{pp} - \Pi_{ph}\right)|_{(\mu,T)} + 1 = 0 \tag{1.70}$$

and the resulting phase diagram is given in Fig.1.7.

1.5.3 Quasiparticle decay rate

In this subsection we analyze the scaling of the quasiparticle decay rate. It is connected to the imaginary part of electron self-energy

$$\Gamma = \frac{i}{2}\Delta\Sigma(0, \mathbf{0})\Big|_{\mu=0}. \tag{1.71}$$

Despite the equilibrium nature of the problem, it is convenient to break causality and use the real-time Keldysh technique that we introduce later in chapter (3). There are no one-loop contributions to the imaginary part of the electron self-energy:

$$\Gamma = 0 \quad \text{(one loop)}. \tag{1.72}$$

The simplest diagram that gives a nontrivial contribution to the quasiparticle width is

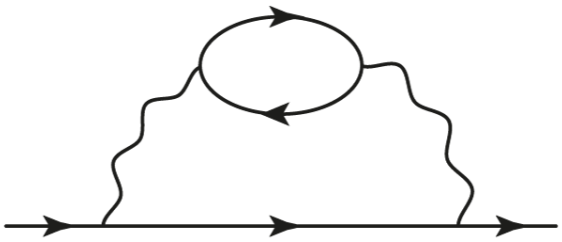

Figure 1.8: *Two-loop contribution to the quasiparticle decay rate.*

shown on Fig. (1.8). Using Keldysh technique it can be written as

$$\begin{aligned}\Delta\Sigma(\varepsilon,\boldsymbol{p}) &= -\int_{\omega,\boldsymbol{q}}\left[B(\omega)+f(\varepsilon-\omega)\right]\Delta G(\varepsilon-\omega,\boldsymbol{p}-\boldsymbol{q})\Delta L(\omega,\boldsymbol{q})\\ &= -i\int_{\boldsymbol{q}}\left[B(\varepsilon-\xi_{p-q})+f(\xi_{p-q})\right]\Delta L(\varepsilon-\xi_{p-q},\boldsymbol{q}),\end{aligned} \tag{1.73}$$

where $B(x) = \coth(x/2T)$ and $f(x) = \tanh(x/2T)$ are bosonic and fermionic distribution functions, L is an interaction propagator, and $\Delta(\dots) = (\dots)^R - (\dots)^A$ stands for the difference between retarded and advanced components. The interaction propagator within the one-loop approximation is essentially

$$\begin{aligned}\Delta\Sigma(\varepsilon,\boldsymbol{p}) = -ig^2\int_{k,q}&\delta(\varepsilon+\xi_{k+q-p}-\xi_q-\xi_k)\times\\ &\times\Big(f(\xi_q)[f(\xi_k)-f(\xi_k+\xi_q-\varepsilon)]+1-f(\xi_k)f(\xi_k+\xi_q-\varepsilon)\Big),\end{aligned} \tag{1.74}$$

where we made use of the relation between equilibrium distribution functions

$$[f(x+y)-f(x)]B(y) = 1-f(x+y)f(x), \tag{1.75}$$

and redefined integration variables $\boldsymbol{k},\boldsymbol{q}$. In principle, diagrammatic technique isn't needed for this result, since it is essentially a statement of Fermi's golden rule.

Rescaling momenta as $(\boldsymbol{k},\boldsymbol{q}) \to T^{1/3}(\boldsymbol{k},\boldsymbol{q})$ we see that the quasiparticle width at the monkey saddle for zero chemical potential and zero external frequency and momenta behaves as

$$\Gamma = \frac{i}{2}\Delta\Sigma(0,\boldsymbol{0})\Big|_{\mu=0} \sim \underbrace{[\nu(T)g]}_{\lambda(T)}{}^2 T \propto T^{1/3}, \tag{1.76}$$

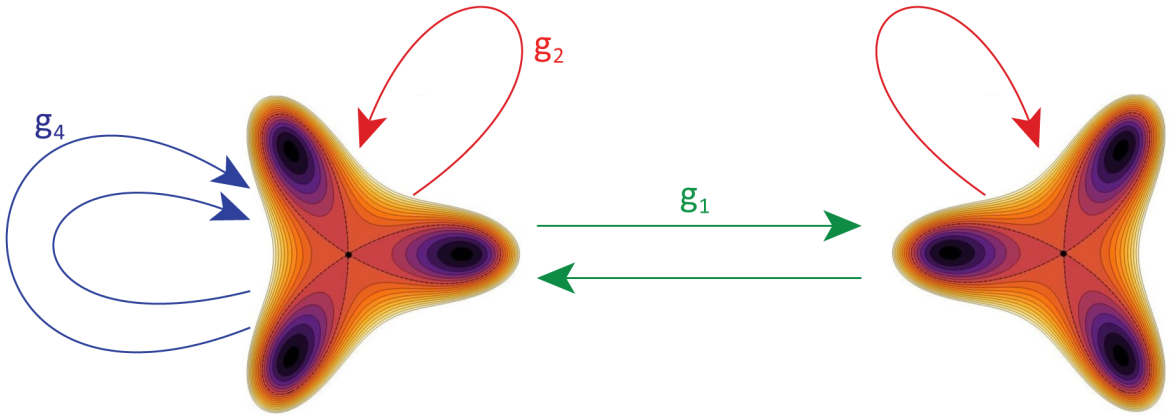

Figure 1.9: *Three possible interaction channels between the two monkey saddles in bilayer graphene, as introduced in Eq. (1.78).*

since exactly at the monkey saddle $\mu = 0$ one-loop contribution to the beta function vanishes and interaction constant $\lambda(T) = g\,\nu(T) \propto T^{-1/3}$ has only tree level scaling. Our analysis breaks down at energy scales $T^* \sim \Gamma(T^*)$, or equivalently when dimensionless coupling constant $\lambda(T^*) \gtrsim 1$ becomes too large.

On the other hand, for non-zero chemical potential we find regular Fermi-liquid-like behavior [31],

$$\Gamma \sim \lambda^2(\mu)\frac{\varepsilon^2}{\mu}\ln\frac{\mu}{\varepsilon}, \quad T \ll \varepsilon \ll |\mu|\,. \tag{1.77}$$

The situation is the same for any odd saddle, $n = 3, 5, \ldots$, but is very different for even saddles. For even saddles there is no cancellation of the one-loop contribution, so that $c \neq 0$ at $\mu = 0$ and the dimensionless coupling constant flows to a fixed point $\lambda = 1/c$ yielding marginal Fermi liquid behavior with decay rate $\Gamma \sim T$. While this implies a dimensionless coupling constant of order one, the existence of this fixed point could be justified within $1/N$ expansion techniques.

1.6 RG flow for bilayer graphene

1.6.1 RG flow equations

In BLG there are two copies of the monkey saddle at the K and K' points, which are related by time-reversal symmetry, with dispersions $\xi_\pm(\boldsymbol{p}) = \pm\xi(\boldsymbol{p})$. The four-fermion interaction now has three coupling constants:

$$\frac{g}{2}(\psi^\dagger\psi)^2 = g_1(\psi^\dagger_{+i}\psi^\dagger_{-j}\psi_{+j}\psi_{-i}) + g_2(\psi^\dagger_{+i}\psi^\dagger_{-j}\psi_{-j}\psi_{+i}) + \cancel{g_3(\psi^\dagger_{+i}\psi^\dagger_{+j}\psi_{-j}\psi_{-i})} + g_4(\psi^\dagger_{\alpha\uparrow}\psi^\dagger_{\alpha\downarrow}\psi_{\alpha\downarrow}\psi_{\alpha\uparrow}), \tag{1.78}$$

where $i, j = \uparrow\downarrow$ indices stand for spin and $\alpha = \pm$ corresponds to K/K' valley isospin, respectively. Our notation for coupling constants is the same as in Refs. [10, 19]. The Umklapp g_3 coupling is forbidden because the K and K' points are inequivalent in the sense of momentum conservation modulo reciprocal lattice vector, $\boldsymbol{Q} = 2\boldsymbol{p}_{KK'} \neq \boldsymbol{0}$.

In addition to polarization operators (1.54) and (1.55), BLG has two new polarization operators at a finite momentum transfer $\boldsymbol{Q}$:

$$\Pi_{ph}(\boldsymbol{Q}, \mu, T) = -T \sum\!\!\!\!\!\!\int_{l,\boldsymbol{p}} G(i\varepsilon_l, \boldsymbol{p}) G(i\varepsilon_l, \boldsymbol{Q} + \boldsymbol{p}), \tag{1.79}$$

$$\Pi_{pp}(\boldsymbol{Q}, \mu, T) = T \sum\!\!\!\!\!\!\int_{l,\boldsymbol{p}} G(i\varepsilon_l, \boldsymbol{p}) G(-i\varepsilon_l, \boldsymbol{Q} - \boldsymbol{p}). \tag{1.80}$$

Once calculated, they yield

$$\Pi_{ph}(\boldsymbol{Q}) = \frac{1}{2}\int \nu(\xi)\,\frac{f(\xi-\mu) - f(-\xi-\mu)}{2\xi}\,\mathrm{d}\xi, \tag{1.81}$$

$$\Pi_{pp}(\boldsymbol{Q}) = \frac{1}{2}\int \nu(\xi)\,\frac{f(\xi+\mu)}{\xi+\mu}\,\mathrm{d}\xi. \tag{1.82}$$

In this chapter we focus on the case when the system is tuned exactly into the monkey saddle, $\mu = 0$, where

$$\Pi_{ph}(\boldsymbol{0}) = \Pi_{pp}(\boldsymbol{0}) = C_3\,\nu(T), \qquad (\mu = 0) \tag{1.83}$$

$$\Pi_{ph}(\boldsymbol{Q}) = \Pi_{pp}(\boldsymbol{Q}) = 3C_3\,\nu(T), \tag{1.84}$$

with numerical constant

$$C_3 = \int_0^\infty \mathrm{d}x\, x^{-1/3} \frac{1}{2\cosh^2(x/2)} = 1.14. \tag{1.85}$$

Polarization operators (1.83, 1.84) serve as building blocks of the RG flow. The RG flow equations for a square lattice with two hot spots were derived in Ref. [10]. These equations are very general and in their infinitesimal form, after an elementary RG step, they give

$$\begin{aligned}
\delta g_1 =& 2g_1(g_2 - g_1)\delta\Pi_{ph}(\boldsymbol{Q}) + 2g_1 g_4 \delta\Pi_{ph}(\mathbf{0}) - 2g_1 g_2 \delta\Pi_{pp}(\boldsymbol{Q}),\\
\delta g_2 =& (g_2^2 + g_3^2)\delta\Pi_{ph}(\boldsymbol{Q}) + 2(g_1 - g_2)g_4\delta\Pi_{ph}(\mathbf{0}) - (g_1^2 + g_2^2)\delta\Pi_{pp}(\boldsymbol{Q}),\\
\delta g_3 =& -2g_3 g_4 \delta\Pi_{pp}(\mathbf{0}) + 2(2g_2 - g_1)g_3\delta\Pi_{ph}(\boldsymbol{Q})\\
\delta g_4 =& -(g_3^2 + g_4^2)\delta\Pi_{pp}(\mathbf{0}) + (g_1^2 + 2g_1 g_2 - 2g_2^2 + g_4^2)\delta\Pi_{ph}(\mathbf{0}).
\end{aligned} \tag{1.86}$$

We re-derive these equations for our case of two monkey saddles in BLG by calculating the Feynman diagrams listed on the Fig. 1.10. As we have mentioned above, in the case of BLG there is no Umklapp scattering between K and K' points, and thus we have $g_3 \equiv 0$. The resulting corrections to interaction constants are

$$\begin{aligned}
\delta g_1 =& 2g_1(g_2 - g_1)\delta\Pi_{ph}(\boldsymbol{Q}) + 2g_1 g_4 \delta\Pi_{ph}(\mathbf{0}) - 2g_1 g_2 \delta\Pi_{pp}(\boldsymbol{Q}),\\
\delta g_2 =& g_2^2\delta\Pi_{ph}(\boldsymbol{Q}) + 2(g_1 - g_2)g_4\delta\Pi_{ph}(\mathbf{0}) - (g_1^2 + g_2^2)\delta\Pi_{pp}(\boldsymbol{Q}),\\
\delta g_4 =& -g_4^2\delta\Pi_{pp}(\mathbf{0}) + (g_1^2 + 2g_1 g_2 - 2g_2^2 + g_4^2)\delta\Pi_{ph}(\mathbf{0}).
\end{aligned} \tag{1.87}$$

The coupling constants g_i are dimensionful, but we introduce dimensionless coupling constants as follows. Since each polarization operator is proportional to the density of states $\Pi_{pp}(\mathbf{0}) \propto \nu$ (see Eqs. 1.83, 1.84), it is appropriate and convenient to define the dimensionless constants as $\lambda_i = \Pi_{pp}(\mathbf{0})g_i$, and take $\mathrm{d}\ln\Pi_{pp}(\mathbf{0})$ for RG time ds:

$$\begin{aligned}
\dot\lambda_1 =& \lambda_1 + 2d_1\lambda_1(\lambda_2 - \lambda_1) + 2d_2\lambda_1\lambda_4 - 2d_3\lambda_1\lambda_2,\\
\dot\lambda_2 =& \lambda_2 + d_1\lambda_2^2 + 2d_2(\lambda_1 - \lambda_2)\lambda_4 - d_3(\lambda_1^2 + \lambda_2^2),\\
\dot\lambda_4 =& \lambda_4 - d_0\lambda_4^2 + d_2(\lambda_1^2 + 2\lambda_1\lambda_2 - 2\lambda_2^2 + \lambda_4^2),
\end{aligned} \tag{1.88}$$

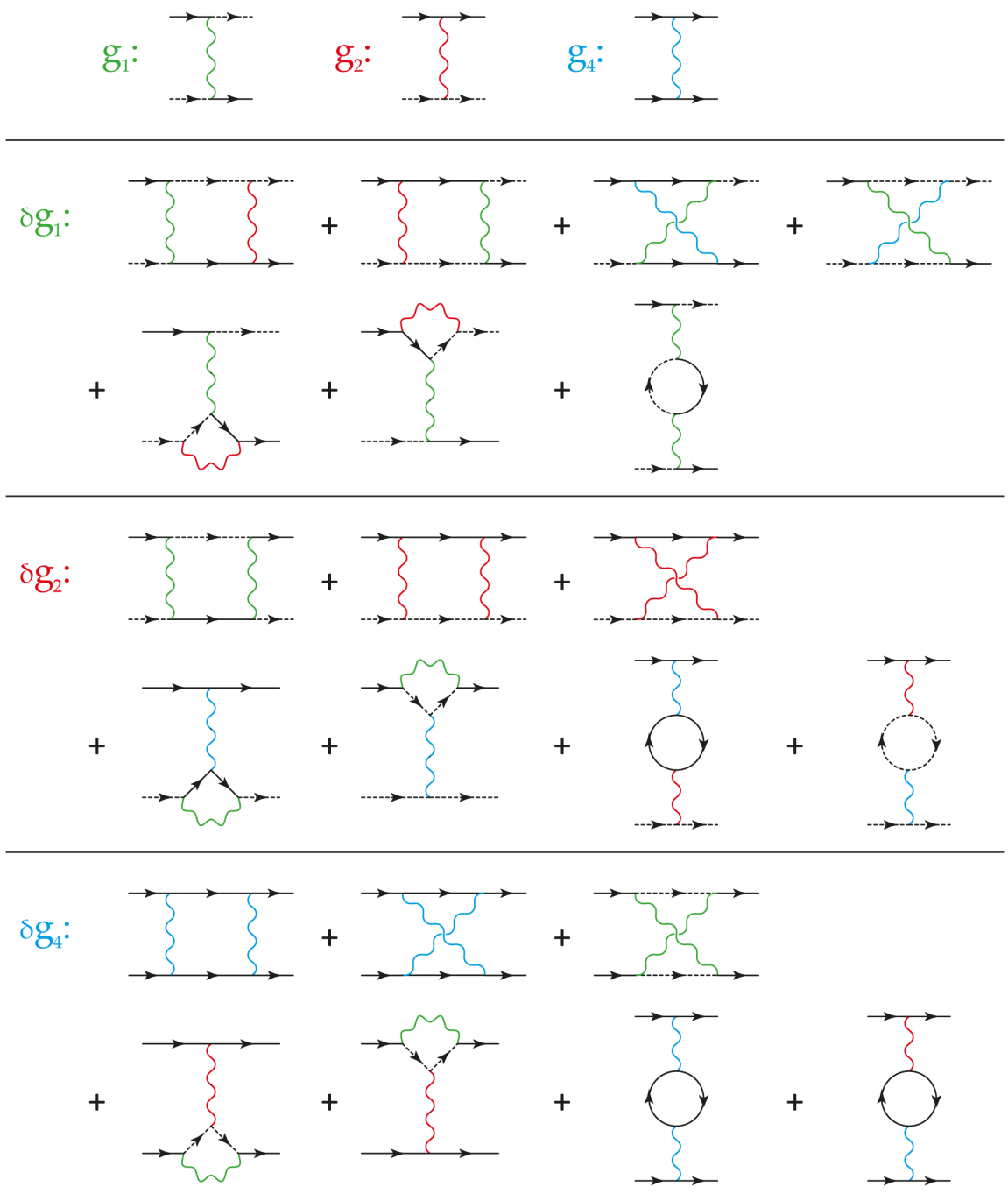

Figure 1.10: *One-loop Feynman diagrams contributing to the renormalization of the interaction constants introduced in Eq. (1.78). Black solid lines represent electron propagators around K valley and dashed lines show propagators around K′ valley.*

where parameters d_i are defined as

$$d_0 \equiv \frac{\mathrm{d}\Pi_{pp}(\boldsymbol{Q})}{\mathrm{d}\Pi_{pp}(\boldsymbol{Q})}, \qquad d_2 \equiv \frac{\mathrm{d}\Pi_{ph}(\boldsymbol{0})}{\mathrm{d}\Pi_{pp}(\boldsymbol{Q})}, \tag{1.89}$$

$$d_1 \equiv \frac{\mathrm{d}\Pi_{ph}(\boldsymbol{Q})}{\mathrm{d}\Pi_{pp}(\boldsymbol{Q})}, \qquad d_3 \equiv \frac{\mathrm{d}\Pi_{pp}(\boldsymbol{0})}{\mathrm{d}\Pi_{pp}(\boldsymbol{Q})}, \tag{1.90}$$

and $d_0 \equiv 1$ is introduced for the sake of generality and ease of comparison with Ref. [10]. We focus on BLG tuned exactly at the monkey saddle with both critical voltage bias $\delta = 1$ and chemical potential $\mu = 0$, where these parameters are equal to

$$d_0 \equiv 1, \quad d_1 = 3, \quad d_2 = 1, \quad d_3 = 3. \tag{1.91}$$

The RG flow equations for dimensionless coupling constants now become

$$\dot{\lambda}_1 = \lambda_1 - 6\lambda_1^2 + 2\lambda_1\lambda_4, \tag{1.92}$$

$$\dot{\lambda}_2 = \lambda_2 + 2(\lambda_1 - \lambda_2)\lambda_4 - 3\lambda_1^2, \tag{1.93}$$

$$\dot{\lambda}_4 = \lambda_4 + \lambda_1^2 + 2\lambda_1\lambda_2 - 2\lambda_2^2. \tag{1.94}$$

At the brink of a many-body instability the coupling constants diverge as

$$\lambda_i = \frac{\lambda_i^{(0)}}{s_c - s}, \tag{1.95}$$

where s_c is a critical RG time corresponding to the instability. Before proceeding to identifying diverging solutions, we need to find a way to interpret physical nature of diverging solutions. This can be achieved by calculating susceptibilities to different order parameters [10, 11, 32].

1.6.2 Susceptibilities

When coupling constants diverge as $\lambda_j \propto (s_c - s)^{-1}$, susceptibilities to different order parameters also diverge as $\chi_j \propto (s_c - s)^{\alpha_j}$, so the leading instability is the one with the most negative value of α_j.

Susceptibilities can be calculated by studying renormalization of test vertices [19]. The

first group of instabilities correspond to uniform densities with a test Lagrangian density

$$\delta\mathcal{L} = \sum_{i=\uparrow\downarrow} \sum_{\alpha=+-} n_{i\alpha} \psi^{\dagger}_{i\alpha} \psi_{i\alpha}, \tag{1.96}$$

where renormalization of test vertices $n_{i\alpha}$ within one-loop approximation is given by equation

$$\frac{\mathrm{d}}{\mathrm{d}s} \begin{pmatrix} n_{+\uparrow} \\ n_{+\downarrow} \\ n_{-\uparrow} \\ n_{-\downarrow} \end{pmatrix} = d_2 \begin{pmatrix} 0 & -\lambda_4 & \lambda_1 - \lambda_2 & -\lambda_2 \\ -\lambda_4 & 0 & -\lambda_2 & \lambda_1 - \lambda_2 \\ \lambda_1 - \lambda_2 & -\lambda_2 & 0 & -\lambda_4 \\ -\lambda_2 & \lambda_1 - \lambda_2 & -\lambda_4 & 0 \end{pmatrix} \begin{pmatrix} n_{+\uparrow} \\ n_{+\downarrow} \\ n_{-\uparrow} \\ n_{-\downarrow} \end{pmatrix} \tag{1.97}$$

and susceptibilities are equal to $\alpha = -2\gamma$, where γ is an eigenvalue of (1.97). Solving for eigensystem of (1.97) we find four instabilities with susceptibilities

$$\alpha_{\text{spin}} = -2(\lambda_1^0 + \lambda_4^0), \tag{1.98}$$

$$\alpha_{\text{charge}} = 2(-\lambda_1^0 + 2\lambda_2^0 + \lambda_4^0), \tag{1.99}$$

$$\alpha_{\text{valley}} = 2(\lambda_1^0 - 2\lambda_2^0 + \lambda_4^0), \tag{1.100}$$

$$\alpha_{\text{spin-valley}} = 2(\lambda_1^0 - \lambda_4^0). \tag{1.101}$$

The second group of instabilities is a charge- and spin-density waves,

$$\delta\mathcal{L} = \sum_{i=\uparrow\downarrow} n_{Qi} \psi^{\dagger}_{-i} \psi_{+i} + \text{h.c.} \tag{1.102}$$

$$\frac{\mathrm{d}}{\mathrm{d}s} \begin{pmatrix} n_{Q\uparrow} \\ n_{Q\downarrow} \end{pmatrix} = d_1 \begin{pmatrix} \lambda_2 - \lambda_1 & -\lambda_1 \\ -\lambda_1 & \lambda_2 - \lambda_1 \end{pmatrix} \begin{pmatrix} n_{Q\uparrow} \\ n_{Q\downarrow} \end{pmatrix}, \tag{1.103}$$

$$\alpha_{CDW} = 6(2\lambda_1^0 - \lambda_2^0), \tag{1.104}$$

$$\alpha_{SDW} = -6\lambda_2^0. \tag{1.105}$$

The third group represents superconducting s- and $s_{\pm}$-wave instabilities,

$$\delta\mathcal{L} = \Delta_1 \psi^{\dagger}_{+\uparrow}\psi^{\dagger}_{-\downarrow} + \Delta_2 \psi^{\dagger}_{-\uparrow}\psi^{\dagger}_{+\downarrow} + \text{h.c.}, \tag{1.106}$$

$$\frac{\mathrm{d}}{\mathrm{d}s}\begin{pmatrix}\Delta_1\\ \Delta_2\end{pmatrix} = d_3 \begin{pmatrix}-\lambda_2 & -\lambda_1\\ -\lambda_1 & -\lambda_2\end{pmatrix}\begin{pmatrix}\Delta_1\\ \Delta_2\end{pmatrix}, \tag{1.107}$$

$$\alpha_{sP} = 6(\lambda_2^0 + \lambda_1^0), \tag{1.108}$$

$$\alpha_{s_{\pm}P} = 6(\lambda_2^0 - \lambda_1^0). \tag{1.109}$$

Finally, the last group corresponds to finite momentum superconductivities,

$$\delta\mathcal{L} = \Delta_{sQ+} \psi^{\dagger}_{+\uparrow}\psi^{\dagger}_{+\downarrow} + \Delta_{sQ-} \psi^{\dagger}_{-\uparrow}\psi^{\dagger}_{-\downarrow} + \text{h.c.}, \tag{1.110}$$

$$\frac{\mathrm{d}}{\mathrm{d}s}\begin{pmatrix}\Delta_{s1}\\ \Delta_{s2}\end{pmatrix} = d_0 \begin{pmatrix}-\lambda_4 & 0\\ 0 & -\lambda_4\end{pmatrix}\begin{pmatrix}\Delta_{s1}\\ \Delta_{s2}\end{pmatrix}, \tag{1.111}$$

$$\alpha_{sP_Q} = \lambda_4, \tag{1.112}$$

$$\alpha_{s_{\pm}P_Q} = \lambda_4. \tag{1.113}$$

Summing up all the susceptibilities above:

$$\alpha_{sP_Q} = 2\lambda_4^0, \tag{1.114}$$

$$\alpha_{s_{\pm}P_Q} = 2\lambda_4^0, \tag{1.115}$$

$$\alpha_{CDW} = 6(2\lambda_1^0 - \lambda_2^0), \tag{1.116}$$

$$\alpha_{SDW} = -6\lambda_2^0, \tag{1.117}$$

$$\alpha_{\text{spin}} = -2(\lambda_1^0 + \lambda_4^0), \tag{1.118}$$

$$\alpha_{\text{charge}} = 2(-\lambda_1^0 + 2\lambda_2^0 + \lambda_4^0), \tag{1.119}$$

$$\alpha_{sP} = 6(-\lambda_1^0 + \lambda_2^0), \tag{1.120}$$

for finite momentum s-wave and $s_\pm$-wave superconducting, charge density wave, spin density wave, ferromagnetic (uniform spin), uniform charge (κ), and s-wave superconducting instabilities respectively.

1.6.3 RG flow analysis

Going back to the analysis of RG flow (1.92), since λ_1 cannot change sign (RHS for $\dot{\lambda}_1$ is equal to zero when $\lambda_1 = 0$), it is convenient to analyze the RG flow in $y_2 = \lambda_2/\lambda_1$ *vs.* $y_4 = \lambda_4/\lambda_1$ coordinates,

$$\dot{y}_2 = \lambda_1 \left(-3 + 6y_2 + 2y_4 - 4y_2 y_4\right), \tag{1.121}$$

$$\dot{y}_4 = \lambda_1 \left(1 + 2y_2 + 6y_4 - 2(y_2^2 + y_4^2)\right). \tag{1.122}$$

We can then reparametrize the RG flow eliminating λ_1 to get a system of equations

$$y_2' = -3 + 6y_2 + 2y_4 - 4y_2 y_4, \tag{1.123}$$

$$y_4' = 1 + 2y_2 + 6y_4 - 2(y_2^2 + y_4^2), \tag{1.124}$$

that can be solved exactly in the coordinates $y_\pm$,

$$y_\pm = (y_4 - 3/2) \pm (y_2 - 1/2): \quad y_\pm' = 6 - y_\pm^2. \tag{1.125}$$

This allows us to identify all phases and phase boundaries on the $y_2 y_4$ plane. Thus, the plot in λ_2/λ_1 *vs.* λ_4/λ_1 coordinates explicitly shows the fate of the system for different initial coupling constants. Fig. 1.11 (left) shows the phase diagram of RG flow for $\lambda_1 > 0$. Ferromagnetic (FM), superconducting (SC) and competing spin/charge-density-wave ([S/C]DW) instabilities are possible with phase boundaries

$$\lambda_2 - \lambda_1/2 = 0, \quad \text{(SC/SDW)} \tag{1.126}$$

$$\lambda_2 + \lambda_4 - (2 - \sqrt{3})\lambda_1 = 0, \quad \text{(FM/SC)} \tag{1.127}$$

$$\lambda_2 - \lambda_4 - (\sqrt{3} - 1)\lambda_1 = 0, \quad \text{(FM/[S/C]DW)} \tag{1.128}$$

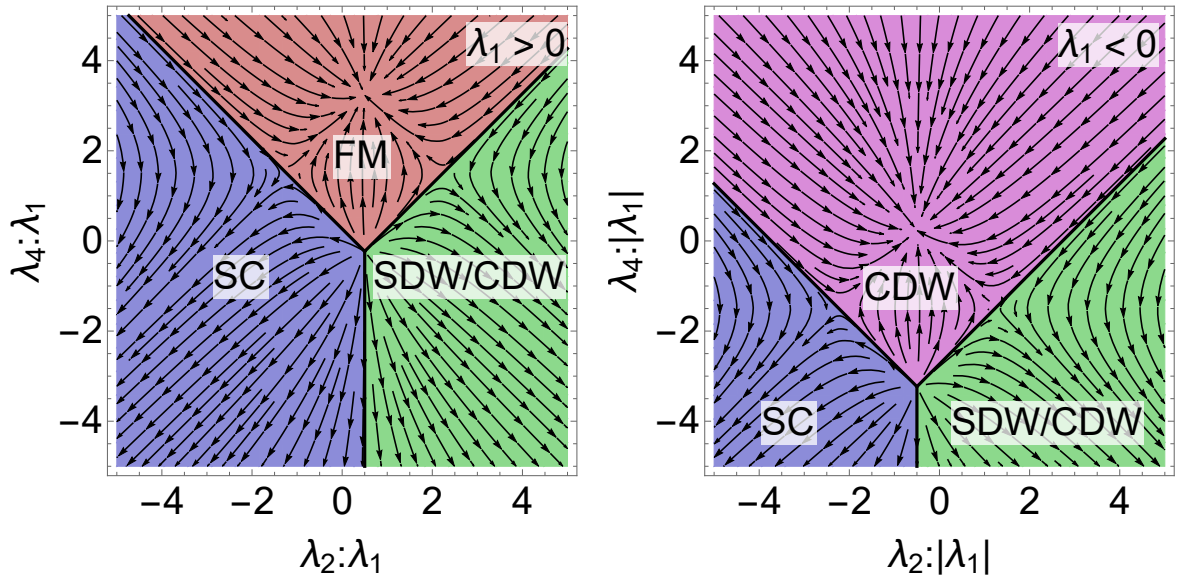

Figure 1.11: *RG phase diagram showing a leading instability as a function of initial coupling constants. The figure on the left shows the case of positive $\lambda_1 > 0$, while the one on the right corresponds to $\lambda_1 < 0$. (λ_1 never changes sign under the RG flow.) There are four possible instabilities: SC superconducting, ferromagnetic (FM), charge-density wave (CDW) and a competing spin/charge-density-wave (SDW/CDW). The Hubbard model initial conditions $\lambda_1 = \lambda_2 = \lambda_4 > 0$ lead to the development of FM instability.*

and the lines cross at the point

$$\lambda_1 : \lambda_2 : \lambda_4 = 2 : 1 : (3 - \sqrt{12}). \tag{1.129}$$

For negative values $\lambda_1 < 0$ we get options of SC, CDW, and [S/C]DW and Fig. 1.11 (right). The phase boundaries are now

$$\lambda_2 + |\lambda_1|/2 = 0, \quad \text{(SC/[S/C]DW)} \tag{1.130}$$

$$\lambda_2 + \lambda_4 - (2 - \sqrt{3})\,|\lambda_1| = 0, \quad \text{(SC/CDW)} \tag{1.131}$$

$$\lambda_2 - \lambda_4 - (\sqrt{3} - 1)\,|\lambda_1| = 0, \quad \text{(CDW/[S/C]DW)} \tag{1.132}$$

crossing at the point

$$|\lambda_1| : \lambda_2 : \lambda_4 = 2 : 1 : (3 - \sqrt{12}). \tag{1.133}$$

The crucial difference with the case of a single monkey saddle is that the solution $\lambda_1 = \lambda_2 = 0$ describing two decoupled saddles is now always unstable. The analysis of the

RG flow presented above shows that there are four possible many-body instabilities, *s*-wave superconducting (SC), ferromagnetic (FM), charge-density-wave (CDW) and a competing spin/charge-density-wave (SDW/CDW). However, only three instabilities, SC, FM, and SDW/CDW are possible for initially repulsive interactions, as is shown in a Fig. 1.11. For Hubbard model the initial conditions correspond to all interaction constants being equal and positive, $\lambda_i = (\lambda)_0 > 0$, and lead to FM phase.

1.7 X_9 singularity in $Sr_3Ru_2O_7$

Before closing this chapter, in this section we discuss $Sr_3Ru_2O_7$, another candidate material for a higher-order saddle in its electronic dispersion. Unlike BLG where the rotational symmetry C_3 leads to a third order monkey saddle, a C_4 rotational symmetry in $Sr_3Ru_2O_7$ leads to a fourth order saddle. This material has attracted a lot of attention due to the complex magnetic phase diagram that hosts a pair of magnetic phases and a pair of spin-density-wave states, see Fig. (1.12). A most interesting feature is a power-law divergence in specific heat and entropy $\Delta C, \Delta S/T \propto |H - H_c|^{-1}$ that signals a square-root divergence in the DoS of states, $\nu(\varepsilon) \propto |\varepsilon - \varepsilon_c|$. Authors of Ref. [34] discuss that while a quasi-one-dimensional dispersion can produce a required power dependence, it would imply the existence of the divergence only to one side of the band edge. No plausible explanation of the symmetric divergence was suggested so far.

We focus on specific electron bands, γ-bands [35], and argue that given the C_4 rotational symmetry of the crystal, the electron dispersion in the vicinity of the singularity can be described as a fourth order saddle, a symmetry-restricted unimodal parabolic singularity

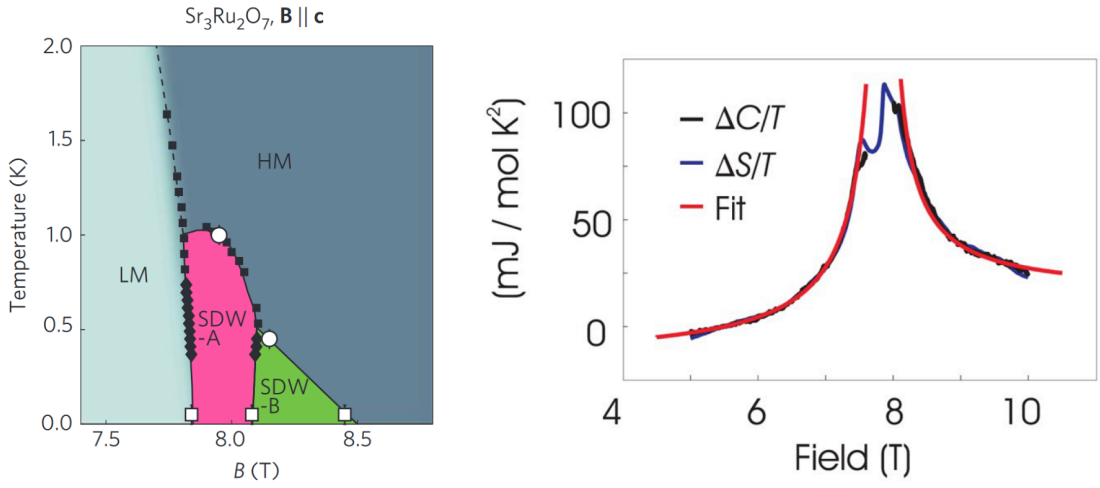

Figure 1.12: *Left: magnetic phase diagram of $Sr_3Ru_2O_7$, showing low- and high-magnetization phases (LM and HM) and two types of spin-density waves. Right: specific heat and entropy in the vicinity of the metamagnetic transition between LM and HM phases shows a $\propto |H - H_m|^{-1}$ divergence. Figures are taken from Refs. [33, 34].*

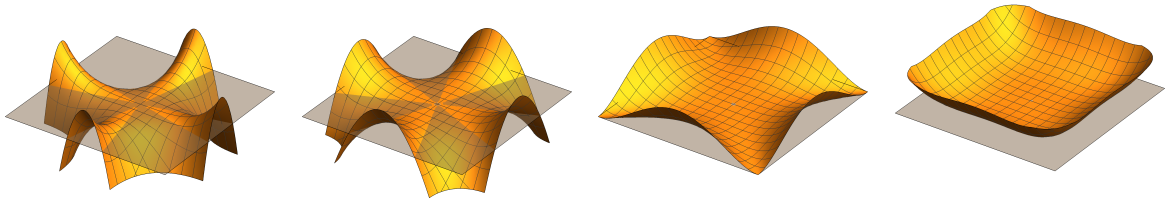

$K = -20$ $K = -6$ $K = -2$ $K = -1/2$

Figure 1.13: *Left: The three dimensional surfaces above are electron dispersions $\varepsilon = \varepsilon(k_x, k_y)$ in the vicinity of the singularity. The grey horizontal plane represents the critical energy of the singularity $\varepsilon = 0$. All values of the modulus $K < -2$ lead to the same topological features. The value of the modulus $K = -6$ corresponds to electron-like and hole-like sections of the same width, a property that is confirmed in the DFT calculation. This implies existence of an additional symmetry in the system, a superposition of the particle-hole transformation $\varepsilon \leftrightarrow -\varepsilon$ and rotation by an angle $\pi/4$. If we increase the value of the modulus, at $K = -2$ the system reaches a critical point and the saddle disappears leaving a singular $\propto p^4$ electronic pocket.*

X_9 in the electronic dispersion $\varepsilon(\boldsymbol{k})$.

From symmetry arguments, the electron dispersion in the vicinity of the singularity can be captured by the dispersion

$$\varepsilon(\boldsymbol{k}) = (k_x^4 + K k_x^2 k_y^2 + k_y^4) + a(k_x^2 + k_y^2) - \mu. \tag{1.134}$$

The core of the singularity is the set of 4th order terms $k_x^4 + K k_x^2 k_y^2 + k_y^4$. This part corresponds to the germ of the singularity, while the remaining terms $(a(k_x^2 + k_y^2) - \mu)$ are the perturbation unfolding the singularity. Unlike simpler singularities, X_9 forms a whole family of singularities parametrized by the modulus K. While a generic singularity from the X_9 family has a co-dimension eight, one modulus and seven control parameters, the presence of the lattice symmetry greatly simplifies the situation leaving only the modulus K and two control parameters a, μ. Moreover, physical properties of the singularity are the same for the whole range $K < -2$ (see Fig. 1.13) and the DFT calculations suggest a value of the modulus close to $K = -6$, see Fig. 1.14. At this special value the low-energy dispersion acquires an additional symmetry that is composed from the particle-hole transformation and rotation by an angle $\pi/4$, with dispersion acquiring especially especially simple form in polar coordinates (k, φ):

$$\varepsilon(\boldsymbol{k})|_{K=-6} = k^4 \cos 4\varphi + a k^2 - \mu. \tag{1.135}$$

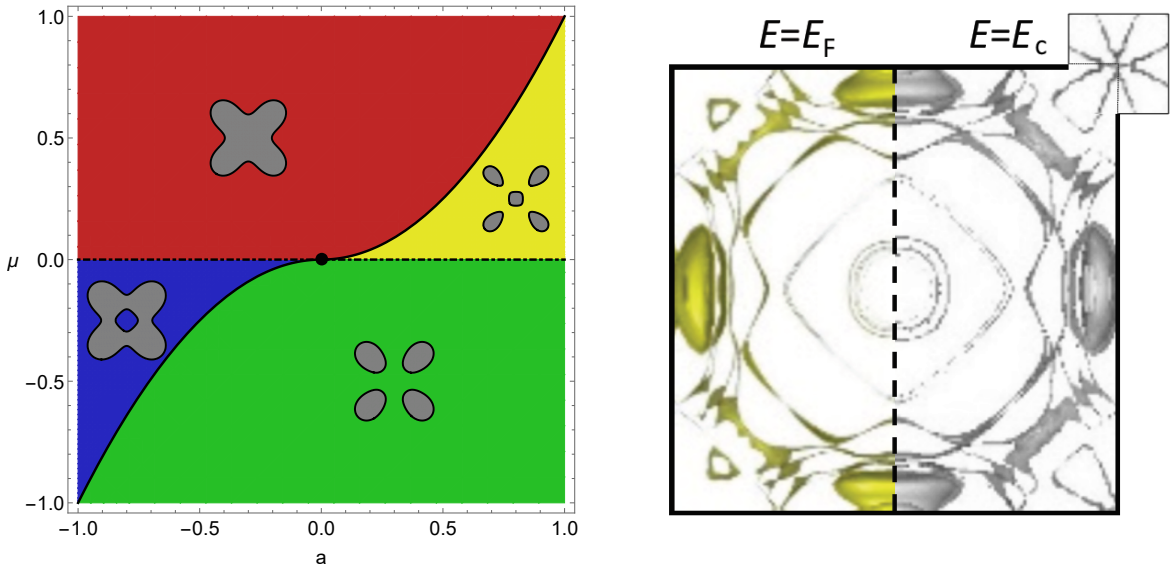

Figure 1.14: *Left: topological phase diagram of the effective model (1.134)) with an added k^8 term to close the Fermi surface. It is very similar to the phase diagram of BLG (Fig. 1.2). In $Sr_3Ru_2O_7$ there is no control over the parameter $a > 0$, so that only green, yellow and red phases are accessible. Right: results of DFT calculation performed by Dmitry Efremov [36]. Shown is the Fermi surface of a single spin species. Yellow color shows the Fermi surface at zero magnetic field and gray shows the Fermi surface near the singularity at $H = 7.8$ T*

The DoS of states of this dispersion has a critical $\propto |\mu|^{-1/2}$ scaling for $a = 0$ and can be summarized as

$$\nu(\mu) \propto \begin{cases} |\mu|^{-1/2}, & |\mu| \gg \mu_c \\ \ln \dfrac{\mu_c}{|\mu - \mu_c|}, & |\mu - \mu_c| \ll \mu_c, \end{cases} \tag{1.136}$$

where the critical value of the chemical potential $\mu_c = a|a|/4$. We present a detailed calculation leading to the result above in the appendix A.1.

1.8 Conclusion

We studied the properties of electronic systems tuned to a monkey saddle singularity, where the dispersion is $\propto p_x^3 - 3p_x p_y^2$. We showed that such a situation occurs in a multicritical Lifshitz point where three van Hove singularities merge. We showed that such a singular point is accessible in bilayer graphene by controlling two parameters, the interlayer bias voltage and the chemical potential. We identified a number of experimentally accessible

features associated with the monkey saddle dispersion when the system is subject to a magnetic field. The Landau level structure has a trademark behavior where $E_m \propto (Bm)^{3/2}$, different from the behavior of both linearly or quadratically dispersing systems. The oscillations of either thermodynamic or transport properties with the applied magnetic field (de Haas-van Alphen or Shubnikov-de Haas oscillations) contain a signature tripling of the oscillation period when the Fermi energy crosses the saddle point energy. This tripling, associated with the topological transition between a single- and three-sheeted Fermi surface, can be viewed as a smoking gun of the monkey saddle singularity.

Generically, the singular electronic dispersion in such multicritical Lifshitz point implies a strong tendency towards development of many-body instabilities. We found that the stronger divergence of the density of states in monkey saddle singularities ($n = 3$), as compared to the case of ordinary van Hove singularities ($n = 2$), brings about crucial simplifications in the field theoretical analysis of the effect of interactions. We showed that the theory for systems with higher order singularities ($n > 2$) is super-renormalizable. Thus, in contrast to the case of van Hove singularities where a renormalization group analysis requires two cut-off scales to properly account for the singular and non-singular parts of the Fermi surface, the analysis of higher order saddles requires no large momentum cut-off, since there are only infrared divergences, which are regularized by temperature T and chemical potential μ.

Via renormalization group analysis of the super-renormalizable theory, we showed that the non-interacting electron fixed point of a system with a single monkey saddle is unstable to interactions, developing either a superconducting instability or non-Fermi liquid behavior. We also showed that the electronic lifetime depends crucially on the symmetry of the dispersion, with odd and even saddles displaying non-Fermi-liquid and marginal Fermi liquid behavior, respectively. For bilayer graphene, which has two non-nested monkey saddles at the K and K' points, we showed that interactions (depending on their nature) lead to s-wave superconductivity, ferromagnetism, charge-density wave, or spin-density wave.

The studies of multicritical Lifshitz points in electronic systems suggest an exciting link

to catastrophe and singularity theories. Namely, the monkey saddle could be considered as a lattice-symmetry-restricted elliptical umbilic elementary catastrophe D_4^-. Catastrophe theory may be a useful language to classify the different possible singularities where Fermi surface topology changes. The relevant classification at criticality is not that of the Fermi surface topologies, but of the singularity itself. Controlling the chemical potential and the interlayer bias voltage in bilayer graphene is a clear example of how to engineer a catastrophe in an electronic system, the monkey saddle. Crystalline symmetries may reduce the possible types of catastrophes in the ADE classification that could be realized in solid state systems. We showed that $Sr_3Ru_2O_7$ is another example of the system with a singularity in electronic dispersion. Remarkably, it displays an X_9 singularity that falls outside of the ADE classification and is an example of a degenerate singularity, being in fact a whole family of singularities. Which other singularities could occur in electronic systems remains an open problem. However, our analysis of the physical consequences of such singularities should be applicable to other types of catastrophes in systems of electrons.

Chapter 2

Topological electronic properties of silicon

2.1 Introduction

The experimental discovery of the integer quantum Hall effect [37], where the Hall resistance is quantized to the extraordinary precision of one part in a billion, led to the new standard of resistance for the international system of units. A degree of precision such as this has its roots in a fruitful confluence of physics and mathematics, which ties the Hall resistance to a topological quantity. In the case of the integer Hall effect, this quantity is the first Chern number associated to each filled Landau level [38]. The integer Hall effect was the first example of a system with topological electronic properties; the number of systems in which topology plays a prominent role has grown explosively in the recent past, fueled by the discovery of a new class of topological band insulators occurring in semiconductors with strong spin-orbit coupling, in which gapless surface states exist [39, 40, 41, 42, 43, 44, 45, 46, 47, 48, 49, 50, 51, 52] (for reviews, see Refs. [53, 54].) After the discovery of topological insulators, many examples of topological semimetals were identified, such as Weyl metals [55, 56, 57, 58, 59, 60, 61] and systems with Weyl nodal lines [55, 62], and nodal chains [63].

Spin-orbit interactions play a prominent role in the topological insulators and Weyl systems, but spin-orbit coupling is not central to the understanding of the basic electronic properties of silicon. Indeed, in the standard classification of topological insulators, silicon is not classified [64] as one with protected Dirac surface states. Therefore, silicon thus far has sat on the sidelines. Here we show that the sublattice structure of crystals such as silicon is responsible for a network of Berry flux lines in the Brillouin zone that link at points of high symmetry in momentum space. This Berry flux network is topologically stable, obeys ice rules (two in, two out) at the X points, and is responsible for topological protection of degeneracies along the X-W direction. The nontrivial topological structure of the Berry flux network in silicon shares the same physical origin as the Berry flux in graphene: the fact that there are two atoms in the unit cell gives rise to a spinor structure with associated Berry phases. The existence of the Berry flux network opens a novel "topological knob" to manipulate electrons in silicon, especially in light of progress made in the past decade from studying the effects of Berry phases in the electronic properties in graphene.

The presentation of the results in this chapter is organized as follows. In Sec. 2.2 we identify the spinor structure and the Berry flux within a general tight-binding approximation (valid for an arbitrary number of orbitals). We argue based on topological and symmetry arguments that the Berry flux network is robust and remains beyond the tight-binding description of silicon. In Sec. 2.3 we derive an effective two-band Hamiltonian that describes key topological properties of silicon. We also argue that it corresponds to a simple toy tight-binding model with just two s-orbitals per site. In Sec. 2.4 we point out a bulk-boundary correspondence, and existence of topological drumhead states in both the toy model and real silicon that follows from the bulk band topology. Such connection is in a close analogy with a physics of nodal-line and nodal-chain semimetals. In Sec. 2.5 we perform a numerical analysis of a thin silicon slab to find energy disperion of drumhead states within sp^3s^* model. We suggest that the valence band drumhead states can be visualized with ARPES. We also consider a silicon quantum well with a large voltage bias and show that in certain regimes drumhead states dominate low-energy behavior of the system. We close the chapter

by summarizing the results and discussing open problems in Sec. 2.6.

2.2 Berry flux network

A tight-binding Hamiltonian for a system on a bipartite lattice comprised of sublattices A and B can be represented as

$$H(\mathbf{k}) = \begin{bmatrix} H_{AA}(\mathbf{k}) & H_{AB}(\mathbf{k}) \\ H_{BA}(\mathbf{k}) & H_{BB}(\mathbf{k}) \end{bmatrix}, \tag{2.1}$$

where the blocks H_{AA} and H_{BB} contain hoppings between sites in the same sublattice, and the blocks H_{AB} and $H_{BA} = H_{AB}^{\dagger}$ contain hoppings between sites is different sublattices. The size of these blocks depend on the number of orbitals included in the tight-binding model. For example, in graphene the blocks are 1×1 if one considers only the π-orbital, and in silicon the blocks are 4×4 if one takes account of only the s, p_x, p_y, p_z orbitals (or 5×5 in the sp^3s^* model [65], with the inclusion of the s^* orbital). The diagonal blocks are periodic in $\mathbf{k}$-space: $H_{AA}(\mathbf{k}) = H_{AA}(\mathbf{k} + \mathbf{G}_i)$ and $H_{BB}(\mathbf{k}) = H_{BB}(\mathbf{k} + \mathbf{G}_i)$, where $\mathbf{G}_i$ ($i = 1, \ldots, d$) is a reciprocal lattice basis vector ($d = 2$ for graphene, $d = 3$ for silicon). The matrix elements of the off-diagonal blocks are written as

$$[H_{AB}(\mathbf{k})]_{\alpha\beta} = -\sum_{\mu} t_{\alpha\beta}(\mathbf{d}_\mu)\, e^{i\mathbf{k}\cdot\mathbf{d}_\mu}, \tag{2.2}$$

where the vectors $\mathbf{d}_\mu$ connect the atoms from A to B, and the $t_{\alpha\beta}(\mathbf{d}_\mu)$ contain the overlap of the orbitals α and β separated by $\mathbf{d}_\mu$. Because the vectors $\mathbf{d}_\mu$ are not Bravais lattice vectors, $\mathbf{d}_\mu \cdot G_i$ is generically not a multiple of 2π, and therefore the off-diagonal blocks H_{AB} and H_{BA} are *not* periodic in $\mathbf{k}$-space. An attempt to gauge out these non-periodicities comes with the price of adding singularities (branch cuts) to the phase of the wave function in momentum space.

In graphene the vectors $\mathbf{d}_\mu$, $\mu = 0, 1, 2$, point to the vertices of a triangle, while in silicon the $\mathbf{d}_\mu$, $\mu = 0, 1, 2, 3$, point to the vertices of a tetrahedron. In these lattices (see Appendix B), it follows that $H_{AB}(\mathbf{k} + \mathbf{G}_i) = e^{i\Phi(\mathbf{G}_i)}\, H_{AB}(\mathbf{k})$, where $\Phi(\mathbf{G}_i) = 2\pi/N$, with $N = 3$ and $N = 4$

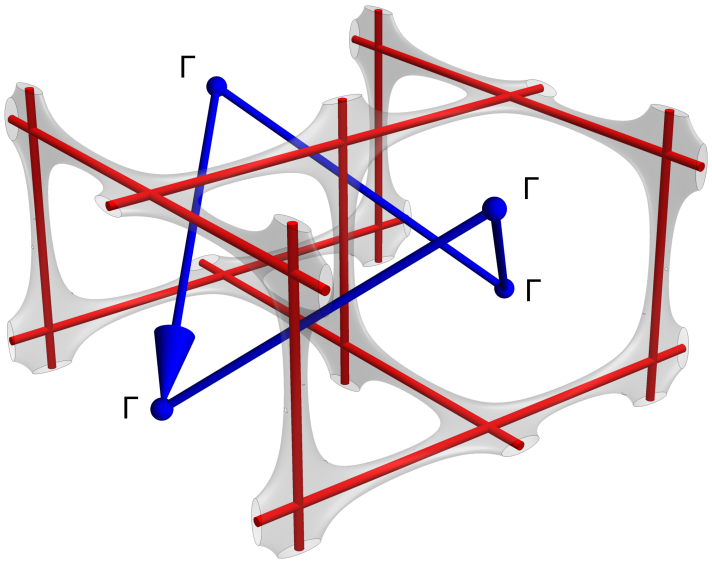

Figure 2.1: A loop in k-space encircling a single π-flux line. *A Berry flux network in* **k***-space is schematically shown in red color with the grey surface guiding the visualization of the flux flow. Blue color represents a* $\mathbf{0}$–$\mathbf{G}_1$–$(\mathbf{G}_1+\mathbf{G}_2)$–$(\mathbf{G}_1+\mathbf{G}_2+\mathbf{G}_3)$–$\mathbf{0}$ *walk that we use to argue the existence of the Berry* π*-flux/Dirac line piercing this loop.*

for the graphene and silicon lattices, respectively. The Hamiltonian $H(\mathbf{k})$ is not periodic in $\mathbf{k}$-space; however, it is periodic *up to* a gauge transformation that rotates the amplitudes on the two sublattices by opposite phases:

$$H(\mathbf{k}+\mathbf{G}_i) = U(\mathbf{G}_i)\, H(\mathbf{k})\, U^{\dagger}(\mathbf{G}_i)\,, \tag{2.3}$$

with

$$U(\mathbf{G}_i) = e^{\,\mathrm{i}\frac{1}{2}\Phi(\mathbf{G}_i)\,\sigma_z}, \tag{2.4}$$

and σ_z a Pauli matrix acting on the A/B sublattice grading. It follows from Eq. (2.3) that the eigenenergies $\epsilon(\mathbf{k}) = \epsilon(\mathbf{k}+\mathbf{G}_i)$, as expected. However, the spinor structure and the lack of periodicity of the matrix Hamiltonian $H(\mathbf{k})$ (not just its eigenvalues) is what leads to the Berry π-vortices at the K points in graphene, and the Berry π-flux network that we uncover in this work. (In the Appendix B we illustrate how the generic framework above recovers the familiar results in graphene as a warm up for the calculations in silicon.)

Consider the walk in $\mathbf{k}$-space that visits, in order, the points $\mathbf{k}, \mathbf{k}+\mathbf{G}_1, \mathbf{k}+\mathbf{G}_1+\mathbf{G}_2, \mathbf{k}+\mathbf{G}_1+\mathbf{G}_2+\mathbf{G}_3$ and back to $\mathbf{k}$. This walk passes through 4 of the 6 edges of the tetrahedron

formed by the four points in **k**-space, closing a loop. We choose the initial point not to be one of high symmetry, to avoid that the edges pass through band crossings, thus avoiding degeneracies along the walk. For example, one may choose to start close to but not at the Γ point, say at $\mathbf{k} = (\delta_x, \delta_y, \delta_z)$, with infinitesimal $\delta_{x,y,z}$. At the end of the walk, the Hamiltonian returns to $H(\mathbf{k})$, but the eigenvector is rotated by the sequence of unitary operations

$$U(-\mathbf{G}_1 - \mathbf{G}_2 - \mathbf{G}_3)\, U(\mathbf{G}_3)\, U(\mathbf{G}_2)\, U(\mathbf{G}_1) = e^{\,\mathrm{i}\pi\,\sigma_z} = -\mathbb{I}\,, \tag{2.5}$$

which amounts to a rotation by π. This geometric phase implies the existence of π-flux lines in **k**-space, which pierce the loop we described above. An example of a π-flux network that threads the 4-edged loop in **k**-space is shown in Fig. 2.1, which, as we show below, corresponds to the case of the conduction band in silicon.

These singular flux lines are stable, and cannot be removed by small deformations. Silicon is inversion symmetric, which implies that the Berry curvature $B(\mathbf{k}) = B(-\mathbf{k})$; in the absence of time-reversal breaking perturbations, $B(\mathbf{k}) = -B(-\mathbf{k})$. These two symmetries, together, imply that the Berry curvature vanishes everywhere with the possible exception of singular lines carrying flux multiple of π, like those we identified above. These two symmetries thus ensure that the π-flux cannot spread over a finite region, and thus remains singular and contained within a network of flux lines circulating around the Brillouin zone. The number of orbitals in the description of the system does not alter our conclusions based on the topological constraints imposed by Eq. (2.5).

To visualize the network of fluxes in silicon, we consider explicitly the 5-orbital sp^3s^* nearest-neighbor tight-binding model [65]. This model captures essential features of silicon's band structure; in particular, it reproduces the conduction band minimum along the Δ line connecting the Γ and X points in the Brillouin zone. In this approximation, sites within the same sublattice are not connected, so that diagonal blocks simply contain the on-site potential energies $H_{AA/BB} = \mathrm{diag}(E_s, E_p, E_p, E_p, E_{s^*})$, while the inter-sublattice hoppings

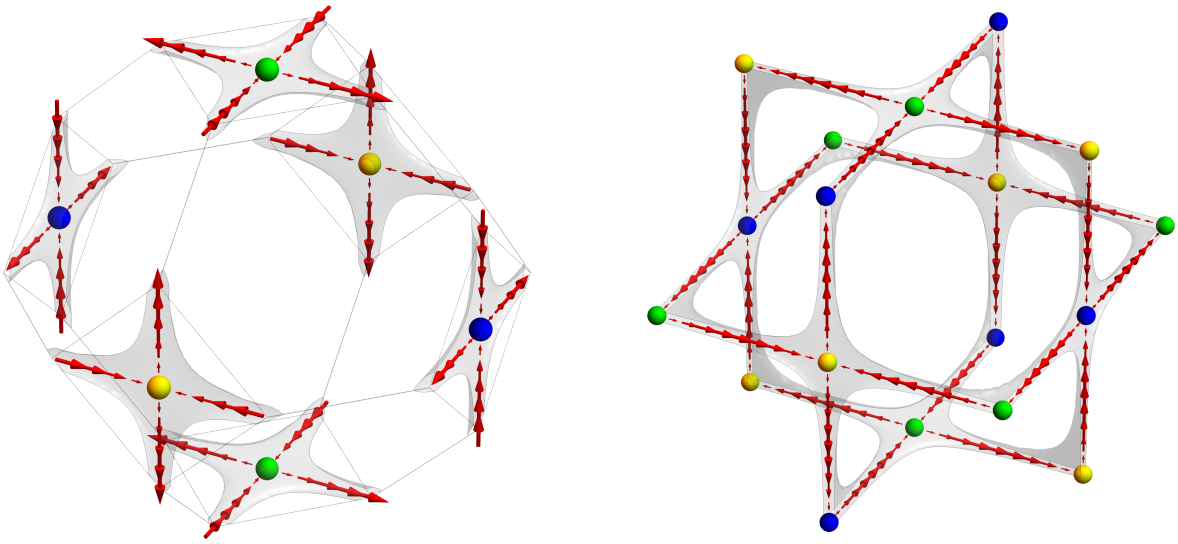

Figure 2.2: Berry curvature field. *Left: a single first Brillouin zone. Right: a doubled Brillouin zone. The colored spheres represent three inequivalent X points. The grey surface guides the visualization of the flux flow and the ice-rule links at the X points.*

contain the non-trivial momentum dependence:

$$H_{AB}(\mathbf{k}) = \begin{bmatrix} V_{ss}\, g_0(\mathbf{k}) & V_{sp}\, g_1(\mathbf{k}) & V_{sp}\, g_2(\mathbf{k}) & V_{sp}\, g_3(\mathbf{k}) & 0 \\ -V_{sp}\, g_1(\mathbf{k}) & V_{xx}\, g_0(\mathbf{k}) & V_{xy}\, g_3(\mathbf{k}) & V_{xy}\, g_2(\mathbf{k}) & -V_{s^*p}\, g_1(\mathbf{k}) \\ -V_{sp}\, g_2(\mathbf{k}) & V_{xy}\, g_3(\mathbf{k}) & V_{xx}\, g_0(\mathbf{k}) & V_{xy}\, g_1(\mathbf{k}) & -V_{s^*p}\, g_2(\mathbf{k}) \\ -V_{sp}\, g_3(\mathbf{k}) & V_{xy}\, g_2(\mathbf{k}) & V_{xy}\, g_1(\mathbf{k}) & V_{xx}\, g_0(\mathbf{k}) & -V_{s^*p}\, g_3(\mathbf{k}) \\ 0 & V_{s^*p}\, g_1(\mathbf{k}) & V_{s^*p}\, g_2(\mathbf{k}) & V_{s^*p}\, g_3(\mathbf{k}) & 0 \end{bmatrix}, \tag{2.6}$$

where momentum functions

$$\begin{aligned} g_0(\mathbf{k}) &= \frac{1}{4}\left(e^{i\mathbf{d}_0\cdot\mathbf{k}} + e^{i\mathbf{d}_1\cdot\mathbf{k}} + e^{i\mathbf{d}_2\cdot\mathbf{k}} + e^{i\mathbf{d}_3\cdot\mathbf{k}}\right), \\ g_1(\mathbf{k}) &= \frac{1}{4}\left(e^{i\mathbf{d}_0\cdot\mathbf{k}} + e^{i\mathbf{d}_1\cdot\mathbf{k}} - e^{i\mathbf{d}_2\cdot\mathbf{k}} - e^{i\mathbf{d}_3\cdot\mathbf{k}}\right), \\ g_2(\mathbf{k}) &= \frac{1}{4}\left(e^{i\mathbf{d}_0\cdot\mathbf{k}} - e^{i\mathbf{d}_1\cdot\mathbf{k}} + e^{i\mathbf{d}_2\cdot\mathbf{k}} - e^{i\mathbf{d}_3\cdot\mathbf{k}}\right), \\ g_3(\mathbf{k}) &= \frac{1}{4}\left(e^{i\mathbf{d}_0\cdot\mathbf{k}} - e^{i\mathbf{d}_1\cdot\mathbf{k}} - e^{i\mathbf{d}_2\cdot\mathbf{k}} + e^{i\mathbf{d}_3\cdot\mathbf{k}}\right), \end{aligned} \tag{2.7}$$

and $\mathbf{d}_0 = \frac{a}{4}(1\,1\,1)$, $\mathbf{d}_1 = \frac{a}{4}(1\,\bar{1}\,\bar{1})$, $\mathbf{d}_2 = \frac{a}{4}(\bar{1}\,1\,\bar{1})$, and $\mathbf{d}_3 = \frac{a}{4}(\bar{1}\,\bar{1}\,1)$, with $a = 5.4310$Å. The interaction parameters in the Hamiltonian are (in eV) $E_s = -4.20$, $E_p = 1.72$, $E_{s^*} = 6.69$, $V_{ss} = -8.30$, $V_{sp} = 5.73$, $V_{s^*p} = 5.38$, $V_{xx} = 1.72$, $V_{xy} = 4.58$ [65]. The resulting band structure is shown

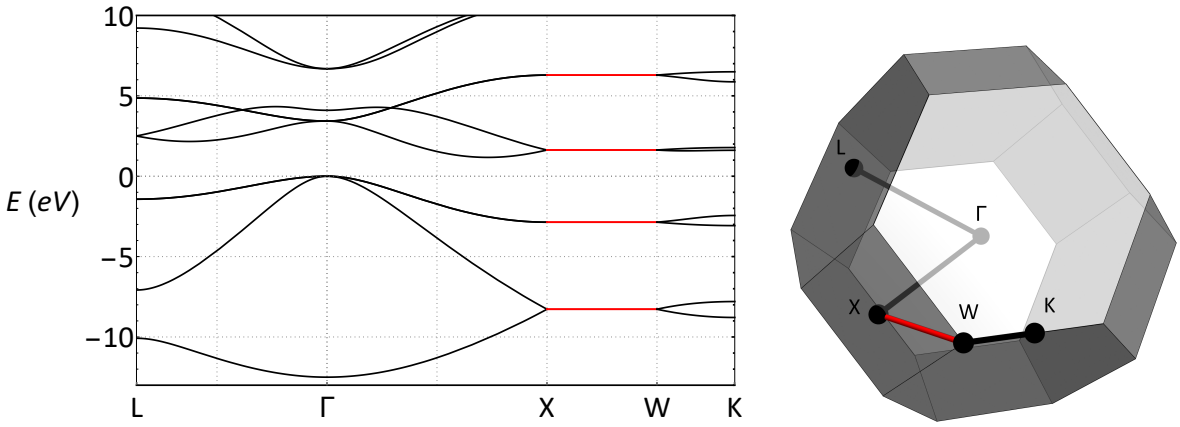

Figure 2.3: Electronic band structure of silicon within the sp^3s^* model. *Left: all bands exhibit a two-fold degeneracy along the X-W line (highlighted in red). This degeneracy may be used as evidence for the existence of the Dirac lines along the X-W direction. Right: first Brillouin zone with points of high symmetry.*

in Fig. 2.3.

This spectrum has an intricate set of lines along which the spectrum is twofold degenerate, in particular along the Z line connecting the X and W points, which is consistent with the O_h^7 crystal symmetry of silicon [66]. We argue that these degeneracies, associated with the Berry flux π identified above, correspond to Dirac lines: fixing the longitudinal momentum along the line yields a two-dimensional Dirac Hamiltonian for the transverse degrees of freedom. While the dispersionless nature of these lines along their longitudinal direction is an artifact of the nearest-neighbor tight-binding approximation, the two-fold degeneracy and the Berry π-flux that travels along these lines are robust. We remark that distorting the hoppings would not remove these lines of degeneracy because the π-fluxes are topologically stable; hence topology ensures that there should be lines of degeneracy in silicon even if rotational symmetry is broken but sublattice symmetry is not. (An analogous reasoning holds in graphene, where the nodes are stable even if the hopping matrix elements to the three neighbors are close but unequal.) We find that the lowest conduction band exhibits the simplest pattern of these Berry flux lines, which reduces to a cage-like net of Dirac lines connecting inequivalent X points (going along the Z line through both X and W points), as is shown on the Fig. 2.2. The Dirac lines meet at the X point, forming an

ice-nodal point (Fig. 2.4).

2.3 Effective Hamiltonian near the X point

2.3.1 Degenerate perturbation theory

Since electron energies at the X point come in degenerate pairs, the relevant physics of the two lowest conduction bands (that together are degenerate along the X-W direction) is to be described by an effective 2×2 Hamiltonian. This can be done within the framework of degenerate perturbation theory [67].

In order to derive such an effective Hamiltonian we first diagonalize the full 10×10 Hamiltonian of the sp^3s^* model at the X point to identify pairs of eigenstates corresponding to five degenerate eigenvalues. Then we expand the Hamiltonian in the newfound basis to the second order in momentum (around the X point) to get a matrix of the type

$$H = \begin{bmatrix} \widehat{H}_{I_1} & \widehat{H}_{I_1 I_2} & \dots & \widehat{H}_{I_1 I_5} \\ \widehat{H}_{I_2 I_1} & \widehat{H}_{I_2} & \dots & \widehat{H}_{I_2 I_5} \\ \vdots & \vdots & \ddots & \vdots \\ \widehat{H}_{I_5 I_1} & \widehat{H}_{I_5 I_2} & \dots & \widehat{H}_{I_5} \end{bmatrix}, \tag{2.8}$$

where I_α label groups of degenerate sublevels and H_{I_α} are D_α by D_α matrices with D_α being the degeneracy of a given level group. $\widehat{H}_{I_\alpha I_\beta}$ represent matrix elements between two such groups of levels. In the case of the X point in silicon all degeneracies are twofold and $\{I_1, I_2, I_3, I_4, I_5\} = \{(1,2), (3,4), (5,6), (7,8), (9,10)\}$, the enumeration starting from the lowest valence band. Then within the second-order perturbation theory the effective Hamiltonian describing level group I_α is given by

$$\widehat{H}^{\text{eff}}_{I_\alpha} = \widehat{H}_{I_\alpha} - \sum_{\beta \neq \alpha} \frac{\widehat{H}_{I_\alpha I_\beta} \widehat{H}_{I_\beta I_\alpha}}{E_{I_\alpha} - E_{I_\beta}}. \tag{2.9}$$

Since I_α and I_β are groups of indices, we can also clarify the equation above and expand in

a more explicit form using ordinary level indices m, n, l and the full Hamiltonian H as

$$\left(\widehat{H}^{\text{eff}}_{I_\alpha}\right)_{m,n} = H_{m,n} - \sum_{\beta\neq\alpha} \frac{1}{E_{I_\alpha} - E_{I_\beta}} \sum_{l\in I_\beta} H_{m,l} H_{l,n}, \quad m, n \in I_\alpha. \tag{2.10}$$

Performing this procedure for silicon numerically, we obtain the effective Hamiltonian for bands 5 and 6

$$H^{\text{eff}}_{(5,6)}(\boldsymbol{p}) = \begin{bmatrix} 1.63 + 0.02p_x^2 & 0.29p_y p_z + 0.02ip_x \\ 0.29p_y p_z - 0.02ip_x & 1.63 + 0.02p_x^2 \end{bmatrix}, \tag{2.11}$$

where we expanded Hamiltonian in momentum $\mathbf{k} = (2\pi, 0, 0) + \mathbf{p}$ around one of the X points. This Hamiltonian can be conveniently represented with Pauli matrices:

$$H_X = \varepsilon_0(\mathbf{p})\,\widehat{\sigma}_0 + v_x\, p_x\,\widehat{\sigma}_1 + \kappa_{yz}\, p_y\, p_z\,\widehat{\sigma}_2, \tag{2.12}$$

where $v_x = 0.51$, $\kappa_{yz} = 0.18$, $\varepsilon_0(\boldsymbol{p}) = 1.63 + 0.11\, p_x^2$, and $\widehat{\sigma}_i$ are Pauli matrices. (Energies are measured in eV and momentum in units of $1/a$.) This expression explicitly shows the ice-nodal nature of the X point. For example, in the vicinity of the points $2\pi\,(1, 0, \pm 0.1)$ the Hamiltonian takes the form

$$H_{X\pm\delta} = \tilde{v}_x\, p_x\,\widehat{\sigma}_1 \pm \tilde{v}_y\, p_y\,\widehat{\sigma}_2, \tag{2.13}$$

where $\tilde{v}_x = 0.51$ and $\tilde{v}_y = 0.02$ are electron velocities at the $2\pi(1, 0, \pm 0.1)$ points. This Hamiltonian structure indicates two Dirac lines with opposite chiralities approaching the X point along the z-axis from opposite directions. Similarly, there are two more such lines along the y-axis (see Fig. 2.4).

2.3.2 Toy model

It turns out that all crucial topological properties of the conduction band can be studied within a simple toy model, with a single orbital per site and nearest-neighbor tight-binding

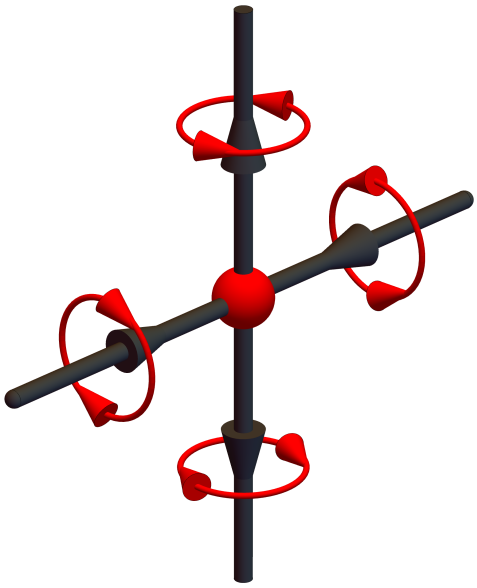

Figure 2.4: Berry flux network near the X point. *The figure shows Dirac lines linking at the X point according to the ice rule 2-in and 2-out. Red loops show the winding of the phase around the lines to visualize the ice rule.*

Hamiltonian

$$\begin{aligned} H_{\text{toy}}(\mathbf{k}) =& t_{nn} \begin{bmatrix} 0 & g_0(\mathbf{k}) \\ g_0^*(\mathbf{k}) & 0 \end{bmatrix} \\ =& t_{nn} \left(\widehat{\sigma}_1 \ \mathrm{Re}\, g_0(\mathbf{k}) + \widehat{\sigma}_2 \ \mathrm{Im}\, g_0(\mathbf{k}) \right). \end{aligned} \tag{2.14}$$

Hopping matrix elements to farther neighbors can be included, especially between the sites of the same sublattice, to reproduce features of silicon's band structure, such as a conduction band minimum along the Δ line. Yet, the topological features are captured by the off-diagonal terms alone: the Hamiltonian is degenerate along the $g_0(\mathbf{k}) = 0$ manifold, yielding essentially the same cage-like net of Dirac lines connecting at X points, just as in the full sp^3s^* model for silicon.

The real and imaginary parts of $g_0(\mathbf{k})$ are

$$\begin{aligned} \mathrm{Re}\, g_0(\mathbf{k}) &= \cos\frac{k_x}{4}\cos\frac{k_y}{4}\cos\frac{k_z}{4}, \\ \mathrm{Im}\, g_0(\mathbf{k}) &= -\sin\frac{k_x}{4}\sin\frac{k_y}{4}\sin\frac{k_z}{4}, \end{aligned} \tag{2.15}$$

from which we identify

$$(2\pi,0,s),\ (2\pi,s,0),\ (0,2\pi,s),\ (s,2\pi,0),\ (0,s,2\pi),\ \text{and}\ (s,0,2\pi)\ \ \text{for}\ s\in[0,2\pi) \tag{2.16}$$

as the set of nodal lines, crossing at the three ice-nodal X points,

$$(2\pi,0,0),\quad (0,2\pi,0),\quad (0,0,2\pi). \tag{2.17}$$

Expanding around one of the ice-nodal points, $\mathbf{k} = (2\pi,0,0) + \mathbf{p}$, we obtain

$$\begin{aligned} \mathrm{Re}\, g_0(\mathbf{k}) &= -\sin\frac{p_x}{4}\cos\frac{p_y}{4}\cos\frac{p_z}{4} \simeq -\frac{1}{4}p_x, \\ \mathrm{Im}\, g_0(\mathbf{k}) &= -\cos\frac{p_x}{4}\sin\frac{p_y}{4}\sin\frac{p_z}{4} \simeq -\frac{p_y p_z}{16}, \end{aligned} \tag{2.18}$$

reproducing the same structure of the X-point effective Hamiltonian derived using the sp^3s^* model:

$$H_{\text{toy, X}} = -V_{AB}\left(\frac{p_x}{4}\widehat{\sigma}_1 + \frac{p_y\,p_z}{16}\widehat{\sigma}_2\right). \tag{2.19}$$

We note that perturbing this toy model Hamiltonian with a $\widehat{\sigma}_3$ term gaps out the Dirac lines (it breaks sublattice symmetry), while a $\widehat{\sigma}_2$ perturbation separates the Dirac lines in different ways depending on the sign of the $\widehat{\sigma}_2$ term, indicating the singular character of the ice-nodal point.

Finally, we gather all results above on the ice-nodal points and combine them with other information inferred from results on the band structure of silicon that is obtained from methods other than tight-binding. We condense this combined information into an effective Hamiltonian near the $(2\pi,0,0)$ nodal point:

$$H_{\text{eff, X}} = \frac{p_x^2}{2m_\ell} + \frac{p_y^2}{2m_t} + \frac{p_z^2}{2m_t} + v_x\,p_x\,\widehat{\sigma}_1 + \kappa\,p_y\,p_z\,\widehat{\sigma}_2\,, \tag{2.20}$$

where $m_\ell = 0.98\,m_e$ and $m_t = 0.19\,m_e$ coincide with the masses from the standard low-energy description of the conduction band (with m_e the electron mass); the velocity $v_x = 0.15\,(2\pi/a)(\hbar/m_\ell)$ is estimated from the location of the conduction band minimum; and κ follows from the dispersion along the X-U direction. This effective Hamiltonian, we claim, captures the topological properties and hence gives a more accurate description of the

low energy states in silicon's conduction band than simply expanding the dispersion to quadratic order near the band minimum. That the minimum occurs close to the X point is captured by the interplay between the Dirac dispersion along the x-direction and the parabolic term, which places the minimum close to the X point (notice that the energy difference between the minimum and the X point is only 0.08eV [67]).

2.4 Surface states and bulk-boundary correspondence

Probably the most important theoretical insight in the field of topological insulators is the fact that non-trivial bulk topology leads to the existence of robust surface states. Recently this idea was extended to topological semimetals, where Fermi surface consists of a nodal loop. In such materials surface states exist only in parts of the surface Brillouin zone that are determined by projecting the nodal loop from the bulk Brillouin zone onto the surface Brillouin zone. Here we argue that the same bulk-boundary correspondence applies to silicon and the existence of the Berry flux "wire frame" leads to the existence of non-trivial topological drumhead surface states.

The two-band toy model Hamiltonian (2.14) is of an archetypal semimetallic form and the manifold $g_0(\mathbf{k}) = 0$ defines a nodal loop. Moreover, this Hamiltonian describes a nodal chain semimetal, a topologically critical system with crossing nodal lines yielding ice-nodal X points [63, 68]. According to the intuition from semimetallic systems [69, 70, 71, 72], the projection of the bulk wire frame onto the surface Brillouin zone breaks it into segments. These segments can be colored with two colors, for example red and blue, in such way that adjacent parts are always of the opposite color. Surface drumhead states then exist in all segments colored either in blue or in red, depending whether the crystal surface is terminated at A or B sublattice. In our case of silicon, the projection of the wire frame breaks down surface Brillouin zone into quadrants. Surface states exist either in first and third or second and fourth quadrants, see Fig. 2.5.

In the nearest neighbor toy model sublattice symmetry protects dispersionless nature of the wire frame and the Fermi Surface at this energy coincides with the wire frame. The same

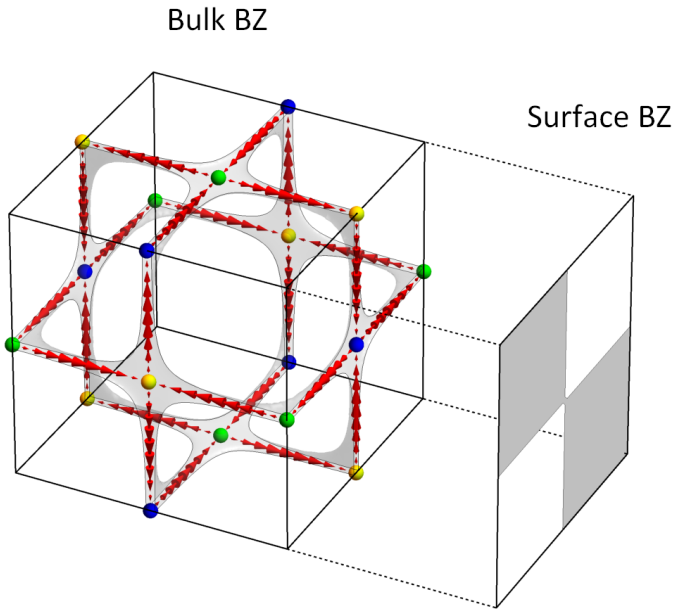

Figure 2.5: Bulk-boundary correspondence within the toy model. *(Doubled) bulk and surface Brillouin zones are topologically related. Bulk wire frame projected on the surface Brillouin zone breaks it into quadrants. Surface drumhead state exists either in first and third or second and fourth, depending whether the crystal surface terminates on A or B sublattice*

happens at the touching of the two lowest valence bands in the sp^3s^* model, see Fig. 2.3. In real silicon, however, $X - W$ line poss nontrivial dispersion. Hopping matrix elements to farther neighbors can be included in order to break sublattice symmetry and reproduce this feature:

$$H_{\text{toy-2}}(\mathbf{k}) = \widehat{\sigma}_0 \left(t_{n^3} v_{n^3}(\mathbf{k}) + t_{n^4} v_{n^4}(\mathbf{k})\right) + t_{nn} \left(\widehat{\sigma}_1 \ \mathrm{Re}\, g_0(\mathbf{k}) + \widehat{\sigma}_2 \ \mathrm{Im}\, g_0(\mathbf{k})\right), \tag{2.21}$$

where

$$v_{n^3}(\mathbf{k}) = \frac{1}{2} \sum_{i \neq j} \cos \frac{k_i a}{2} \cos \frac{k_j a}{2}, \tag{2.22}$$

$$v_{n^4}(\mathbf{k}) = \sum_i \cos(k_i a). \tag{2.23}$$

We allow for both next-nearest-neighbor (n^3) and next-next-nearest-neighbor (n^4) hopping.

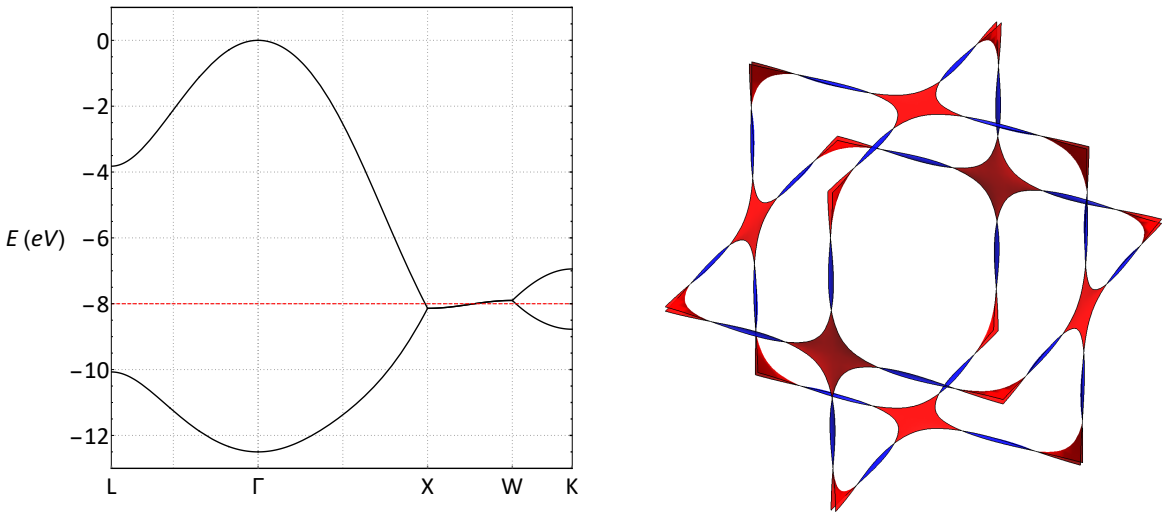

Figure 2.6: Electronic band structure and Fermi surface of the toy model. *Left: Electronic band structure of toy model with next- and next-next-nearest neighbor hoppings included. The latter leads to nontrivial dispersion along X-W line. Right: Fermi surface corresponding to the energy level shown with red dashed line on the left figure. The chosen energy crosses both bands, lower is shown with blue color and upper with red.*

It turns out that n^3 hopping alone is not sufficient to destroy the flatness of dispersion along X-W lines. We fit parameters of the toy model to reproduce Γ, X, W point energies in the lowest valence band of real silicon. The resulting band structure and Fermi surface in the vicinity of the X point are shown in Fig. 2.6.

2.5 Silicon quantum well

2.5.1 Zero Voltage Bias $\Delta V \equiv 0$

The clean and straightforward connection between bulk topology and surface states relies on the sublattice symmetry, which, unfortunately, is destroyed even within the sp^3s^* model. While sp^3s^* model has matrix elements only between A and B sublattices, only two of the ten states are involved in the formation of each wire frame. When the full Hamiltonian is projected on the relevant two dimensional subspace for each wire frame, longer range

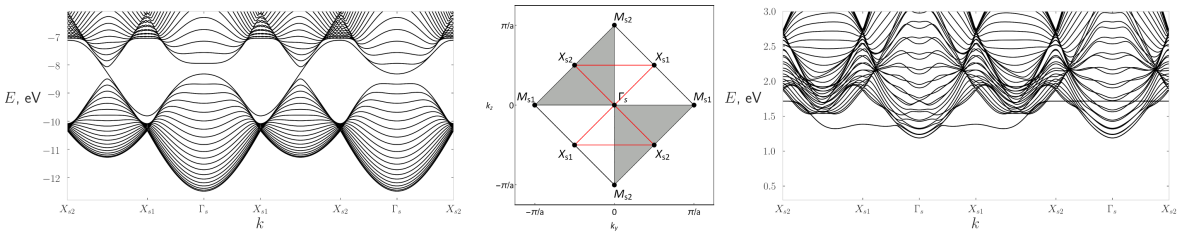

Figure 2.7: Energy dispersion $E(k_y, k_z)$ *within a silicon slab (valence bands on the left and conduction bands on the right). Figure in the center shows surface Brillouin zone with shaded areas (2nd and 4th quadrants) revealing region where a surface state exists within a toy model.*

hopping elements are induced via transitions to the states that were projected out. For example, if we focus on the lowest energy wire frame that is formed by first two bands, next-nearest neighbor element between an A site at the i-th and (i+1)-th cells is formed as

$$-\sum_{\alpha=2\ldots10} \frac{\langle A_i, 1 \,|\, H_{\text{eff}} \,|\, B_i, \alpha\rangle \langle B_i, \alpha \,|\, H_{\text{eff}} \,|\, A_{i+1}, 1\rangle}{(E_\alpha - E_1)^2}. \tag{2.24}$$

Despite this unfortunate fact, the bulk-boundary correspondence and surface states in the toy model are of *topological* nature. Hence, we expect that breaking respective symmetries retains qualitatively bulk-boundary correspondence and surface states for reasonably large perturbations of the toy model.

To explore drumhead states within sp^3s^* model, we perform a numerical calculation of electron dispersion in a silicon slab. We consider a slab of the material with [100] surface and the thickness approximately 10 nm (20 unit cells). The sample is infinite in y, z directions parallel to the surface, for which we perform the Fourier transformation, retaining only the spatial dimension x perpendicular to the surface, so that the electron wavefunction can be factorized as

$$\Psi^{\alpha\mu}(x_i, k_y, k_z) = e^{i(k_y y + k_z z)} \psi^{\alpha\mu}_{k_y,k_z}(x_i), \tag{2.25}$$

where x_i is the position of the i-th unit cell ($i = 1 \ldots 20$), $\alpha = 1, 2$ labels A/B sublattices and $\mu = 1 \ldots 5$ enumerates each of the five orbitals. We find all eigenvalues of the Hamiltonian $E_i(\mathbf{k}_\parallel)$ for each value of the momentum $\mathbf{k}_\parallel = (k_y, k_z)$ parallel to the surface and repeat this procedure along the path $\Gamma_s - X_{s1} - X_{s2}$ within the surface Brillouin zone. The result is shown on the Fig. 2.7. While the exact nature of the bulk-boundary correspondence does

not survive in the five band model, the qualitative connection remains clear.

As we have argued in the previous section, the energy dispersion of silicon in the vicinity of the touching of the lowest valence bands is fairly close to that of the toy model. Largely, this is the case due to other bands well separated in energy from the first two valence bands. To further clarify the connection between the surface states and the bulk topology, we consider a following modification of the sp^3s^* model. We slowly tune interband hopping parameters from 0% to 100%,

$$\left(V'_{sp}(\alpha), \quad V'_{s^*p}(\alpha), \quad V'_{xy}(\alpha)\right) = \alpha \cdot \left(V_{sp}, \quad V_{s^*p}, \quad V_{xy}\right), \tag{2.26}$$

keeping other parameters intact. At $\alpha = 0$ we have five exactly solvable copies of the toy model and for each of them we know that the drumhead states exist and they are of topological nature. This way, by slowly tuning α from 0 to 1, we can track the evolution of the surface state arising from the lowest energy wire frame.

In Fig. 2.8 we zoom into the region between points X_{s2} and X_{s1}, to show a striking robustness of the drumhead state in the full sp^3s^* model. On the top panels, we show the evolution of the spectrum for $\alpha = 0, 0.5$, and 1.0, and on the bottom panels we show the spectrum resulting from further addition of a term that breaks inversion symmetry and opens a gap. Notice that the drumhead states acquire a dispersion as α is turned on, and that the corresponding bandwidth is large. Thus, if one opens a gap that is smaller than that bandwidth (as in the bottom panels), a stable drumhead state remains at the surface, crossing the bulk gap. We remark that the scale of the bandwidth is rather large in the sp^3s^* model, of the order of several eV. In other words, breaking of the chiral symmetry protects the drumhead state against other perturbations that weakly break any other symmetry.

In addition to tracking the α-dependence of the energy spectrum, for each value of α we also calculate the inverse participation ratio defined as

$$\mathrm{ipr}(k_y, k_z) = \sum_i \left|\psi_{k_y,k_z}(x_i)\right|^4. \tag{2.27}$$

For localized states the ipr is inversely proportional to the localization length $\propto 1/l$, while

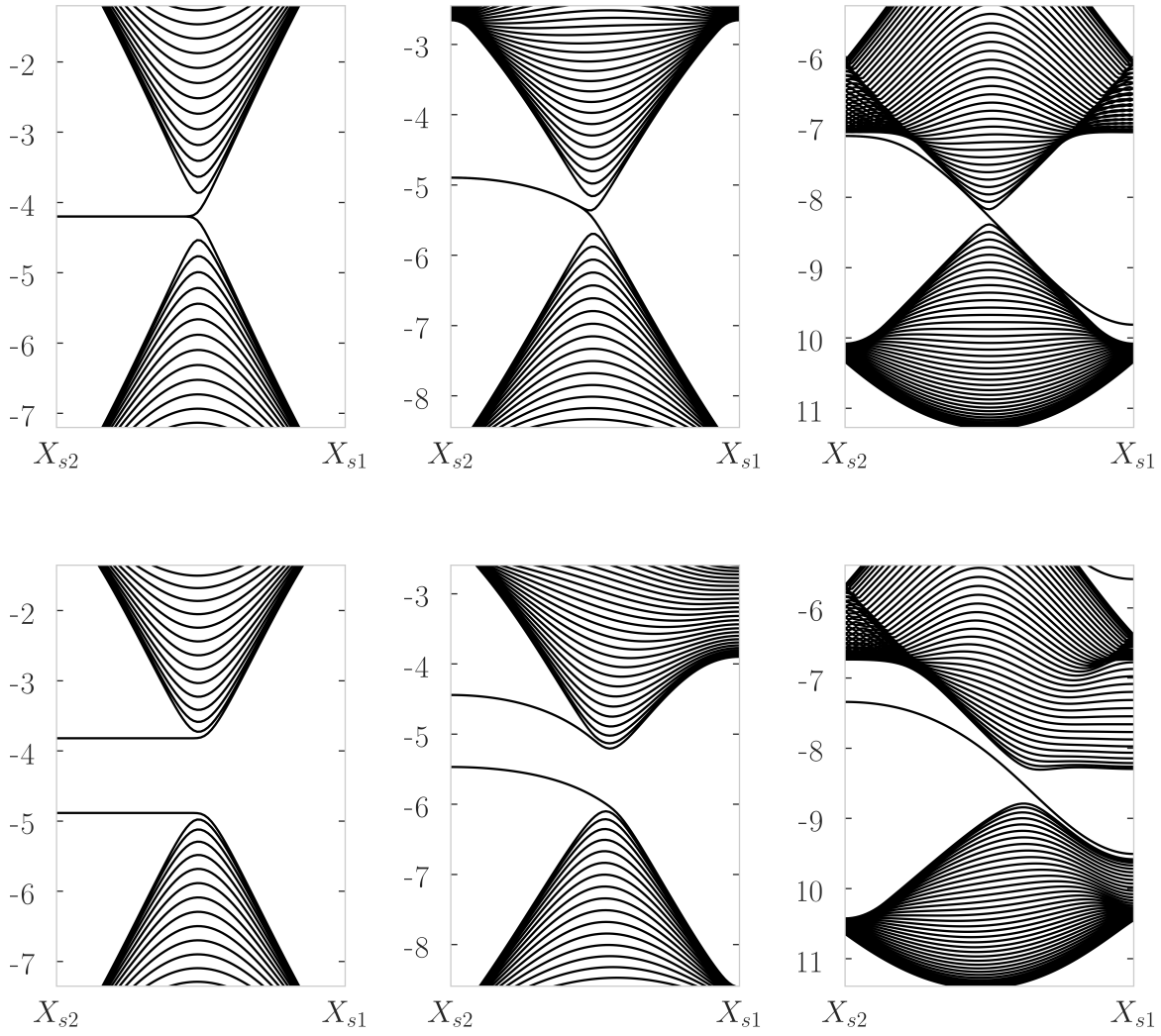

Figure 2.8: Drumhead state dispersion *for different interband interaction strengths* α = 0.0, 0.5, 1.0 *(columns). Bottom row shows dispersion with an additional A/B staggered chemical potential corresponding to opening of 1 eV bulk gap between the first and second valence bands. We increased the number of unit cells to* n = 40 *for the clarity of the presentation.*

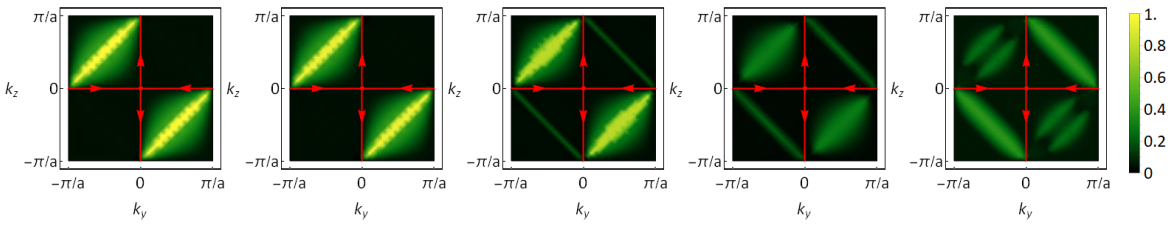

Figure 2.9: Inverse participation ratio *of the surface drumhead state related to the lowest in energy wire frame. The figures are given within the doubled surface Brillouin zone, and the progression from left to right represents tuning of interband interactions from complete absence $\alpha = 0$ to a full sp^3s^* model $\alpha = 1$ (following Eq. (2.26)). The figures are given for $\alpha = 0, 0.25, 0.50, 0.75, 1$. The red cross shows a projection of the bulk wire frame onto the surface Brillouin zone.*

for bulk states it vanishes as $\propto 1/L$, where L is the size of the system. The resulting inverse participation ratios are shown in the Fig. 2.9. Aside from the emergence of new surface states as we tune α, the topological nature this surface state is unambiguous.

2.5.2 Non-Zero Voltage Bias ΔV

As we discuss above, electron states in a silicon slab can be divided into localized (along the $x-$direction) surface states and delocalized bulk states. Application of perpendicular electric field leads to localization of bulk states and formation of the Shockley-type states near the bottom of the conduction band. The conventional theories of MOSFETs focus on such states. However, here we show that in the clean system of a very thin slab geometry it is possible to achieve regime when topological drumhead states dominate low energy behavior of the system.

Since topological surface states are strongly localized at the surface, they are more sensitive to the application of the perpendicular voltage bias. By perturbation theory, voltage bias leads to a linear shift of the surface levels

$$\delta E_{topological} \propto V. \tag{2.28}$$

In contrast, bulk states have a zero first order correction and will experience only quadratic

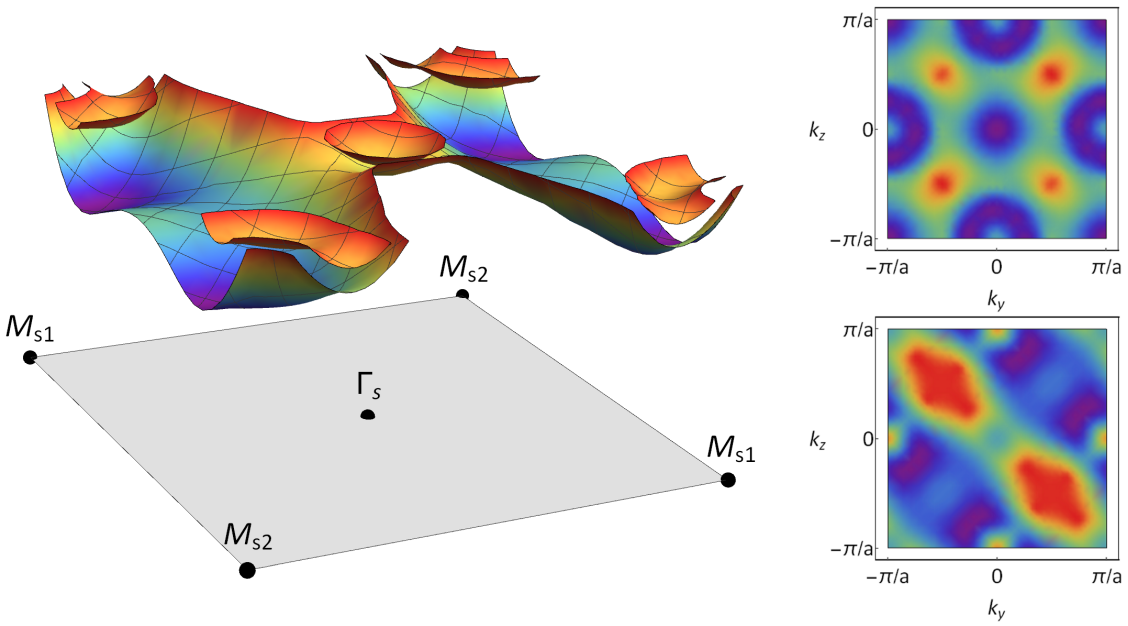

Figure 2.10: *Left: Energy dispersion of the silicon slab with applied voltage. The lowest state is the drumhead state showing a strong anisotropy and only C_2 rotational symmetry. The second state is of a Shockley type is a bulk electron localized by electric field. In contrast to the lowest state, the second state is nearly isotropic at lowest energies. Right: inverse participation ratio for the first and second conduction band surface states (top and bottom respectively).*

shift under the application of the voltage bias

$$\delta E_{non-topological} \propto V^2. \tag{2.29}$$

This means that at small enough thickness of the sample it should be possible to pull down topological surface states to dominate low-energy transport of the system. At stronger fields the scaling (2.29), breaks down, but qualitatively the conclusion remains the same. We verify these speculations numerically and find that they are indeed true.

In this subsection we consider a slab of 20 unit cells to magnify the effects of electric field. Fig. 2.10 shows the energy dispersion of two lowest conduction band states when a voltage bias equal to 50% of the gap is applied, $\Delta V = 0.59$ V. We can see that the drumhead surface state indeed dominates the low energy behavior of the system. Moreover, while the non-topological Shockley-type states have almost perfect C_4 symmetry and are nearly

isotropic at lowest energies, the drumhead state is strongly anisotropic with the rotational symmetry reduced to C_2. Such drastic difference will be readily observable in transport properties of clean intrinsic silicon structures.

2.6 Conclusion

In this work we identified a network of π Berry flux lines in reciprocal space, for silicon. We first constructed a rather general argument, based solely on the existence of two sublattices, to argue that there must be π flux lines independently of how many bands there are. The π flux lines are tied to the spinor structure due to the two sublattices, and the flux cannot spread out because of time-reversal and inversion symmetry. The situation is analogous to what happens in graphene, where the Dirac points carry π flux and cannot be removed perturbatively.

We then identified these lines in a tight-binding model containing 5 orbitals per sublattice (a 10×10 matrix Hamiltonian). We showed explicitly that the π flux lines appear, and identified the X point as a location where flux lines meet. The electronic dispersion near the X point can be described in terms of the Dirac lines analyzed in this chapter.

Flux lines inside the bulk Brillouin zone imply the existence of drumhead surface states, which are confined within the projection of the flux lines onto the surface Brillouin zone. We discussed how the breaking of sublattice symmetry makes the identification of the drumhead states less obvious, but that nevertheless the qualitative connection between bulk-boundary remains.

There are two sets of questions that our work suggests:

- Can one observe all or some of these features experimentally?
- Can the knowledge that these topological features exist in silicon lead to novel electronics in this "old" material?

Regarding the first question, one of the possible tools to probe these flux lines and the dispersion of wire frames is angle resolved photoemission spectroscopy (ARPES). Since the

features we identified are present in all bands of silicon, one can study them in the valence bands, which are accessible in ARPES. If high energy photons are used, not only can one probe electronic states deep inside the valence bands but also use the high penetration depth (here the x-direction) of those photons to map constant energy surfaces as function of k_y and k_z for different k_x. Such techniques are used in Ref. [73], for example. These types of scans would be able to identify the wire frames, providing evidence for the lines of nodes where the flux runs through.

As for addressing the second question, one must find ways to pull the physics of these nodal lines or surface states to the Fermi level. While the Fermi level lies in the gap for intrinsic silicon, one can reach the regime where the Fermi level crosses the conduction band in inversion layers in doped silicon field effect transistors (FETs).

Another possibility is to use undoped silicon, and pull down the surface states by electric fields. States that are already localized at the boundary are more sensitive to potentials caused by an electric field (a linear potential has its largest and smallest values at the boundary). Intrinsic silicon cannot screen the electric field. Once the surface states are pulled to the Fermi level, there should be metallic boundary states. The absence of disorder should lead to high mobilities at these surfaces. While the mechanism described above does not require that the surface states be drumhead ones, we already observe from Fig. 2.7 that the lowest surface band at positive energies is of the drumhead type.

The findings presented in this work reveal novel topological electronic features in the band structure of silicon, one of the best known and most studied materials. That these features had been missed does not signal an accident, but rather suggests that there are a number of topological properties occuring in many, if not most, other materials. The topological features of silicon that we expose provide new impetus to revisit the physics of bulk silicon and two-dimensional electron gases in silicon FETs, particularly in light of what is now known from recent studies of both graphene and topological insulators.

Chapter 3

Superfluid density of a photo-induced superconducting state

3.1 Introduction

The subject of nonequilibrium superconductivity has recently gained much interest, in part due to experiments on photo-induced transient states in $YBa_2Cu_2O_{6+\delta}$ [74], and the subsequent experimental and theoretical progress (see Ref. [75] for a review). In fact, ideas to extend the temperature regime where superconductivity exists by optical excitation have a long history. Their root can be traced back to the pioneering theoretical predictions by Eliashberg and Gor'kov [76, 77], who showed that microwave radiation may assist the formation of the superconducting gap and thus raise the transition temperature T_c. These predictions were later confirmed by experiments [78]. The applied electromagnetic radiation shifts the electronic occupation numbers, extending the temperature regime in which the BCS self-consistency equation has a non-zero solution.

These ideas of population control can also be applied to systems that are not superconductors at equilibrium. It was proposed that superconductivity could be induced in narrow, indirect gap semiconductors, with pairing between electrons in the same band (intraband pairing) [79, 80, 81, 82]. A non-zero superconducting gap was shown to be

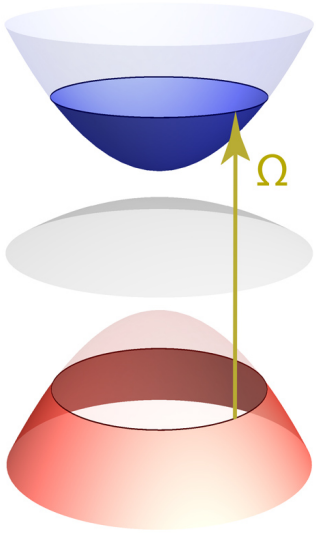

Figure 3.1: *Electrons of a semiconductor are optically pumped from the valence (red) band to the conduction band (blue). In the absence of pumping, i.e. in thermal equilibrium, the conduction band is empty. The laser drive creates a nontrivial steady-state distribution function partially depleting (populating) the valence (conduction) band. Such a population imbalance can also be assisted via an auxiliary band (gray).*

possible with attractive and, notably, with repulsive electronic interactions as well. The latter case is particularly important because repulsion is prevalent in electronic systems. However, in the latter case it was also noted that there was no Meissner effect accompanying the formation of a gap, because the sign of the current response was opposite to that in a standard superconductor: the system would respond as a perfect paramagnet instead of a perfect diamagnet. This strange response, corresponding to a *negative* superfluid density, signals that the state is unstable for repulsive interactions.

Recently, Ref. [83] proposed to use optical pumping to achieve *interband*, rather than intraband, pairing. In this scheme, electrons sitting in two bands at widely different energies and far away from the chemical potential can form interband Cooper pairs in the *s*-wave channel, even in the case of repulsive interactions. (See Fig 3.1 for a sketch of the relevant mechanism.)

In this chapter, we investigate the stability of the corresponding photo-induced interband superconducting state by computing its superfluid density. We find a *positive* superfluid density for repulsive interactions for all parameters (*e.g.*, band curvatures, quasi-particle

populations) where a non-trivial mean-field solution exist. The positivity of the superfluid density implies the stability of the state as well as the existence of a Meissner effect. The latter could be used as a reliable alternative to transport properties to confirm the presence of a nonequilibrium superconducting order in a semiconductor.

of the results in this chapter is organized as follows. In Sec. 3.2 we introduce the system that we study in the present chapter. In Sec. 3.3 we introduce Schwinger-Keldysh formalism that helps us to describe nonequilibrium transport response of the system. In Sec. 3.4 we derive a superfluid density for a general non-equilibrium state with a well-defined quasiparticle distribution function, specializing to the specific steady state in Sec. 3.5. We close the chapter by summarizing the results in Sec. 3.6.

3.2 Model

We consider a two-band semiconductor model with electronic dispersions $E_{1\boldsymbol{p}}$ and $E_{2\boldsymbol{p}}$. The chemical potential of the system is set in the middle of the two bands, see Fig. 3.1. For simplicity, we consider isotropic bands, *i.e.* $E_{\alpha\,\boldsymbol{p}} = E_{\alpha\,-\boldsymbol{p}}$ for $\alpha = 1, 2$. The semiconductor is optically pumped with a broad-band light source, as described in Ref. [83]. In this setup, the optical pumping creates a nonequilibrium distribution of the quasiparticles, which is key to achieve the interband pairing. The semiconductor is coupled to external thermal bath, a necessary condition for a well defined steady state, since external driving continuously injects energy into the system.

3.2.1 Hamiltonian

We consider a two-band Hamiltonian

$$H = H_0 + H_{\text{int}}, \tag{3.1}$$

where H_0 describes non-interacting system,

$$H_0 = \sum\!\!\!\!\!\!\int_{\boldsymbol{p}\alpha} E_{\alpha\boldsymbol{p}} c^{\alpha\dagger}_{\boldsymbol{p}} c^{\alpha}_{\boldsymbol{p}}, \tag{3.2}$$

with $c_p^{\alpha\dagger}$ and c_p^{α} being the fermionic creation and annihilation operators corresponding the electrons in the conduction ($\alpha = 1$) and valence ($\alpha = 2$) bands. To simplify the discussion, we work with spinless electrons. H_{int} describes short-range interaction between electrons of the valence and conduction bands,

$$H_{\text{int}} = V_{\text{int}} \int_{p_1,p_2} c_{p_2}^{2\dagger} c_{p_1}^{2} c_{-p_2}^{1\dagger} c_{-p_1}^{1}, \tag{3.3}$$

with V_{int} being positive for repulsive interactions.

Let us assume that, after a transient regime under the optical pumping, the interband superconducting pairing has already built up. The mean-field description of the system consists in the following Hamiltonian

$$H = \sum\!\!\!\!\!\!\int_{p\alpha} E_{\alpha p} c_p^{\alpha\dagger} c_p^{\alpha} + \frac{1}{2} \sum\!\!\!\!\!\!\int_{p\alpha\beta} \left[c_p^{\alpha\dagger} \Delta (i\sigma_{\alpha\beta}^{y}) c_{-p}^{\beta\dagger} + \text{h.c.} \right], \tag{3.4}$$

where Δ is the s-wave superconducting order parameter to be determined self-consistently, see below. σ^y is the usual Pauli matrix. Without loss of generality, we assume that Δ is real. After introducing the Nambu-Gor'kov spinor notation

$$\Psi_p = \left(c_p^{1}, \quad c_{-p}^{2\dagger} \right), \tag{3.5}$$

the Hamiltonian in Eq. (3.4) can be compactly re-written as

$$H = \int_k \Psi_p^{\dagger} [\varepsilon_p \check{I} + E_p \check{\tau}^z + \Delta \check{\tau}^x] \Psi_p, \tag{3.6}$$

where

$$E_p \equiv (E_{1p} + E_{2p})/2, \quad \varepsilon_p \equiv (E_{1p} - E_{2p})/2, \tag{3.7}$$

and where $\check{I}$, $\check{\tau}^x$, and $\check{\tau}^z$ are the usual identity and Pauli matrices, respectively, in Nambu-Gor'kov space.

The Hamiltonian can be readily diagonalized *via* the following transformations in

Nambu-Gor'kov space

$$\check{U}_p = \exp\left[\frac{\mathrm{i}}{2}\beta_p \check{\tau}_y\right], \text{ with } \tan\beta_p \equiv \frac{\Delta}{E_p}, \tag{3.8}$$

leading to

$$\underline{H} = \int_p \Psi_p^\dagger [\xi_p \underline{\check{\tau}}^z + \varepsilon_p \underline{\check{I}}] \Psi_p, \tag{3.9}$$

with $\xi_p \equiv \sqrt{E_p^2 + \Delta^2}$. We adopt the underlining to indicate the use of the quasiparticle basis.

3.2.2 Self-consistency equation

In this manuscript, we consider a generic steady state with a diagonal quasiparticle distribution function,

$$\left\langle \Psi_p^{\alpha\dagger} \Psi_p^\beta \right\rangle = \check{U}^\dagger \begin{pmatrix} \underline{n}_{1p} & 0 \\ 0 & 1 - \underline{n}_{2p} \end{pmatrix} \check{U}. \tag{3.10}$$

To derive the self-consistency equation, we go back to the original microscopic electron interaction and track the origin of the superconducting pairing in Eq. (3.4) as stemming from an electronic interaction

$$H_{\text{int}} = V_{\text{int}} \int_{p_1,p_2} c_{p_2}^{2\dagger} c_{p_1}^2 c_{-p_2}^{1\dagger} c_{-p_1}^1, \tag{3.11}$$

where V_{int} is positive for repulsive interactions. Within a mean-field treatment, we have

$$H_{\text{int}} = -\int_p \left(\Delta c_p^{2\dagger} c_{-p}^{1\dagger} + \Delta^* c_p^2 c_{-p}^1\right), \tag{3.12}$$

together with a self-consistency equation reading

$$\Delta = V_{\text{int}} \int_p \left\langle c_p^2 c_{-p}^1 \right\rangle. \tag{3.13}$$

Using the explicit form of the distribution function in Eq. (3.10), the self-consistency equation takes a standard form when written in terms of quasiparticle distribution function:

$$1 = \frac{V_{\text{int}}}{2} \int_p \frac{\underline{n}_{1p} + \underline{n}_{2p} - 1}{\xi_p}, \tag{3.14}$$

where $\xi_{\boldsymbol{p}} \equiv \sqrt{E_{\boldsymbol{p}}^2 + \Delta^2}$. The nonequilibrium effects enter through changes of the quasiparticle distribution functions with respect to their equilibrium values,

$$\underline{n}^{\mathrm{eq}}_{1(2)\boldsymbol{p}} = n_{\mathrm{F}}(\varepsilon_{\boldsymbol{p}} \pm \xi_{\boldsymbol{p}}, \mu)\,, \tag{3.15}$$

where $n_{\mathrm{F}}(\epsilon, \mu) = [1 + \exp(-(\epsilon - \mu)/T)]^{-1}$ is the Fermi-Dirac distribution at the temperature T and chemical potential μ. The latter would reproduce the standard BCS self-consistency equation.

3.2.3 Equations of motion for the distribution functions

In the general steady state, the electron distribution function can be parametrized by four parameters,

$$\left\langle \Psi_{\boldsymbol{p}}^{\alpha\dagger} \Psi_{\boldsymbol{p}}^{\beta} \right\rangle = \begin{pmatrix} n_{\boldsymbol{k}}^{11} & s_{\boldsymbol{k}}^{12} \\ s_{\boldsymbol{k}}^{12*} & 1 - n_{-\boldsymbol{k}}^{22} \end{pmatrix}, \tag{3.16}$$

Let us assume that, after a transient regime under the broadband optical pumping, the interband superconducting pairing has already built up. The equations of motion for the distribution function setup by the internal dynamics of the system and by coupling to the reservoir. The former can be computed straightforwardly by commuting the distribution function with the Hamiltonian of the system, while the latter can be boiled down to effective decay rates $\Gamma_{1(2)}$, for electrons in conduction and valence bands. This eventually leads to [83]

$$\begin{aligned} \frac{\mathrm{d}}{\mathrm{d}t} n_{\boldsymbol{k}}^{11} &= \mathrm{i}\Delta s_{\boldsymbol{k}}^{12} - \mathrm{i}\Delta^* s_{\boldsymbol{k}}^{12*} - 2\Gamma_1 \tilde{n}_{\boldsymbol{k}}^{1}, \\ \frac{\mathrm{d}}{\mathrm{d}t} n_{-\boldsymbol{k}}^{22} &= \mathrm{i}\Delta s_{\boldsymbol{k}}^{12} - \mathrm{i}\Delta^* s_{\boldsymbol{k}}^{12*} - 2\Gamma_2 \tilde{n}_{-\boldsymbol{k}}^{2}, \\ \frac{\mathrm{d}}{\mathrm{d}t} s_{\boldsymbol{k}}^{12} &= -\mathrm{i}(2E_{\boldsymbol{k}} - \mathrm{i}\Gamma_{12}) s_{\boldsymbol{k}}^{12} + \mathrm{i}\Delta^* (n_{\boldsymbol{k}}^{11} + n_{-\boldsymbol{k}}^{22} - 1), \end{aligned} \tag{3.17}$$

where the tilded quantities $\tilde{n}_{\boldsymbol{k}}^{\alpha} = n_{\boldsymbol{k}}^{\alpha\alpha} - n_{\mathrm{F}}(E_{\alpha\boldsymbol{k}}, \mu_\alpha)$, and $n_{\mathrm{F}}(E_{\alpha\boldsymbol{k}}, \mu_\alpha)$ are distribution functions in the external thermal bath. We assume that we have two separate reservoirs for the conduction and valence bands that have potentially different chemical potentials μ_α.

In the steady state all time derivatives are zero. The last equation gives a useful relation

$$s_k^{12} = \frac{\Delta^*}{2E_k - i\Gamma_{12}}(n_k^{11} + n_{-k}^{22} - 1), \tag{3.18}$$

making use of it and proceeding with solving equations of motion, we get

$$n_k^{11} + n_{-k}^{22} - 1 = \frac{4E^2 + \Gamma_{12}^2}{4E^2 + \Gamma_{12}^2 + \gamma_* \Delta^2} N_{\mathcal{S}}, \tag{3.19}$$

$$s_k^{12} = \frac{\Delta^*(2E + i\Gamma_{12})}{4E^2 + \Gamma_{12}^2 + \gamma_* \Delta^2} N_{\mathcal{S}}, \tag{3.20}$$

where $N_{\mathcal{S}} = (n_{\mathrm{F}}(E_{1k}, \mu_1) + n_{\mathrm{F}}(E_{2k}, \mu_2) - 1)$ and $\gamma_* = \Gamma_{12}(\Gamma_1^{-1} + \Gamma_2^{-1})$. Only these two quantities, (3.19) and (3.20) are of interest, as we will see below.

Using Eqs. (3.10, 3.16), we get for the matrix quasiparticle distribution function

$$\begin{pmatrix} n_{\underline{1}k} & 0 \\ 0 & 1 - n_{\underline{2}k} \end{pmatrix} = \widehat{U} \begin{pmatrix} n_k^{11} & s_k^{12} \\ s_k^{12*} & 1 - n_{-k}^{22} \end{pmatrix} \widehat{U}^\dagger, \tag{3.21}$$

$$\begin{aligned} n_{\underline{1}k} &= n_k^{11} \cos^2 \frac{\beta}{2} + (1 - n_{-k}^{22}) \sin^2 \frac{\beta}{2} + (\mathrm{Re}\, s_k^{12}) \sin\beta, \\ 1 - n_{\underline{2}k} &= n_k^{11} \sin^2 \frac{\beta}{2} + (1 - n_{-k}^{22}) \cos^2 \frac{\beta}{2} - (\mathrm{Re}\, s_k^{12}) \sin\beta. \end{aligned} \tag{3.22}$$

As we have already mentioned, only the following combination is of interest,

$$n_{\underline{1}k} + n_{\underline{2}k} - 1 = (n_k^{11} + n_{-k}^{22} - 1)\cos\beta + 2(\mathrm{Re}\, s_k^{12}) \sin\beta. \tag{3.23}$$

Recalling that we set the order parameter to be real and focusing on energies larger than the decay rate,

$$n_{\underline{1}k} + n_{\underline{2}k} - 1 = \frac{4EE_\Delta}{4E^2 + \gamma_* \Delta^2} N_{\mathcal{S}}. \tag{3.24}$$

3.2.4 Superfluid density

The focus of this chapter is on the Meissner effect *i.e.* the response of the system to a non-uniform static electromagnetic vector potential. In this static limit, the electromagnetic

properties are governed by the superfluid density defined through the following relation

$$j^{\mu} = -\rho^{\mu\nu} A^{\nu}. \tag{3.25}$$

We consider the isotropic case, when the superfluid density tensor $\rho^{\mu\nu}$ is reduced to a scalar quantity ρ,

$$\rho^{\mu\nu} = (e^2/d)\rho\, \delta_{\mu\nu}. \tag{3.26}$$

The superfluid density ρ in the present text differs from the standard definition by a factor e^2/d, where d is the spatial dimension, in order to simplify the expressions below.

Similarly to the equilibrium case, there are two contributions to the electric current, paramagnetic and diamagnetic,

$$\rho = \rho_{(\mathrm{para})} + \rho_{(\mathrm{dia})}\,. \tag{3.27}$$

Below we compute these two contributions for generic quasiparticle distributions. In order to do this, we introduce Schwinger-Keldysh formalism in Sec. 3.3, use it to calculate superfluid density in a generic nonequilibrium state with a well-defined quasiparticle distribution function in Sec. 3.4 and then later specialize to the case of photo-induced superconductivity in our specific setup in Sec. 3.5.

3.3 Schwinger-Keldysh formalism

Equilibrium systems have an inherent symmetry between electrons and holes: a hole at a given energy corresponds exactly to an electron undergoing motion back in time at this same energy. Such system can be fully described by considering an electron action

$$\mathcal{S} = \int_{-\infty}^{+\infty} \mathrm{d}t \int \mathrm{d}\boldsymbol{r}\, \bar{\psi} \left[\mathrm{i}\partial_t - \widehat{H} \right] \psi, \tag{3.28}$$

where $\bar{\psi}, \psi$ are electron fields and $\widehat{H}$ is single particle Hamiltonian. For simplicity, in this section we consider a single band system. We then generalize the results for the case of the two-band system.

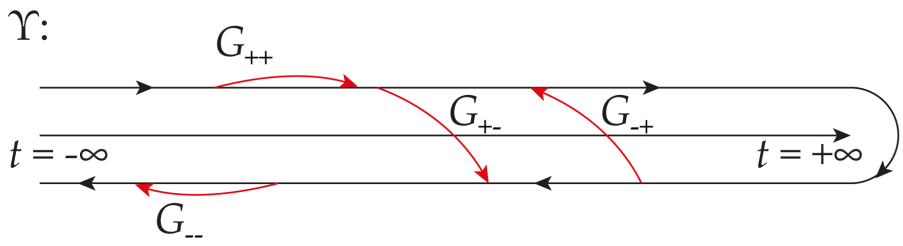

Figure 3.2: *Keldysh integration contour* Y *and four components of the Green's function.*

A process of extracting information from the action (3.28) is not without challenges: derivation of finite temperature correlation functions typically involves Matsubara technique, analytical continuation to and back from imaginary time. In the present chapter we will be dealing with a system that is driven out of thermal equilibrium with external bath. Such explicit time dependence of the Hamiltonian (external driving) adds another layer of complexity to the theoretical description of the quantum system.

As we have stated above, in equilibrium it is enough to describe evolution of electrons and the evolution of holes follows. In a formal language, the evolution of the creation operator $\psi^\dagger$ follows from the evolution of the annihilation operator ψ. In the presence of external drive these two operators have to be described independently. One of the ways to approach the description of such problem, beside a master equation formalism that is especially popular in optical literature, is a Schwinger-Keldysh approach [84, 85, 86]. According to this approach, in order to accommodate the need to describe both ψ and $\psi^\dagger$ simultaneously, we can double the number of variables at each moment of time and consider simultaneously forward and backward evolution in time. This leads to action

$$\mathcal{S}_0 = \int_{\mathrm{Y}} \mathrm{d}t \int \mathrm{d}\boldsymbol{r} \bar{\psi} \left[\mathrm{i}\partial_t - \widehat{H} \right] \psi, \tag{3.29}$$

where the time integral over t goes along the standard Keldysh contour Y going from $-\infty$ to $+\infty$ and then back to $-\infty$. The Keldysh contour is shown on Fig. 3.2. Variables living on the upper branch of the contour going forward in time are labeled with a "+" subscript, while variables on the lower branch are labeled with a "−". Dealing with such unusual time

contour proves to be cumbersome. It is much more convenient to explicitly double the number of variables and have a usual time integration going from $-\infty$ to $+\infty$ one only time:

$$\mathcal{S}_0 = \int_{-\infty}^{+\infty} \mathrm{d}t \int \mathrm{d}\boldsymbol{r} \left[\bar{\psi}_+(t) \left(\mathrm{i}\partial_t - \widehat{H} \right) \psi_+(t) - \bar{\psi}_-(t) \left(\mathrm{i}\partial_t - \widehat{H} \right) \psi_-(t) \right]. \tag{3.30}$$

Such structure leads to four Green's functions instead of just one,

$$G_{\alpha\beta} = -i \left\langle \psi_\alpha \bar{\psi}_\beta \right\rangle, \quad \alpha, \beta = \pm, \tag{3.31}$$

It is customary to perform a so-called Keldysh rotation of the fields living on the two time branches. Electron fields $(\psi^\dagger, \psi)$ transform according to [87]

$$\psi_1 = \frac{\psi_+ + \psi_-}{\sqrt{2}}, \quad \psi_2 = \frac{\psi_+ - \psi_-}{2}, \tag{3.32}$$

while $\bar{\psi}$ is chosen to transform as

$$\bar{\psi}_1 = \frac{\bar{\psi}_+ - \bar{\psi}_-}{\sqrt{2}}, \quad \bar{\psi}_2 = \frac{\bar{\psi}_+ + \bar{\psi}_-}{2}. \tag{3.33}$$

It is important to stress that two fileds $\bar{\psi}, \psi$ are independent of each other and transformation rules (3.33) for $\bar{\psi}$ and ψ are independent and are not related by a simple conjugation.

The structure of the Green's function in the rotated basis is

$$\check{G}_{\alpha\beta} \equiv -i \left\langle \psi_\alpha \bar{\psi}_\beta \right\rangle = \begin{pmatrix} \check{G}^R & \check{G}^K \\ 0 & \check{G}^A \end{pmatrix}_{\alpha\beta}, \tag{3.34}$$

where $G^{R(A)}$ are retarded and advanced Green's functions and Keldysh component can be parametrized as

$$G^K = G^R \circ F - F \circ G^A, \tag{3.35}$$

where "$\circ$" stands for convolution in time and space and F describes the distribution function of electrons. In equilibrium

$$F(\varepsilon) = \tanh \frac{\varepsilon}{2T} \tag{3.36}$$

and

$$G^K(\varepsilon) = F(\varepsilon) \left(G^R(\varepsilon) - G^A(\varepsilon) \right). \tag{3.37}$$

Electromagnetic vector potential is introduced by minimal coupling respecting gauge invariance of the system, replacing momenta $\boldsymbol{p} \to \boldsymbol{p} - e\boldsymbol{A}$. This modifies electron action by modifying electron dispersion as

$$\varepsilon(\boldsymbol{p} - e\boldsymbol{A}) = \varepsilon(\boldsymbol{p}) - e\boldsymbol{v}\cdot\boldsymbol{A} + \frac{e^2}{2}(\widehat{\kappa})_{\alpha\beta}\boldsymbol{A}_\alpha\boldsymbol{A}_\beta. \tag{3.38}$$

where $\widehat{\kappa}$ is a curvature of electron dispersion

$$(\widehat{\kappa})_{\alpha\beta} = \frac{1}{2}\left(\frac{\partial_\alpha \boldsymbol{v}}{\partial \boldsymbol{p}_\beta} + \frac{\partial_\beta \boldsymbol{v}}{\partial \boldsymbol{p}_\alpha}\right). \tag{3.39}$$

Similarly to electron fields, vector potential also lives on both branches of the Keldysh contour having components $\boldsymbol{A}_{+/-}$. We rotate the source of external vector potential introducing *classical* and *quantum* components

$$\boldsymbol{A}_{\mathrm{cl}} = \frac{\boldsymbol{A}_+ + \boldsymbol{A}_-}{2}, \quad \boldsymbol{A}_{\mathrm{q}} = \frac{\boldsymbol{A}_+ - \boldsymbol{A}_-}{2}. \tag{3.40}$$

Such names, *classical* and *quantum*, follow from the fact that a physical real observable external field has to be the same on both branches of the Keldysh contour. Hence its quantum component would be zero.

The total action can be written as

$$\begin{aligned}\mathcal{S}[\boldsymbol{A}] = &\int_{-\infty}^{+\infty} \mathrm{d}t \sum\!\!\!\!\!\!\int_{\alpha,\beta} \mathrm{d}\boldsymbol{p}\bar{\psi}_\alpha \left[G\right]_{\alpha\beta}\psi_\beta + \\ &+ \int_{-\infty}^{+\infty} \mathrm{d}t \sum\!\!\!\!\!\!\int_{\alpha,\beta,\gamma} \mathrm{d}\boldsymbol{p}\bar{\psi}_\alpha \left[e\boldsymbol{v}\cdot\boldsymbol{A}_{(\gamma)} - \frac{e^2}{2}\sum_{\mu,\nu}(\widehat{\kappa})_{\mu\nu}\boldsymbol{A}_{(\gamma),\mu}\boldsymbol{A}_{(\gamma),\nu}\right]\Lambda^\gamma_{\alpha\beta}\psi_\beta,\end{aligned} \tag{3.41}$$

where the Keldysh vertex

$$\Lambda^{\mathrm{cl}} = \begin{pmatrix} 1 & 0 \\ 0 & 1 \end{pmatrix}_{\alpha\beta}, \quad \Lambda^{\mathrm{q}} = \begin{pmatrix} 0 & 1 \\ 1 & 0 \end{pmatrix}_{\alpha\beta}. \tag{3.42}$$

Below we will be dealing only with a physical component and it is implied that $\boldsymbol{A} \equiv \boldsymbol{A}_{\mathrm{cl}}$. The electric current as a physical observable at time t can be obtained as a variation of the

action over the vector potential with $-+$ components [85]

$$\boldsymbol{j} = \left\langle \frac{\delta \mathcal{S}}{\delta A_+} \right\rangle_{\boldsymbol{A}} = e \left\langle \bar{\psi}_- \left[\boldsymbol{v} - e(\widehat{\kappa} \boldsymbol{A}) \right] \psi_+ \right\rangle_{\boldsymbol{A}}, \tag{3.43}$$

where the average should be taken with the action $\mathcal{S}[\boldsymbol{A}]$ that also depends on the vector potential. As we discuss in the previous section, electric current can be decomposed into para- and diamagnetic contributions,

$$\boldsymbol{j} = \boldsymbol{j}_{(\text{para})} + \boldsymbol{j}_{(\text{dia})}. \tag{3.44}$$

that correspond to the two terms in the equation above. We now expand the action in vector potential and keep only linear terms. Once we integrate out electron fields following Eq. (3.34), we find

$$\boldsymbol{j} = -\rho_X \boldsymbol{A}, \quad X = (\text{para})/(\text{dia}), \tag{3.45}$$

with superfluid densities

$$\rho_{(\text{dia})} = -\frac{\mathrm{i}}{2} \sum\!\!\!\!\!\!\int_{\epsilon, \boldsymbol{p}, \mu} (\widehat{\kappa})_{\mu\mu} \left[\check{G}^K - \check{G}^R + \check{G}^A \right] (\epsilon, \boldsymbol{p}), \tag{3.46}$$

and

$$\rho_{(\text{para})} = -\frac{\mathrm{i}}{2} \sum\!\!\!\!\!\!\int_{\epsilon, \boldsymbol{p}, \mu} \left[\check{G}^K \check{v}^\mu \check{G}^R \check{v}^\mu + \check{G}^A \check{v}^\mu \check{G}^K \check{v}^\mu . \right] (\epsilon, \boldsymbol{p}) \tag{3.47}$$

We now proceed with the analysis of the two-band semiconductor.

3.4 Superfluid density

Generalizing results of Sec. 3.3 to the case of a two-band semiconductor, Keldysh action corresponding to the Hamiltonian in Eq. (3.6) reads

$$\mathcal{S} = \int_{\mathrm{Y}} \mathrm{d}t \sum\!\!\!\!\!\!\int_{\boldsymbol{p}} \Psi_{\boldsymbol{p}}^\dagger [\left(\mathrm{i}\partial_t - \varepsilon_{\boldsymbol{p}} \right) \check{I} - E_{\boldsymbol{p}} \check{\tau}^z - \Delta \check{\tau}^x] \Psi_{\boldsymbol{p}}, \tag{3.48}$$

where the time integral over t goes along the standard Keldysh contour. Now Green's function is a 4×4 matrix with a standard Keldysh space structure

$$\check{G}_{\alpha\beta} = \begin{pmatrix} \check{G}^R & \check{G}^K \\ 0 & \check{G}^A \end{pmatrix}_{\alpha\beta}, \tag{3.49}$$

with each component $\underline{\check{G}}^{R(A,K)}$ being also a 2×2 matrix in Nambu-Gor'kov space. For example, the retarded Green's function encodes the spectral properties of the steady-state and reads $\check{G}^R = \check{U}\underline{\check{G}}^R\check{U}^\dagger$ with

$$\underline{\check{G}}^R(\epsilon,\boldsymbol{p})^{-1} = \left(\epsilon - \varepsilon_{\boldsymbol{p}} + \mathrm{i}0\right)\underline{\check{I}} - \xi_{\boldsymbol{p}}\underline{\check{\tau}}^z, \tag{3.50}$$

where the operator $\check{U}$ was defined in Eq. (3.8). A convenient representation is given by

$$\check{G}^R(\epsilon,\boldsymbol{p}) = \frac{1}{\epsilon - \varepsilon_{\boldsymbol{p}} - \xi_{\boldsymbol{p}} + \mathrm{i}0}\check{P}_{+\boldsymbol{p}} + \frac{1}{\epsilon - \varepsilon_{\boldsymbol{p}} + \xi_{\boldsymbol{p}} + \mathrm{i}0}\check{P}_{-\boldsymbol{p}} \tag{3.51}$$

with $\check{P}_\pm$ being the projectors onto the states of the quasiparticle basis, *i.e.* $\underline{\check{P}}_\pm = (\underline{\check{I}} \pm \underline{\check{\tau}}^z)/2$. $\check{G}^A$ can be determined from $\check{G}^R$ by a simple time-reversal operation. The Keldysh Green's function encodes the nonequilibrium state populations by the relation (3.35) extended to the two-band case,

$$\check{G}^K(\epsilon,\boldsymbol{p}) = \left[\check{G}^R\check{F} - \check{F}\check{G}^A\right](\epsilon,\boldsymbol{p}). \tag{3.52}$$

In the case of our model the assumption about well-defined quasiparticle distribution functions expressed with Eq. (3.10) implies that the matrix $\check{F}$ is also diagonal in quasiparticle basis and is given by

$$\underline{\check{F}}(\epsilon,\boldsymbol{p}) = \begin{pmatrix} 1 - 2\underline{n}_{1\boldsymbol{p}} & 0 \\ 0 & 2\underline{n}_{2\boldsymbol{p}} - 1 \end{pmatrix}. \tag{3.53}$$

This means that $\underline{\check{F}}$ commutes with the Green's functions $\underline{\check{G}}^R$ and $\underline{\check{G}}^A$ just as in equilibrium.

In computing superfluid densities in the following subsections, we will need expressions

for "velocity" and "mass" of quasiparticles

$$\check{v}^{\mu}_{\boldsymbol{p}} = V^{\mu}_{\boldsymbol{p}}\check{I} + v^{\mu}_{\boldsymbol{p}}\check{\tau}^{z}, \quad \partial_{\mu}\check{v}^{\nu}_{\boldsymbol{p}} = \partial_{\mu}V^{\nu}_{\boldsymbol{p}}\check{\tau}^{z} + \partial_{\mu}v^{\nu}_{\boldsymbol{p}}\check{I}, \tag{3.54}$$

with $\partial_{\mu} \equiv \partial/\partial p^{\mu}$, $V^{\mu}_{\boldsymbol{p}} \equiv \partial_{\mu}E_{\boldsymbol{p}}$, and $v^{\mu}_{\boldsymbol{p}} \equiv \partial_{\mu}\varepsilon_{\boldsymbol{p}}$. In the quasiparticle basis, they read (omitting the $\boldsymbol{p}$ indices)

$$\begin{aligned} \underline{\check{v}}^{\mu} &= V^{\mu}\underline{\check{I}} + v^{\mu}(\underline{\check{\tau}}^{z}\cos\beta - \underline{\check{\tau}}^{x}\sin\beta)\,, \\ \underline{\partial_{\mu}\check{v}^{\nu}} &= \partial_{\mu}V^{\nu}(\underline{\check{\tau}}^{z}\cos\beta - \underline{\check{\tau}}^{x}\sin\beta) + \partial_{\mu}v^{\nu}\underline{\check{I}}\,. \end{aligned} \tag{3.55}$$

3.4.1 Diamagnetic contribution

We start with the diamagnetic contribution to the superfluid density. Generalizing Eq. (3.46), we have

$$\rho_{(\mathrm{dia})} = -\frac{\mathrm{i}}{2}\sum\!\!\!\!\!\!\int_{\epsilon,\boldsymbol{p},\mu} \mathrm{Tr}\left[\partial_{\mu}\check{v}_{\mu}\left[\check{G}^{K} - \check{G}^{R} + \check{G}^{A}\right](\epsilon,\boldsymbol{p})\right], \tag{3.56}$$

where the trace runs in Nambu-Gor'kov space. The equation (3.56) has contributions from both quasiparticle bands. The contribution from the upper quasiparticle band can be computed using equations (3.50), (3.55), and (3.10), yielding

$$\sum\!\!\!\!\!\!\int_{\boldsymbol{p},\mu}\left(\partial_{\mu}V^{\mu}\cos\beta + \partial_{\mu}v^{\mu}\right)\underline{n}_{1\boldsymbol{p}}, \tag{3.57}$$

since the actual occupation number [85] is given by

$$\underline{n}_{1\boldsymbol{p}} = -\frac{\mathrm{i}}{2}\int_{\epsilon}\left[\underline{\check{G}}^{K}_{11} - \underline{\check{G}}^{R}_{11} + \underline{\check{G}}^{A}_{11}\right](\epsilon,\boldsymbol{p}). \tag{3.58}$$

The second quasiparticle band contributes with

$$\sum\!\!\!\!\!\!\int_{\boldsymbol{p},\mu}\left(-\partial_{\mu}V^{\mu}\cos\beta_{\boldsymbol{p}} + \partial_{\mu}v^{\mu}\right)(1 - \underline{n}_{2\boldsymbol{p}})\,, \tag{3.59}$$

such that, at last, we obtain

$$\rho_{(\mathrm{dia})} = \sum\!\!\!\!\!\!\int_{\boldsymbol{p},\mu}(\partial_{\mu}V^{\mu}\cos\beta_{\boldsymbol{p}}\,(\underline{n}_{1\boldsymbol{p}} + \underline{n}_{2\boldsymbol{p}} - 1) + (\partial_{\mu}v^{\mu})(\underline{n}_{1\boldsymbol{p}} - \underline{n}_{2\boldsymbol{p}} + 1)\,. \tag{3.60}$$

3.4.2 Paramagnetic contribution

The paramagnetic contribution to the superfluid density is given by (see Eq. 3.47)

$$\rho_{(\text{para})} = -\frac{\mathrm{i}}{2} \sum\!\!\!\!\!\!\int_{\epsilon,\boldsymbol{p},\mu} \mathrm{Tr}\left[\check{G}^K \check{v}^\mu \check{G}^R \check{v}^\mu + \check{G}^A \check{v}^\mu \check{G}^K \check{v}^\mu\right]. \tag{3.61}$$

Given that we focus on the Meissner effect, we have to be careful with the order of limits $\omega, \boldsymbol{q} \to 0$ for the external vector potential $\boldsymbol{A}$. The Meissner effect corresponds to expulsion of the static magnetic field, so in order to get the superfluid density we have to take the $\omega \to 0$ limit first. To show the importance of the order of limits we retain $\omega, \boldsymbol{q}$ explicitly:

$$\rho_{(\text{para})}(\omega, \boldsymbol{q}) = -\frac{\mathrm{i}}{2} \sum\!\!\!\!\!\!\int_{\epsilon,\boldsymbol{p},\mu} \mathrm{Tr}\left[\check{G}^K_+ \check{v}^\mu \check{G}^R_- \check{v}^\mu + \check{G}^A_+ \check{v}^\mu \check{G}^K_- \check{v}^\mu\right], \tag{3.62}$$

where $\pm$ correspond to arguments $\epsilon \pm \omega/2$, $\boldsymbol{p} \pm \boldsymbol{q}/2$.

We separate the total Green's function bubble into intra- and interband parts based on whether the quasiparticles change bands within the Green's function bubble,

$$\rho_{(\text{para})}(\omega, \boldsymbol{q}) = \rho^{(\text{intra})}_{(\text{para})}(\omega, \boldsymbol{q}) + \rho^{(\text{inter})}_{(\text{para})}(\omega, \boldsymbol{q}). \tag{3.63}$$

Intraband contribution

The intraband contribution can be further broken down into contributions of the two quasiparticle bands,

$$\rho^{(\text{intra})}_{(\text{para})}(\omega, \boldsymbol{q}) = \rho^{(\text{intra-1})}_{(\text{para})}(\omega, \boldsymbol{q}) + \rho^{(\text{intra-2})}_{(\text{para})}(\omega, \boldsymbol{q}), \tag{3.64}$$

where the contribution of the first quasiparticle band is

$$\rho^{(\text{intra-1})}_{(\text{para})}(\omega, \boldsymbol{q}) = -\frac{\mathrm{i}}{2} \sum\!\!\!\!\!\!\int_{\epsilon,\boldsymbol{p},\mu} (\underline{\check{v}}^\mu_{11})^2 \left(\underline{G}^K_{11+}\underline{G}^R_{11-} + \underline{G}^A_{11+}\underline{G}^K_{11-}\right), \tag{3.65}$$

The first term of (3.65) is

$$\begin{aligned}\sum\!\!\!\!\!\!\int_{\epsilon,\boldsymbol{p},\mu}(\check{v}^{\mu}_{\underline{11}})^2 G^K_{1+}G^R_{1-} &= \sum\!\!\!\!\!\!\int_{\epsilon,\boldsymbol{p},\mu}(\check{v}^{\mu}_{\underline{11}})^2 F_{11+}\left(G^R_{1+}-G^A_{1+}\right)G^R_{1-}\\ &= -2\mathrm{i}\pi\sum\!\!\!\!\!\!\int_{\epsilon,\boldsymbol{p},\mu}(\check{v}^{\mu}_{\underline{11}})^2 F_{11+}\delta(\epsilon_+-(\varepsilon+\xi)_+)\frac{1}{\epsilon_--(\varepsilon+\xi)_-+\mathrm{i}0}\\ &= -\mathrm{i}\sum\!\!\!\!\!\!\int_{\boldsymbol{p},\mu}(\check{v}^{\mu}_{\underline{11}})^2\frac{F_{11+}}{(\varepsilon+\xi)_+-(\varepsilon+\xi)_--\omega+\mathrm{i}0},\end{aligned} \tag{3.66}$$

where we took into account the fact that the Green's function combination $\left(G^R-G^A\right)$ is related to density of states and

$$\begin{aligned}G^R_{1+}-G^A_{1+} =&\frac{1}{\epsilon_+-(\varepsilon+\xi)_++\mathrm{i}0}-\frac{1}{\epsilon_+-(\varepsilon+\xi)_+-\mathrm{i}0}\\ =&-2\mathrm{i}\pi\delta(\epsilon_+-(\varepsilon+\xi)_+),\end{aligned} \tag{3.67}$$

with δ being Dirac delta function.

Similarly, the second term turns out to be

$$\sum\!\!\!\!\!\!\int_{\epsilon,\boldsymbol{p},\mu}(\check{v}^{\mu}_{\underline{11}})^2 G^A_{1+}G^K_{1-} = -\mathrm{i}\sum\!\!\!\!\!\!\int_{\epsilon,\boldsymbol{p},\mu}(\check{v}^{\mu}_{\underline{11}})^2\frac{-F_{11-}}{(\varepsilon+\xi)_+-(\varepsilon+\xi)_--\omega+\mathrm{i}0}, \tag{3.68}$$

so that the total contribution of the first band into intraband part is

$$\rho^{(\text{intra-1})}_{(\text{para})}(\omega,\boldsymbol{q}) = -\frac{1}{2}\sum\!\!\!\!\!\!\int_{\epsilon,\boldsymbol{p},\mu}(\check{v}^{\mu}_{11}\check{v}^{\mu}_{11})\frac{F_{11+}-F_{11-}}{(\varepsilon+\xi)_+-(\varepsilon+\xi)_--\omega+\mathrm{i}0}. \tag{3.69}$$

To proceed we note that the matrix element F_{11} gives the quasiparticle distribution function

$$F_{11}(\varepsilon,\boldsymbol{p}) = 1-2\underline{n}_{1\boldsymbol{p}}, \tag{3.70}$$

the matrix element of the velocity operator is

$$\check{v}^{\mu}_{11} = V^{\mu}+v^{\mu}\cos\beta, \tag{3.71}$$

and taking the limit yields

$$\rho^{(\text{intra-1})}_{(\text{para})} = \sum\!\!\!\!\!\!\int_{\boldsymbol{p},\mu}(V^{\mu}_{\boldsymbol{p}}+v^{\mu}_{\boldsymbol{p}}\cos\beta_{1\boldsymbol{p}})^2\underline{n}'_{1\boldsymbol{p}}, \tag{3.72}$$

where we introduced the quantity

$$\begin{aligned}\underline{n}'_{1(2)\boldsymbol{p}} &= -\frac{1}{2}\lim_{\boldsymbol{q}\to 0}\lim_{\omega\to 0}\frac{F_{11(22)+}-F_{11(22)-}}{(\varepsilon+\xi)_+-(\varepsilon+\xi)_- -\omega+\mathrm{i}0}\\ &\equiv \lim_{\boldsymbol{q}\to 0}\frac{\underline{n}_{1(2)\boldsymbol{p}+\boldsymbol{q}}-\underline{n}_{1(2)\boldsymbol{p}}}{(\varepsilon_{\boldsymbol{p}+\boldsymbol{q}}\pm\xi_{\boldsymbol{p}+\boldsymbol{q}})-(\varepsilon_{\boldsymbol{p}}\pm\xi_{\boldsymbol{p}})} = \frac{\partial_p \underline{n}_{1(2)p}}{v^{\mathrm{qp}}_{1(2)p}}\end{aligned} \tag{3.73}$$

and in the last step we assumed isotropic dispersion relations and v^{qp}_{α} is the quasiparticle velocity ($\alpha = 1,2$). This quantity can be interpreted as a derivative of the quasiparticle distribution function over energy. In particular, it reduces to the usual energy derivative in the equilibrium.

Similarly, the contribution of the second band is

$$\rho^{(\text{intra-2})}_{(\text{para})} = \sum\!\!\!\!\!\!\int_{\boldsymbol{p},\mu}(V^{\mu}_{\boldsymbol{p}}-v^{\mu}_{\boldsymbol{p}}\cos\beta_{\boldsymbol{p}})^2\underline{n}'_{2\boldsymbol{p}}. \tag{3.74}$$

Summation of the two gives

$$\rho^{\text{intra}}_{(\text{para})} = \sum\!\!\!\!\!\!\int_{\boldsymbol{p},\mu}(V^{\mu}_{\boldsymbol{p}}+v^{\mu}_{\boldsymbol{p}}\cos\beta_{\boldsymbol{p}})^2\underline{n}'_{1\boldsymbol{p}}+(V^{\mu}_{\boldsymbol{p}}-v^{\mu}_{\boldsymbol{p}}\cos\beta_{\boldsymbol{p}})^2\underline{n}'_{2\boldsymbol{p}},. \tag{3.75}$$

The order of limits in $\omega, \boldsymbol{q}\to 0$ was crucial throughout the calculation. With the opposite order of limits we would have a zero intraband contribution

$$\lim_{\omega\to 0}\lim_{\boldsymbol{q}\to 0}\frac{\underline{n}_{1(\boldsymbol{p}+\boldsymbol{q}/2)}-\underline{n}_{1(\boldsymbol{p}-\boldsymbol{q}/2)}}{(\varepsilon+\xi)_{\boldsymbol{p}+\boldsymbol{q}/2}-(\varepsilon+\xi)_{\boldsymbol{p}}-\boldsymbol{q}/2-\omega+\mathrm{i}0} = \lim_{\omega\to 0}\frac{0}{-\omega+\mathrm{i}0} = 0. \tag{3.76}$$

Finally, we note that strictly speaking the vertex coupling electrons to the vector potential is

$$\frac{1}{2}\left(\check{v}^{\mu}_{\boldsymbol{p}+\boldsymbol{q}/2}+\check{v}^{\mu}_{\boldsymbol{p}-\boldsymbol{q}/2}\right) = \check{v}^{\mu}_{\boldsymbol{p}}+O(q^2), \tag{3.77}$$

but the corrections coming from finite external vector potential momentum $\boldsymbol{q}$ are irrelevant for the present calculation.

Interband contribution

In contrast, the order of limits is irrelevant for the interband contribution due to the presence of the superconducting gap. In the intraband contribution we compare energies of the two

quasiparticles from the same band and the quantity $(\varepsilon+\xi)_+ - (\varepsilon+\xi)_- \to 0$ in the denominator results in the importance of the order of limits. Meanwhile, in the interband contribution below we will be comparing two quasiparticles from different bands encountering a well-defined denominator $(\varepsilon+\xi)_+ - (\varepsilon-\xi)_- \to 2\xi \geq 2\Delta$. Thus we omit external frequency ω and momentum $\boldsymbol{q}$ right away.

The contribution of interband processes is

$$\rho^{(\text{inter})}_{(\text{para})} = -\frac{\mathrm{i}}{2} \oint\!\!\!\!\!\!\sum_{\epsilon,\boldsymbol{p},\mu} (\check{v}^{\mu}_{12}\check{v}^{\mu}_{21}) \left(\underline{G}^{K}_{11}\underline{G}^{R}_{22} + \underline{G}^{A}_{11}\underline{G}^{K}_{22} + \underline{G}^{K}_{22}\underline{G}^{R}_{11} + \underline{G}^{A}_{22}\underline{G}^{K}_{11}\right). \tag{3.78}$$

This expression can be conveniently represented as

$$\rho^{(\text{inter})}_{(\text{para})} = \operatorname{Im} \oint\!\!\!\!\!\!\sum_{\epsilon,\boldsymbol{p},\mu} (\check{v}^{\mu}_{12}\check{v}^{\mu}_{21}) \left(\underline{G}^{K}_{11}\underline{G}^{R}_{22} + \underline{G}^{K}_{22}\underline{G}^{R}_{11}\right). \tag{3.79}$$

The first term in the equation above gives

$$\begin{aligned} \oint\!\!\!\!\!\!\sum_{\epsilon,\boldsymbol{p},\mu} (\check{v}^{\mu}_{12}\check{v}^{\mu}_{21})\underline{G}^{K}_{11}\underline{G}^{R}_{22} &= \oint\!\!\!\!\!\!\sum_{\epsilon,\boldsymbol{p},\mu} (\check{v}^{\mu}_{12}\check{v}^{\mu}_{21}) F_{11}\left(\underline{G}^{R}_{11} - \underline{G}^{A}_{11}\right)\underline{G}^{R}_{22} \\ &= -2\mathrm{i}\pi \oint\!\!\!\!\!\!\sum_{\epsilon,\boldsymbol{p},\mu} (\check{v}^{\mu}_{12}\check{v}^{\mu}_{21}) F_{11}\delta(\epsilon - (\varepsilon+\xi)) \frac{1}{\epsilon - (\varepsilon-\xi) + \mathrm{i}0} \\ &= -\mathrm{i} \oint\!\!\!\!\!\!\sum_{\boldsymbol{p},\mu} (\check{v}^{\mu}_{12}\check{v}^{\mu}_{21}) \frac{F_{11}}{2\xi}. \end{aligned} \tag{3.80}$$

Similarly, the second term is

$$\oint\!\!\!\!\!\!\sum_{\epsilon,\boldsymbol{p},\mu} (\check{v}^{\mu}_{12}\check{v}^{\mu}_{21})\underline{G}^{K}_{22}\underline{G}^{R}_{11} = -\mathrm{i} \oint\!\!\!\!\!\!\sum_{\boldsymbol{p},\mu} (\check{v}^{\mu}_{12}\check{v}^{\mu}_{21}) \frac{F_{22}}{-2\xi}. \tag{3.81}$$

Taking into account that the diagonal elements of the quasiparticle distribution function are

$$F_{11}(\varepsilon,\boldsymbol{p}) = 1 - 2\underline{n}_{1\boldsymbol{p}}, \quad F_{22}(\varepsilon,\boldsymbol{p}) = 2\underline{n}_{2\boldsymbol{p}} - 1, \tag{3.82}$$

and the matrix elements of the velocity operator are

$$\check{v}^{\mu}_{12} = \check{v}^{\mu}_{21} = -v^{\mu}\sin\beta, \tag{3.83}$$

we get

$$\rho^{(\text{inter})}_{(\text{para})} = -\sum\!\!\!\!\!\!\int_{p,\mu} (v^\mu \sin\beta)^2 \frac{F_{11}-F_{22}}{2\xi} = \int_{p,\mu} v_p^2 \sin^2\beta_p \frac{\underline{n}_{1p}+\underline{n}_{2p}-1}{\xi_p}. \tag{3.84}$$

3.4.3 Total superfluid density

Integrating by parts the diamagnetic contribution (3.60) and summing with both paramagnetic terms (3.75,3.84), we obtain the final result for the net superfluid density of the system (see appendix C.1 for detailed steps):

$$\rho = -\int_p (V_p^2 - v_p^2)\sin^2\beta_p \left[\frac{\underline{n}_{1p}+\underline{n}_{2p}-1}{\xi_p} - \underline{n}'_{1p} - \underline{n}'_{2p}\right]. \tag{3.85}$$

The equation above is the central result of this chapter. It is applicable to a wide class of electronic dispersions as long as the superconducting state is stable and with a diagonal quasiparticle distribution function. The immediate application of interest is to use this result to study the superfluid density of a photo-induced inter-band superconductor, which is the topic of the next section.

3.5 Superfluid density in the steady state

In the optical-pumping setup a nonequilibrium population of the two electron bands is created by shining a laser on the system. The laser is responsible for the emergence of a resonance surface in momentum space, $\mathcal{S}$, where the sum of the two bands $2E_{\boldsymbol{k}} = E_{1\boldsymbol{k}} + E_{2\boldsymbol{k}} = 0$. The resonant surface $\mathcal{S}$ has essentially the same role as a Fermi surface in a conventional BCS superconductor in thermal equilibrium. Superconducting pairing takes place around the resonant surface $\mathcal{S}$, where $E_{\boldsymbol{k}} = 0$. For simplicity, we assume that $\mathcal{S}$ is rotationally invariant. The electronic dispersions can be expanded in the vicinity of this surface as

$$E_k \equiv \frac{E_{1k}+E_{2k}}{2} \simeq V(k-k_{\mathcal{S}}) + \kappa_+(k-k_{\mathcal{S}})^2, \tag{3.86}$$

$$\varepsilon_k \equiv \frac{E_{1k}-E_{2k}}{2} \simeq \varepsilon_0 + v(k-k_{\mathcal{S}}) + \kappa_-(k-k_{\mathcal{S}})^2. \tag{3.87}$$

Superconductivity	✓	✓	✓	✓
$V_{\rm int}$	-	-	+	+
$N_{\mathcal{S}}$	-	+	-	+
$\kappa_+ = \frac{\kappa_1+\kappa_2}{2}$	+	-	-	+
ρ	-	-	+	+

Table 3.1: *Sign of the superfluid density ρ for different parameters: electronic interaction $V_{\rm int}$ (repulsive when positive), nonequilibrium population imbalance $N_{\mathcal{S}}$ [see Eq. (3.91)] and average band curvature κ_+. Only the cases allowing for an inter-band superconducting state are displayed.*

A situation which is especially favorable for the formation of the superconducting order corresponds to whenever the velocity matching condition $V = 0$ is satisfied, see Ref. [83] for details. Below, we concentrate on this case, such that $E_k \simeq \kappa_+(k - k_{\mathcal{S}})^2$.

As it follows from Eqs. (3.19, 3.20), the distribution functions in Eq. (3.85) are relatively smooth around the resonant surface and depend only on the energy E_k. Together with the assumed velocity matching condition, $V \simeq 0$, this implies that the second term in the superfluid density in Eq. (3.85) is negligible as compared to the first one, since the quasiparticle velocities $v_{\underline{1}(\underline{2})p} = v_p \pm V_p \cos\beta_p \simeq v$ and

$$\underline{n}'_{\alpha p} \equiv \frac{\partial_k \underline{n}_{\alpha k}}{v^{\rm qp}_{\alpha k}} \simeq \frac{d\underline{n}_\alpha(E)}{dE}\left(\frac{V}{v}\right) \underset{V/v\to 0}{\longrightarrow} 0. \tag{3.88}$$

Simplifying, we get

$$\rho \simeq \int_{\boldsymbol{p}} v^2 \frac{\Delta^2}{\xi_p^3}(\underline{n}_{1p} + \underline{n}_{2p} - 1)\,, \tag{3.89}$$

where, we recall, $\xi_{\boldsymbol{p}} \equiv \sqrt{E_{\boldsymbol{p}}^2 + \Delta^2}$.

Now, we make use of the explicit form of distribution functions (3.19, 3.20). In particular, a relevant quantity of interest is

$$\underline{n}_{1\boldsymbol{k}} + \underline{n}_{2\boldsymbol{k}} - 1 = \frac{4E_k\sqrt{E_k^2+\Delta^2}}{4E_k^2 + \gamma_*\Delta^2} N_{\mathcal{S}}\,, \tag{3.90}$$

where we introduced the combination

$$N_{\mathcal{S}} \equiv n_{\mathrm{F}}(E_{1\boldsymbol{k}}, \mu_1) + n_{\mathrm{F}}(E_{2\boldsymbol{k}}, \mu_2) - 1\,, \tag{3.91}$$

with $n_{\mathrm{F}}(E_{\alpha\boldsymbol{k}}, \mu_\alpha)$ the Fermi-Dirac distributions corresponding to the quasi-thermal equilibrium that sets up in each band. The effective chemical potentials μ_α can be seen as Lagrange multipliers enforcing the average number of particles in each band, and depend on the balance between the optical drive and the interband relaxation mechanisms [83]. Note that the finiteness of the above quantity, $N_{\mathcal{S}} \neq 0$, is crucial to the formation of an interband Cooper pairing. For convenience we introduced $\gamma_* \equiv \Gamma_{12}(\Gamma_1^{-1} + \Gamma_2^{-1})$ with $\Gamma_{1,2}$ being intraband relaxation rates. We obtain the superfluid density

$$\rho \simeq N_{\mathcal{S}}\, v^2 \int_{\boldsymbol{k}} \frac{4\Delta^2 E_{\boldsymbol{k}}}{(E_{\boldsymbol{k}}^2 + \Delta^2)(4E_{\boldsymbol{k}}^2 + \gamma_*\Delta^2)}\,, \tag{3.92}$$

and the self-consistency equation for photo-induced superconductivity

$$1 = 2N_{\mathcal{S}}\, V_{\mathrm{int}} \int_{\boldsymbol{k}} \frac{E_{\boldsymbol{k}}}{4E_{\boldsymbol{k}}^2 + \gamma_*\Delta^2}\,. \tag{3.93}$$

The most pressing questions are now

- Is superconductivity possible?
- What is the sign of the superfluid density?

Answers to these question depend solely on the signs of three parameters, namely: electron-electron interaction V_{int}, curvature of the electron dispersion κ_+, and $N_{\mathcal{S}}$. Indeed, a rapid inspection of the right-hand side of Eq. (3.92) implies that the sign of the superfluid density is governed by

$$\mathrm{sgn}(\rho) = \mathrm{sgn}(\kappa_+) \times \mathrm{sgn}(N_{\mathcal{S}})\,. \tag{3.94}$$

Similarly, the inspection of the right-hand side of Eq. (3.93) implies that a solution with a finite superconducting order parameter exists whenever

$$\mathrm{sgn}(V_{\mathrm{int}}) = \mathrm{sgn}(\kappa_+) \times \mathrm{sgn}(N_{\mathcal{S}})\,. \tag{3.95}$$

The corresponding outcomes for different cases are summarized in the Table 3.1. We now compute the expression of the superfluid density in two limiting cases: $\Delta \gg \Gamma$ and $\Delta \ll \Gamma$.

In the regime $\Delta \gg \Gamma$, we start by expanding the energy E_k around the resonance surface (using the velocity matching condition, $V \simeq 0$), $E \simeq \kappa_+(k - k_S)^2$, so that the superfluid density becomes

$$\rho = (\operatorname{sgn}\kappa_+ N_S)\frac{A_S v^2}{\sqrt{\Delta\,|\kappa_+|}} B_\rho\left(\gamma_*\right), \tag{3.96}$$

where $A_S = 4\pi k_S^2$ is the area of the resonant surface ($2\pi k_S$ for a two-dimensional system) and $B_\rho(x)$ is a positive function

$$B_\rho(x) = \int_{-\infty}^{\infty} \mathrm{d}t \frac{4t^2}{(t^4+1)(4t^4+x)} = \begin{cases} \pi x^{-1/4} & x \ll 1 \\ 2\sqrt{2}\pi x^{-1} & x \gg 1 \end{cases}. \tag{3.97}$$

Equation (3.96) displays an anomalous scaling of the superfluid density ρ with the order parameter Δ,

$$\rho \propto \frac{1}{\sqrt{\Delta}} \text{ for } \Delta \gg \Gamma\,. \tag{3.98}$$

Such a divergent scaling survives only while $\Delta \gg \Gamma$. In the regime where $\Delta \ll \Gamma$, after re-including properly the factors of Γ that have been neglected so far (see the appendix C.2 for a detailed derivation), one finds

$$\rho \propto \Delta^2 \text{ for } \Delta \ll \Gamma\,, \tag{3.99}$$

which is similar to the conventional BCS scenario in equilibrium. The two scalings in Eqs. (3.98) and (3.99) signal that the superfluid density reaches a maximum in the crossover regime.

3.6 Conclusion

We have computed the superfluid density of the superconducting state that can be induced by optically pumping valence band electrons to the conduction band. We found a positive

superfluid density in the presence of repulsive electronic interactions, and this constitutes an important check of the stability of the superconducting order announced in Ref. [83]. The next check is to make sure that the heating caused by the optical pumping is slow enough to allow for the superconducting order to develop (on the order of hundreds on $1/\Gamma$'s) and, perhaps more importantly, for the transport measurements to be performed. The power dissipated can estimated to be $\mathcal{P} \sim \Gamma_{\text{Interband}} \times N \times \hbar\omega_{\text{gap}}$ with an interband recombination rate $\Gamma_{\text{Interband}} \sim 10^{-8}$ eV, a density of states $N \sim 10^{20}/\text{cm}^3$, and $\hbar\omega_{\text{gap}} \sim 0.3$ eV, amounting to $\mathcal{P} \sim 10^{6-7}$ J/s.cm^3, and leading to a generous window of 10^{-4} s to perform the experiments before the sample temperature increases by approximately 10 K (in the absence of external cooling).

References

[1] Chris B Stringer and Peter Andrews. Genetic and fossil evidence for the origin of modern humans. *Science*, 239(4845):1263–1268, 1988.

[2] Xiaohong Wu, Chi Zhang, Paul Goldberg, David Cohen, Yan Pan, Trina Arpin, and Ofer Bar-Yosef. Early pottery at 20,000 years ago in xianrendong cave, china. *Science*, 336(6089):1696–1700, 2012.

[3] Amanda G Henry, Alison S Brooks, and Dolores R Piperno. Microfossils in calculus demonstrate consumption of plants and cooked foods in neanderthal diets (shanidar iii, iraq; spy i and ii, belgium). *Proceedings of the National Academy of Sciences*, 108(2):486–491, 2011.

[4] James Thomson. A quantitative investigation of certain relations between the gaseous, the liquid, and the solid states of water-substance. *Proceedings of the Royal Society of London*, 22(148-155):27–36, 1874.

[5] Stephen Carr, Daniel Massatt, Shiang Fang, Paul Cazeaux, Mitchell Luskin, and Efthimios Kaxiras. Twistronics: Manipulating the electronic properties of two-dimensional layered structures through their twist angle. *Physical Review B*, 95(7):075420, 2017.

[6] Yuan Cao, Valla Fatemi, Shiang Fang, Kenji Watanabe, Takashi Taniguchi, Efthimios Kaxiras, and Pablo Jarillo-Herrero. Unconventional superconductivity in magic-angle graphene superlattices. *Nature*, 556(7699):43, 2018.

[7] Jason R Petta. Atom-by-atom construction of a quantum device. *ACS nano*, 11(3):2382–2386, 2017.

[8] André Eckardt. Colloquium: Atomic quantum gases in periodically driven optical lattices. *Rev. Mod. Phys.*, 89:011004, Mar 2017.

[9] Wen-Yu He, Dong-Hui Xu, Benjamin T. Zhou, Qi Zhou, and K. T. Law. From nodal-ring topological superfluids to spiral majorana modes in cold atomic systems. *Phys. Rev. A*, 97:043618, Apr 2018.

[10] Nobuo Furukawa, T. M. Rice, and Manfred Salmhofer. Truncation of a two-dimensional fermi surface due to quasiparticle gap formation at the saddle points. *Phys. Rev. Lett.*, 81:3195–3198, Oct 1998.

[11] Igor Dzyaloshinskii. Extended van-hove singularity and related non-fermi liquids. *J. Phys. I France*, 6(1):119–135, 1996.

[12] D. M. Newns, H. R. Krishnamurthy, P. C. Pattnaik, C. C. Tsuei, and C. L. Kane. Saddle-point pairing: An electronic mechanism for superconductivity. *Phys. Rev. Lett.*, 69:1264–1267, Aug 1992.

[13] A. Ziletti, S. M. Huang, D. F. Coker, and H. Lin. Van hove singularity and ferromagnetic instability in phosphorene. *Phys. Rev. B*, 92:085423, Aug 2015.

[14] González, J., Guinea, F., and Vozmediano, M. A. H. Renormalization group analysis of electrons near a van hove singularity. *Europhys. Lett.*, 34(9):711–716, 1996.

[15] S. Gopalan, O. Gunnarsson, and O. K. Andersen. Effects of saddle-point singularities on the electron lifetime. *Phys. Rev. B*, 46:11798–11806, Nov 1992.

[16] D. Menashe and B. Laikhtman. Fermi-liquid properties of a two-dimensional electron system with the fermi level near a van hove singularity. *Phys. Rev. B*, 59:13592–13595, Jun 1999.

[17] V. Yu. Irkhin, A. A. Katanin, and M. I. Katsnelson. Effects of van hove singularities on magnetism and superconductivity in the $t - t'$ hubbard model: A parquet approach. *Phys. Rev. B*, 64:165107, Oct 2001.

[18] Anton Kapustin, Tristan McKinney, and Ira Z. Rothstein. Effective Field Theory of 2D van Hove Singularities. 2016.

[19] Rahul Nandkishore, L. S. Levitov, and A. V. Chubukov. Chiral superconductivity from repulsive interactions in doped graphene. *Nature Physics*, 8(2):158–163, FEB 2012.

[20] Sedigh Ghamari, Sung-Sik Lee, and Catherine Kallin. Renormalization group analysis of a neck-narrowing lifshitz transition in the presence of weak short-range interactions in two dimensions. *Phys. Rev. B*, 92:085112, Aug 2015.

[21] R. M. Hornreich, Marshall Luban, and S. Shtrikman. Critical behavior at the onset of $\vec{k}$-space instability on the λ line. *Phys. Rev. Lett.*, 35:1678–1681, Dec 1975.

[22] Amnon Aharony, Eytan Domany, R. M. Hornreich, T. Schneider, and M. Zannetti. Novel lifshitz tricritical point and critical dynamics. *Phys. Rev. B*, 32:3358–3360, Sep 1985.

[23] M. Thede, A. Mannig, M. Månsson, D. Hüvonen, R. Khasanov, E. Morenzoni, and A. Zheludev. Pressure-induced quantum critical and multicritical points in a frustrated spin liquid. *Phys. Rev. Lett.*, 112:087204, Feb 2014.

[24] Rudro R. Biswas, Liang Fu, Chris R. Laumann, and Subir Sachdev. Su(2)-invariant spin liquids on the triangular lattice with spinful majorana excitations. *Phys. Rev. B*, 83:245131, Jun 2011.

[25] Mikito Koshino. Electronic transport in bilayer graphene. *New Journal of Physics*, 11(9):095010, 2009.

[26] Anastasia Varlet, Dominik Bischoff, Pauline Simonet, Kenji Watanabe, Takashi Taniguchi, Thomas Ihn, Klaus Ensslin, Marcin Mucha-Kruczyński, and Vladimir I. Fal'ko. Anomalous sequence of quantum hall liquids revealing a tunable lifshitz transition in bilayer graphene. *Phys. Rev. Lett.*, 113:116602, Sep 2014.

[27] Vladimir I. Arnold. *Catastrophe Theory*. Springer-Verlag, 1992.

[28] AA Abrikosov, LP Gor'kov, and IE Dzyaloshinskii. *Methods of Quantum Field Theory in Statistical Physics*. Prentice-Hall, Englewood Cliffs, NJ, 1963.

[29] S Engels, B Terrés, A Epping, T Khodkov, K Watanabe, T Taniguchi, B Beschoten, and C Stampfer. Limitations to carrier mobility and phase-coherent transport in bilayer graphene. *Physical review letters*, 113(12):126801, 2014.

[30] R. Shankar. Renormalization-group approach to interacting fermions. *Rev. Mod. Phys.*, 66:129–192, Jan 1994.

[31] Subir Sachdev. *Quantum Phase Transitions*. Cambridge University Press, second edition, 2011.

[32] Lederer, P., Montambaux, G., and Poilblanc, D. Antiferromagnetism and superconductivity in a quasi two-dimensional electron gas. scaling theory of a generic hubbard model. *J. Phys. France*, 48(10):1613–1618, 1987.

[33] C Lester, Silvia Ramos, RS Perry, TP Croft, RI Bewley, T Guidi, P Manuel, DD Khalyavin, EM Forgan, and SM Hayden. Field-tunable spin-density-wave phases in sr 3 ru 2 o 7. *Nature materials*, 14(4):373, 2015.

[34] AW Rost, RS Perry, J-F Mercure, AP Mackenzie, and SA Grigera. Entropy landscape of phase formation associated with quantum criticality in sr3ru2o7. *Science*, 325(5946):1360–1363, 2009.

[35] Christoph M Puetter, Jeffrey G Rau, and Hae-Young Kee. Microscopic route to nematicity in sr 3 ru 2 o 7. *Physical Review B*, 81(8):081105, 2010.

[36] D. Efremov. Unpublished.

[37] K. v. Klitzing, G. Dorda, and M. Pepper. New method for high-accuracy determination of the fine-structure constant based on quantized Hall resistance. *Phys. Rev. Lett.*, 45:494–497, Aug 1980.

[38] D. J. Thouless, M. Kohmoto, M. P. Nightingale, and M. den Nijs. Quantized Hall conductance in a two-dimensional periodic potential. *Phys. Rev. Lett.*, 49:405–408, Aug 1982.

[39] C. L. Kane and E. J. Mele. Quantum spin Hall effect in graphene. *Phys. Rev. Lett.*, 95:226801, Nov 2005.

[40] C. L. Kane and E. J. Mele. $\mathbb{Z}_2$ topological order and the quantum spin Hall effect. *Phys. Rev. Lett.*, 95:146802, Sep 2005.

[41] Liang Fu and C. L. Kane. Time reversal polarization and a $\mathbb{Z}_2$ adiabatic spin pump. *Phys. Rev. B*, 74:195312, Nov 2006.

[42] B. Andrei Bernevig and Shou-Cheng Zhang. Quantum spin Hall effect. *Phys. Rev. Lett.*, 96:106802, Mar 2006.

[43] B. Andrei Bernevig, Taylor L. Hughes, and Shou-Cheng Zhang. Quantum spin Hall effect and topological phase transition in HgTe quantum wells. *Science*, 314(5806):1757–1761, 2006.

[44] Markus König, Steffen Wiedmann, Christoph Brüne, Andreas Roth, Hartmut Buhmann, Laurens W. Molenkamp, Xiao-Liang Qi, and Shou-Cheng Zhang. Quantum spin Hall insulator state in HgTe quantum wells. *Science*, 318(5851):766–770, 2007.

[45] Liang Fu, C. L. Kane, and E. J. Mele. Topological insulators in three dimensions. *Phys. Rev. Lett.*, 98:106803, Mar 2007.

[46] J. E. Moore and L. Balents. Topological invariants of time-reversal-invariant band structures. *Phys. Rev. B*, 75:121306, Mar 2007.

[47] Rahul Roy. $\mathbb{Z}_2$ classification of quantum spin Hall systems: An approach using time-reversal invariance. *Phys. Rev. B*, 79:195321, May 2009.

[48] Rahul Roy. Topological phases and the quantum spin Hall effect in three dimensions. *Phys. Rev. B*, 79:195322, May 2009.

[49] D. Hsieh, D. Qian, L. Wray, Y. Xia, Y. S. Hor, R. J. Cava, and M. Z. Hasan. A topological Dirac insulator in a quantum spin Hall phase. *Nature*, 452(7190):970–974, Apr 2008.

[50] D. Hsieh, Y. Xia, L. Wray, D. Qian, A. Pal, J. H. Dil, J. Osterwalder, F. Meier, G. Bihlmayer, C. L. Kane, Y. S. Hor, R. J. Cava, and M. Z. Hasan. Observation of unconventional quantum spin textures in topological insulators. *Science*, 323(5916):919–922, 2009.

[51] D. Hsieh, Y. Xia, D. Qian, L. Wray, J. H. Dil, F. Meier, J. Osterwalder, L. Patthey, J. G. Checkelsky, N. P. Ong, A. V. Fedorov, H. Lin, D. Bansil, A. eand Grauer, Y. S. Hor, R. J. Cava, and M. Z. Hasan. A tunable topological insulator in the spin helical Dirac transport regime. *Nature*, 460(7259):1101–1105, Aug 2009.

[52] Y. L. Chen, J. G. Analytis, J.-H. Chu, Z. K. Liu, S.-K. Mo, X. L. Qi, H. J. Zhang, D. H. Lu, X. Dai, Z. Fang, S. C. Zhang, I. R. Fisher, Z. Hussain, and Z.-X. Shen. Experimental realization of a three-dimensional topological insulator, Bi_2Te_3. *Science*, 325(5937):178–181, 2009.

[53] M. Z. Hasan and C. L. Kane. Colloquium: Topological insulators. *Rev. Mod. Phys.*, 82:3045–3067, Nov 2010.

[54] Xiao-Liang Qi and Shou-Cheng Zhang. Topological insulators and superconductors. *Rev. Mod. Phys.*, 83:1057–1110, Oct 2011.

[55] A. A. Burkov, M. D. Hook, and Leon Balents. Topological nodal semimetals. *Phys. Rev. B*, 84:235126, Dec 2011.

[56] A. A. Burkov and Leon Balents. Weyl semimetal in a topological insulator multilayer. *Phys. Rev. Lett.*, 107:127205, Sep 2011.

[57] Xiangang Wan, Ari M. Turner, Ashvin Vishwanath, and Sergey Y. Savrasov. Topological semimetal and Fermi-arc surface states in the electronic structure of pyrochlore iridates. *Phys. Rev. B*, 83:205101, May 2011.

[58] Madhab Neupane, Su-Yang Xu, Raman Sankar, Nasser Alidoust, Guang Bian, Chang Liu, Ilya Belopolski, Tay-Rong Chang, Horng-Tay Jeng, Hsin Lin, Arun Bansil, Fangcheng Chou, and M. Zahid Hasan. Observation of a three-dimensional topological Dirac semimetal phase in high-mobility Cd_3As_2. *Nature Communications*, 5:3786 EP –, May 2014. Article.

[59] Z. K. Liu, B. Zhou, Y. Zhang, Z. J. Wang, H. M. Weng, D. Prabhakaran, S.-K. Mo, Z. X. Shen, Z. Fang, X. Dai, Z. Hussain, and Y. L. Chen. Discovery of a three-dimensional topological Dirac semimetal, Na_3Bi. *Science*, 343(6173):864–867, 2014.

[60] Shin-Ming Huang, Su-Yang Xu, Ilya Belopolski, Chi-Cheng Lee, Guoqing Chang, BaoKai Wang, Nasser Alidoust, Guang Bian, Madhab Neupane, Chenglong Zhang, Shuang Jia, Arun Bansil, Hsin Lin, and M. Zahid Hasan. A Weyl Fermion semimetal with surface Fermi arcs in the transition metal monopnictide TaAs class. *Nature Communications*, 6:7373 EP –, Jun 2015. Article.

[61] B. Q. Lv, H. M. Weng, B. B. Fu, X. P. Wang, H. Miao, J. Ma, P. Richard, X. C. Huang, L. X. Zhao, G. F. Chen, Z. Fang, X. Dai, T. Qian, and H. Ding. Experimental discovery of Weyl semimetal TaAs. *Phys. Rev. X*, 5:031013, Jul 2015.

[62] Rui Yu, Hongming Weng, Zhong Fang, Xi Dai, and Xiao Hu. Topological node-line semimetal and Dirac semimetal state in antiperovskite Cu_3PdN. *Phys. Rev. Lett.*, 115:036807, Jul 2015.

[63] Tomáš Bzdušek, QuanSheng Wu, Andreas Ruegg, Manfred Sigrist, and Alexey A. Soluyanov. Nodal-chain metals. *Nature*, 538(7623):75–78, OCT 6 2016.

[64] Andreas P. Schnyder, Shinsei Ryu, Akira Furusaki, and Andreas W. W. Ludwig. Classification of topological insulators and superconductors in three spatial dimensions. *Phys. Rev. B*, 78:195125, Nov 2008.

[65] P. Vogl, Harold P. Hjalmarson, and John D. Dow. A semi-empirical tight-binding theory of the electronic structure of semiconductors. *Journal of Physics and Chemistry of Solids*, 44(5):365 – 378, 1983.

[66] J.C. Slater. *Symmetry and Energy Bands in Crystals*. Dover Publications, 1965.

[67] New Semiconductor Materials archive: Physical Properties of Semiconductors (Si). `http://www.ioffe.ru/SVA/NSM/Semicond/Si/bandstr.html`.

[68] Qinghui Yan, Rongjuan Liu, Zhongbo Yan, Boyuan Liu, Hongsheng Chen, Zhong Wang, and Ling Lu. Experimental discovery of nodal chains. *Nature Physics*, page 1, 2018.

[69] Marcos Atala, Monika Aidelsburger, Julio T Barreiro, Dmitry Abanin, Takuya Kitagawa, Eugene Demler, and Immanuel Bloch. Direct measurement of the zak phase in topological bloch bands. *Nature Physics*, 9(12):795, 2013.

[70] Jun-Won Rhim, Jan Behrends, and Jens H Bardarson. Bulk-boundary correspondence from the intercellular zak phase. *Physical Review B*, 95(3):035421, 2017.

[71] Guido van Miert, Carmine Ortix, and Cristiane Morais Smith. Topological origin of edge states in two-dimensional inversion-symmetric insulators and semimetals. *2D Materials*, 4(1):015023, 2016.

[72] Ivan I Naumov and Russell J Hemley. Topological surface states in dense solid hydrogen. *Physical Review Letters*, 117(20):206403, 2016.

[73] Vladimir N. Strocov, Ming Shi, Masaki Kobayashi, Claude Monney, Xiaoqiang Wang, Juraj Krempasky, Thorsten Schmitt, Luc Patthey, Helmuth Berger, and Peter Blaha. Three-dimensional electron realm in vse_2 by soft-x-ray photoelectron spectroscopy: Origin of charge-density waves. *Phys. Rev. Lett.*, 109:086401, Aug 2012.

[74] S. Kaiser, C. R. Hunt, D. Nicoletti, W. Hu, I. Gierz, H. Y. Liu, M. Le Tacon, T. Loew, D. Haug, B. Keimer, and A. Cavalleri. Optically induced coherent transport far above T_c in underdoped $yba_2cu_3o_{6+\delta}$. *Phys. Rev. B*, 89:184516, May 2014.

[75] Roman Mankowsky, Michael FÃ¶rst, and Andrea Cavalleri. Non-equilibrium control of complex solids by nonlinear phononics. *Reports on Progress in Physics*, 79(6):064503, 2016.

[76] L. P. Gor'kov and G. M. Eliashberg. Superconducting Alloys in a Rapidly Alternating Magnetic Field of Large Amplitude. *JETP Lett*, 8:202, September 1968.

[77] G. M. Eliashberg. Film superconductivity stimulated by a high-frequency field. *JETP Lett.*, 11:114, 1970.

[78] V. M. Dmitriev, E. V. Khristenko, A. V. Trubitsyn, and F. F. Mende. Behaviour of superconductive thin-film bridges in hhf fields. *Ukr. Fiz. Zh.*, 15(10):1614, 1970.

[79] VM Galitskii, VF Elesin, and Yu V Kopaev. Feasibility of high-temperature superconductivity in nonequilibrium systems with repulsion. *JETP Lett*, 18:27, 1973.

[80] DA Kirzhnits and Yu V Kopaev. Superconductivity in non-equilibrium with repulsion between particles. *JETP Lett*, 17:270, 1973.

[81] VF Elesin, Yu V Kopaev, and R Kh Timerov. Theory of superconductivity in systems with an inverse distribution. *JETP Lett*, 38:1170, 1974.

[82] V M Galitskii, V F Elesin, and Yu V Kopaev. The kinetic theory of superconductors with excess quasiparticles. In Donald N Langenberg and Anthony Ignatius Larkin, editors, *Nonequilibrium Superconductivity*, pages 377–451. Elsevier Science Publishers, 1986.

[83] Garry Goldstein, Camille Aron, and Claudio Chamon. Photoinduced superconductivity in semiconductors. *Phys. Rev. B*, 91:054517, Feb 2015.

[84] Leonid V Keldysh. Diagram technique for nonequilibrium processes. *Sov. Phys. JETP*, 20(4):1018–1026, 1965.

[85] J. Rammer and H. Smith. Quantum field-theoretical methods in transport theory of metals. *Rev. Mod. Phys.*, 58:323–359, Apr 1986.

[86] A. Kamenev and A. Levchenko. Keldysh technique and non-linear σ-model: basic principles and applications. *Advances in Physics*, 58(3):197–319, 2009.

[87] A. I. Larkin and Yu. N Ovchinnikov. Vortex motion in superconductors. In D. N. Langenberg and A. I. Larkin, editors, *Nonequilibrium Superconductivity*, page 493. Elsevier, 1986.

Appendix A

Appendix to Chapter 1

A.1 DOS in the vicinity of the multicritical point in $Sr_3Ru_2O_7$

As we discuss in the main text, the physics of the multicritical Lifshitz point can be described by the dispersion

$$\varepsilon(\boldsymbol{p}) = ap^2 + bp^4 \cos 4\varphi + cp^8 - \mu. \tag{A.1}$$

Below we assume small values of a and μ. In this case the p^8 term is not crucial for the analysis, as it only serves to close the Fermi surface away from the singularity, and it can be omitted safely,

$$\varepsilon(\boldsymbol{p}) \simeq ap^2 + bp^4 \cos 4\varphi - \mu. \tag{A.2}$$

For definiteness we assume $a > 0$ below. The symmetry of the dispersion (A.2) implies relation $\nu(-|a|, \mu) = \nu(|a|, -\mu)$.

The DoS of A.2 is given by

$$\nu(\mu) = \int \frac{d^2p}{(2\pi)^2}\delta(ap^2 + bp^4\cos 4\varphi - \mu) = \int \frac{d\varphi dt}{8\pi^2}\delta(at + bt^2\cos 4\varphi - \mu) = \frac{1}{4\pi^2 a} D\left(\frac{4b\mu}{a^2}\right), \tag{A.3}$$

where we made a substitution $t = p^2$ and the function $D(x)$ is an elliptic integral

$$D(x) = \int_0^{2\pi} d\varphi \int_0^{\infty} dt\, \delta(2t + t^2\cos\varphi - x) = 2\,\mathrm{Re}\int_0^{\infty} dt \frac{1}{\sqrt{t^4 - (2t - x)^2}}. \tag{A.4}$$

The DoS obtained above has a natural energy scale

$$\mu_c = a^2/4b. \tag{A.5}$$

A.1.1 Critical scaling at $|\mu| \gg \mu_c$

The term ap^2 breaks the multicriticality, so that at large values of the chemical potential $|\mu| \gg a^2/4b$, when quadratic term can be neglected, the dispersion reduces to the pure fourth-order saddle

$$\varepsilon(\boldsymbol{p}) = bp^4 \cos 4\varphi - \mu \tag{A.6}$$

with the critical scaling of the DoS $\nu(\mu) \propto |\mu|^{-1/2}$,

$$\nu(\mu) = \int \frac{d^2p}{(2\pi)^2}\delta(bp^4\cos 4\varphi - \mu) = \frac{1}{4\pi^2\sqrt{b\,|\mu|}}\int d^2k\,\delta(k^4\cos 4\varphi - 1) = \frac{K(1/2)}{4\sqrt{2}\pi^2}\frac{1}{\sqrt{b\,|\mu|}} \propto |\mu|^{-1/2}, \tag{A.7}$$

where $K(1/\sqrt{2}) \approx 1.85$ is a complete elliptic integral of the first kind.

A.1.2 Jump at $\mu = 0$

As we approach the singularity from the region of negative chemical potential, the quadratic term leads to the formation of electron pocket at the center. The electron pocket forms at $\mu = 0$ and leads to a jump in the density of states,

$$\begin{aligned}\nu(\mu = +0) - \nu(\mu = -0) &= \lim_{\mu\to+0}\int \frac{d^2p}{(2\pi)^2}\delta(ap^2 + bp^4\cos 4\varphi - \mu) - \lim_{\mu\to-0}\int \frac{d^2p}{(2\pi)^2}\delta(ap^2 + bp^4\cos 4\varphi - \mu) \\ &= \lim_{\mu\to+0}\int \frac{d^2p}{(2\pi)^2}\delta(ap^2 - \mu) = \frac{1}{4\pi a}.\end{aligned} \tag{A.8}$$

A.1.3 Van Hove singularity at $\mu = \mu_c$

Finally, at the value of the chemical potential $\mu = \mu_c = a^2/4b$ the electron pocket formed at $\mu = 0$ touches four outer leaves of the Fermi surface via the formation of four saddle points,

located at $p_c = \sqrt{a/2b}$, $\cos 4\varphi_c = -1$:

$$\begin{aligned} ap^2 + bp^4 \cos 4\varphi - \mu &\approx a(p_c + \Delta p)^2 - b(p_c + \Delta p)^4 \left(1 - \frac{(4\Delta\varphi)^2}{2}\right) - \mu \\ &= (ap_c^2 - bp_c^4 - \mu) + (2ap_c - 4bp_c^3)\Delta p + (a - 6bp_c^2)(\Delta p)^2 + 8bp_c^4(\Delta\varphi)^2 \\ &= (\mu - \mu_c) - 2a(\Delta p)^2 + 8\mu_c(\Delta\varphi)^2. \end{aligned} \tag{A.9}$$

The saddle point result in the logarithmic divergence in the DoS:

$$\begin{aligned} \nu(\mu) &= 4\int \frac{d^2p}{(2\pi)^2}\delta((\mu - \mu_c) - 2a(\Delta p)^2 + 8\mu_c(\Delta\varphi)^2) \\ &= \frac{1}{2\sqrt{2}\pi^2 a}\int dxdy\,\delta\left(\frac{\mu - \mu_c}{\mu_c} - x^2 + y^2\right) \\ &\simeq \frac{1}{\sqrt{2}\pi^2 a}\log\frac{\mu_c}{|\mu - \mu_c|}. \end{aligned} \tag{A.10}$$

These results can be confirmed by studying limits of the general expression (A.3).

A.1.4 General expression

Using a substitution $z = (t - x)/t$ the elliptic integral $D(x)$ can be rewritten as

$$D(x) = 2\,\mathrm{Re}\int_{-\mathrm{sgn}\,x}^{\infty} \frac{dz}{\sqrt{[(|x| - 1) + z^2][(|x| + 1) - z^2]}}. \tag{A.11}$$

Taking the real part of the integral above just reduces the integration to the region where the argument of the square root is positive. Depending on the value of x, the true domain of integration is

$$\begin{aligned} x > 1: &\quad z \in (-1, \sqrt{1 + |x|}), \\ 0 < x < 1: &\quad z \in (-1, -\sqrt{1 - |x|}) \cup (\sqrt{1 - |x|}, \sqrt{1 + |x|}), \\ x < 0: &\quad z \in (1, \sqrt{1 + |x|}). \end{aligned} \tag{A.12}$$

Transforming the variable as $z = \sqrt{(|x| + 1)}\cos\theta$ we bring the integral to the canonical

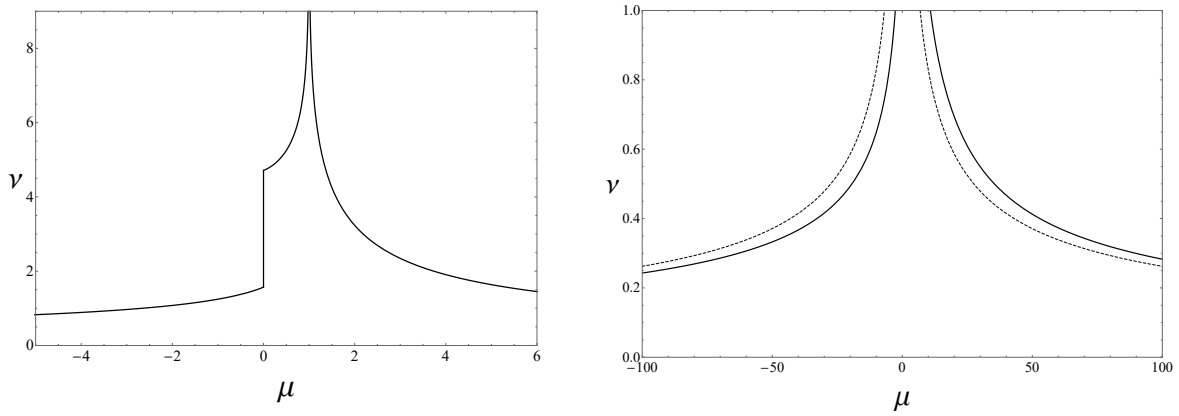

Figure A.1: *DoS $\nu(\mu) \equiv D(\mu)$, with DoS and chemical potential in units $(4\pi^2 a)^{-1}$ and $\mu_c = a^2/4b$ respectively. The plot on the right shows DoS at larger values of the chemical potential when the singularity breaking term ap^2 can be neglected. The dashed line shows the critical scaling of the density of states given by (A.15), $\nu(\mu) \propto |\mu|^{-1/2}$.*

form

$$D(x) = \sqrt{\frac{2}{|x|}} \times \begin{cases} F(\pi - \varphi_1(x), k(x)), & x > 1 \\ 2F(\varphi_2(x), k(x)) - F(\varphi_1(x), k(x)) & 0 < x < 1 \\ F(\varphi_1(x), k(x)), & x < 0 \end{cases} \tag{A.13}$$

where modulus and angles are

$$k(x) = \sqrt{\frac{1+|x|}{2|x|}}, \quad \varphi_1 = \arctan(\sqrt{|x|}), \quad \varphi_2 = \arctan\sqrt{\frac{2|x|}{1-|x|}}. \tag{A.14}$$

At large values of the argument the asymptotic behavior is

$$D(x) \simeq \sqrt{\frac{2}{|x|}} K\left(\frac{1}{\sqrt{2}}\right), \quad |x| \gg 1, \tag{A.15}$$

Appendix B

Appendix to Chapter 2

B.1 Spinor structure and Berry fluxes in the graphene and silicon lattices

Let us first apply the formalism presented in the main text to derive the familiar result that in graphene there is a π-vortex in the Brillouin zone at the K point. The carbon atoms form a honeycomb lattice, with interpenetrating triangular sublattices A and B. The A sites sit on lattice sites spanned by the basis vectors $\mathbf{R}_1 = \sqrt{3}\,a\,(1/2, \sqrt{3}/2)$ and $\mathbf{R}_2 = \sqrt{3}\,a\,(-1/2, \sqrt{3}/2)$, where $a = 1.42$Å. The reciprocal lattice vectors are $\mathbf{G}_1 = \frac{4\pi}{3a}\,(\sqrt{3}/2, 1/2)$ and $\mathbf{G}_2 = \frac{4\pi}{3a}\,(-\sqrt{3}/2, 1/2)$. The three vectors connecting sublattice A to B are $\mathbf{d}_0 = a\,(0,1)$, $\mathbf{d}_1 = a\,(-\sqrt{3}/2, -1/2)$, and $\mathbf{d}_2 = a\,(\sqrt{3}/2, -1/2)$.

The off-diagonal hopping matrix element for the π-orbital is

$$H_{AB}(\mathbf{k}) = -\sum_{\mu=0}^{2} t(\mathbf{d}_\mu)\, e^{i\mathbf{k}\cdot\mathbf{d}_\mu}\,, \tag{B.1}$$

where we allowed generically for unequal values for the hoppings to the three nearest neighbors. The vectors $\mathbf{G}_{1,2}$ and $\mathbf{d}_{0,1,2}$ satisfy

$$\mathbf{G}_i \cdot \mathbf{d}_\mu = \frac{2\pi}{3} \pmod{2\pi} \quad \text{for } i = 1,2 \text{ and } \mu = 0,1,2\,. \tag{B.2}$$

It then follows that the 2×2 Hamiltonian for graphene is not periodic in $\mathbf{k}$, but instead

is periodic up to the gauge transformation in Eq. (2.3) of the main text (repeated here for convenience):

$$H(\mathbf{k}+\mathbf{G}_i) = U(\mathbf{G}_i)\, H(\mathbf{k})\, U^\dagger(\mathbf{G}_i)\,, \quad \text{with} \quad U(\mathbf{G}_i) = e^{\,\mathrm{i}\frac{1}{2}\Phi(\mathbf{G}_i)\,\sigma_z}\,, \tag{B.3}$$

with $\Phi(\mathbf{G}_i) = 2\pi/3$. One can also check that $-(\mathbf{G}_1+\mathbf{G}_2)\cdot\mathbf{d}_\mu = \frac{2\pi}{3} \pmod{2\pi}$, for $\mu = 0,1,2$, or equivalently, $\Phi(-\mathbf{G}_1-\mathbf{G}_2) = 2\pi/3$.

We then consider the walk in $\mathbf{k}$-space that visits, in order, the points $\mathbf{k}, \mathbf{k}+\mathbf{G}_1, \mathbf{k}+\mathbf{G}_1+\mathbf{G}_2$ and back to $\mathbf{k}$. This walk visits three neighboring Brillouin zones, returning to the original point in $\mathbf{k}$-space, closing a loop, shown in Fig. B.1. We know that, in graphene, this loop will not visit a degeneracy point if we choose $\mathbf{k} = 0$ (the Γ point). (In silicon, we shift the point $\mathbf{k}$ from the origin to avoid going through degeneracies.) At the end of the walk, the Hamiltonian returns to $H(\mathbf{k})$, but the eigenvector is rotated by the sequence of unitary operations

$$\begin{aligned} U(-\mathbf{G}_1-\mathbf{G}_2)\, U(\mathbf{G}_2)\, U(\mathbf{G}_1) &= e^{\,\mathrm{i}\frac{1}{2}[\Phi(-\mathbf{G}_1-\mathbf{G}_2)+\Phi(\mathbf{G}_2)+\Phi(\mathbf{G}_1)]\,\sigma_z} \\ &= e^{\,\mathrm{i}\pi\,\sigma_z} = -\mathbb{I}\,. \end{aligned} \tag{B.4}$$

This rotation changes the sign of the wavefunction, which is equivalent to an accumulation of a Berry phase of π. Indeed, the Dirac node at the K point contains the π-vortex when all the three hoppings to the nearest neighbors are equal. If these three hoppings are not equal, the vortex moves location in $\mathbf{k}$-space, but cannot disappear; it must be contained within the triangle. To disappear, the vortex must come to the boundaries of the triangle to meet an anti-vortex, but when that happens our assumption that the path does not include a degenerate point no longer applies.

Having completed the warm up exercise of recovering know results for graphene in two spatial dimensions, we apply the same steps for silicon in three dimensions. In silicon the A sites sit on lattice sites spanned by the basis vectors $\mathbf{R}_1 = \frac{a}{2}(0,1,1)$, $\mathbf{R}_2 = \frac{a}{2}(1,0,1)$, and $\mathbf{R}_3 = \frac{a}{2}(1,1,0)$, with $a = 5.4310$Å. The reciprocal lattice vectors are $\mathbf{G}_1 = \frac{2\pi}{a}(-1,1,1)$, $\mathbf{G}_2 = \frac{2\pi}{a}(1,-1,1)$, and $\mathbf{G}_3 = \frac{2\pi}{a}(1,1,-1)$. The four vectors connecting sublattice A to B are $\mathbf{d}_0 = \frac{a}{4}(1,1,1)$, $\mathbf{d}_1 = \frac{a}{4}(1,-1,-1)$, $\mathbf{d}_2 = \frac{a}{4}(-1,1,-1)$, and $\mathbf{d}_3 = \frac{a}{4}(-1,-1,1)$.

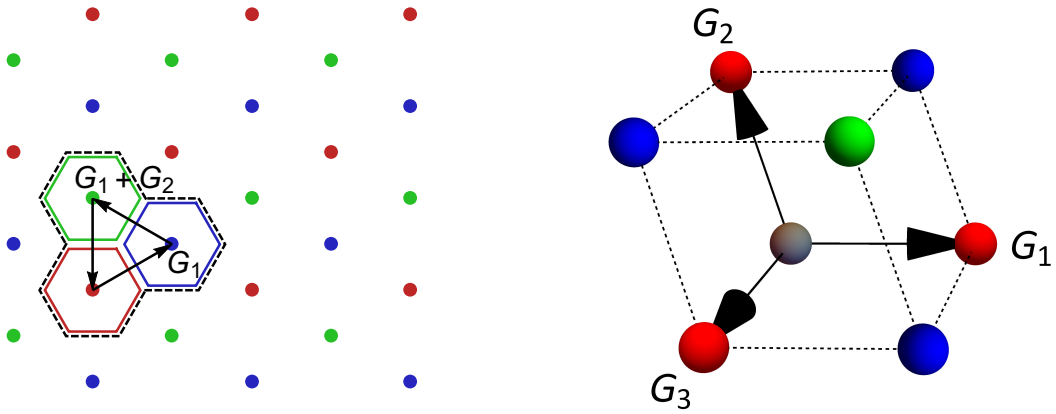

Figure B.1: Reciprocal lattice. *Left: reciprocal lattice of graphene. There are three possible axial phases at the center of the Brillouin zone, $0, 2\pi/3, 4\pi/3$, which are represented by three colors. This leads to tripling of the Brillouin zone, as shown by the dashed line emclosing three hexagons of different colors. The figure also shows a loop constructed out of* **G** *vectors with an overall π Berry phase that establishes existence of the Dirac points at the K/K′ points.*
Right: reciprocal lattice of silicon. In the case of silicon there are four possible axial phases and hence four colors for the reciprocal lattice sites, indicating the quadrupling of the Brillouin zone.

The off-diagonal block matrix, whose dimension depends on how many orbitals we consider, is given by Eq. (2.2) of the main text with the index $\mu = 0, 1, 2, 4$:

$$[H_{AB}(\mathbf{k})]_{\alpha\beta} = -\sum_{\mu=0}^{4} t_{\alpha\beta}(\mathbf{d}_\mu)\, e^{i\mathbf{k}\cdot\mathbf{d}_\mu}\,, \tag{B.5}$$

where again we allowed generically for unequal values for the hoppings to the three nearest neighbors. The vectors $\mathbf{G}_{1,2,3}$ and $\mathbf{d}_{0,1,2,3}$ satisfy

$$\mathbf{G}_i \cdot \mathbf{d}_\mu = \frac{2\pi}{4} \pmod{2\pi} \quad \text{for } i = 1, 2, 3 \text{ and } \mu = 0, 1, 2, 4\,. \tag{B.6}$$

The Hamiltonian for silicon is therefore not periodic in $\mathbf{k}$, but instead is periodic up to the gauge transformation in Eq. (2.3) of the main text [repeated in Eq. (B.3) for convenience], with $\Phi(\mathbf{G}_i) = 2\pi/4$. One can also check that $-(\mathbf{G}_1 + \mathbf{G}_2 + \mathbf{G}_3)\cdot\mathbf{d}_\mu = \frac{2\pi}{4} \pmod{2\pi}$, for $\mu = 0, 1, 2, 3$, or equivalently, $\Phi(-\mathbf{G}_1 - \mathbf{G}_2 - \mathbf{G}_3) = 2\pi/4$.

We then consider the walk in $\mathbf{k}$-space that was described in the main text, one that visits, in order, the points $\mathbf{k}, \mathbf{k}+\mathbf{G}_1, \mathbf{k}+\mathbf{G}_1+\mathbf{G}_2, \mathbf{k}+\mathbf{G}_1+\mathbf{G}_2+\mathbf{G}_3$ and back to $\mathbf{k}$. As explained in the main text, we start at a $\mathbf{k}$ near but not at the Γ point, to avoid passing through lines of

degeneracy. At the end of the walk, the Hamiltonian returns to $H(\mathbf{k})$, but the eigenvector is rotated by the sequence of unitary operations

$$\begin{aligned} & U(-\mathbf{G}_1 - \mathbf{G}_2 - \mathbf{G}_3)\, U(\mathbf{G}_3)\, U(\mathbf{G}_2)\, U(\mathbf{G}_1) = \\ & = e^{\,\mathrm{i}\frac{1}{2}[\Phi(-\mathbf{G}_1-\mathbf{G}_2-\mathbf{G}_3)+\Phi(\mathbf{G}_3)+\Phi(\mathbf{G}_2)+\Phi(\mathbf{G}_1)]\,\sigma_z} \\ & = e^{\,\mathrm{i}\pi\,\sigma_z} = -\mathbb{I}\,. \end{aligned} \tag{B.7}$$

The wavefunction changes sign upon returning from the walk, which requires that a π-flux lines pierce the region enclosed by the walk. The flux lines required by the argument above are precisely those described in the main text, obtained via direct calculation of the Berry curvature in the sp^3s^* model.

Appendix C

Appendix to Chapter 3

C.1 Total superfluid density

Here we reproduce the result (3.85) for the total superfluid density from the main text. While the summation of the dia- and paramagnetic contributions is a mathematical exercise, it is not entirely straightforward and we illustrate it here for the convenience of the reader. To reproduce the compact expression from the main text, we have to integrate by parts the diamagnetic contribution

$$\rho_{(\mathrm{dia})} = \sum\!\!\!\!\!\!\int_{\boldsymbol{p},\mu} (\partial_\mu V^\mu_{\boldsymbol{p}} \cos\beta_{\boldsymbol{p}} \, (\underline{n}_{1\boldsymbol{p}} + \underline{n}_{2\boldsymbol{p}} - 1) + (\partial_\mu v^\mu_{\boldsymbol{p}})(\underline{n}_{1\boldsymbol{p}} - \underline{n}_{2\boldsymbol{p}} + 1)\,. \tag{C.1}$$

Integrating by parts we have

$$\begin{aligned} \rho_{(\mathrm{dia})} = -\sum\!\!\!\!\!\!\int_{\boldsymbol{p},\mu} (V^\mu_{\boldsymbol{p}} \partial_\mu(\cos\beta_{\boldsymbol{p}}) \, (\underline{n}_{1\boldsymbol{p}} + \underline{n}_{2\boldsymbol{p}} - 1) + \\ + V^\mu_{\boldsymbol{p}} \cos\beta_{\boldsymbol{p}} \, \partial_\mu(\underline{n}_{1\boldsymbol{p}} + \underline{n}_{2\boldsymbol{p}}) + \\ + v^\mu_{\boldsymbol{p}} \partial_\mu(\underline{n}_{1\boldsymbol{p}} - \underline{n}_{2\boldsymbol{p}})\,. \end{aligned} \tag{C.2}$$

Let us label the contribution in each line above as $\rho^{(\alpha)}_{(\mathrm{dia})}$, $\alpha = 1, 2, 3$.

First, since $\cos\beta_{\boldsymbol{p}} = E/\sqrt{E^2_{\boldsymbol{p}} + \Delta^2}$, we have

$$\partial_\mu(\cos\beta_{\boldsymbol{p}}) = \frac{\Delta^2}{(E^2_{\boldsymbol{p}} + \Delta^2)^{3/2}} V^\mu_{\boldsymbol{p}} = \frac{V^\mu_{\boldsymbol{p}}}{\xi_{\boldsymbol{p}}} \sin^2\beta_{\boldsymbol{p}} \tag{C.3}$$

and the first contribution becomes

$$\rho^{(1)}_{(\mathrm{dia})} = -\int_{p,\mu} V_p^2 \sin^2\beta_p \frac{\underline{n}_{1p} + \underline{n}_{2p} - 1}{\xi_p}. \tag{C.4}$$

Second, we go back to the definition of the derivative of the distribution function over the quasiparticle energy (3.73) and observe that since

$$\underline{n}'_{1(2)p} \equiv \lim_{q\to 0} \frac{\underline{n}_{1(2)p+q} - \underline{n}_{1(2)p}}{(\varepsilon_{p+q} \pm \xi_{p+q}) - (\varepsilon_p \pm \xi_p)}, \tag{C.5}$$

then

$$\partial_\mu \underline{n}_{1(2)p} = \underline{n}'_{1(2)p}(v^\mu_p \pm \partial^\mu \xi_p) = \underline{n}'_{1(2)p}(v^\mu_p \pm V^\mu_p \cos\beta_p). \tag{C.6}$$

Using this identity, we have

$$\rho^{(2)}_{(\mathrm{dia})} = -\int_{p,\mu} V^\mu_p \cos\beta_p \left(\underline{n}'_{1p}(v^\mu_p + V^\mu_p \cos\beta_p) + \underline{n}'_{2p}(v^\mu_p - V^\mu_p \cos\beta_p)\right) \tag{C.7}$$

and

$$\rho^{(3)}_{(\mathrm{dia})} = -\int_{p,\mu} v^\mu_p \left(\underline{n}'_{1p}(v^\mu_p + V^\mu_p \cos\beta_p) - -\underline{n}'_{2p}(v^\mu_p - V^\mu_p \cos\beta_p)\right), \tag{C.8}$$

Adding together $\rho_{(\mathrm{dia}-2)}$, $\rho_{(\mathrm{dia}-3)}$ and $\rho^{\mathrm{intra}}_{(\mathrm{para})}$ (given by Eq.(3.75)), we have

$$\begin{aligned}
&\rho^{(2)}_{(\mathrm{dia})} + \rho^{(3)}_{(\mathrm{dia})} + \rho^{\mathrm{intra}}_{(\mathrm{para})} = \\
&= -\int_{p,\mu} \Big[\underline{n}'_{1p}\left(v_p^2 + 2v^\mu_p V^\mu_p \cos\beta_p + V_p^2\cos^2\beta_p + -(V^\mu_p + v^\mu_p \cos\beta_{1p})^2\right) + \\
&+\underline{n}'_{2p}\left(v_p^2 - 2v^\mu_p V^\mu_p \cos\beta_p + V_p^2\cos^2\beta_p - -(V^\mu_p - v^\mu_p \cos\beta_{1p})^2\right)\Big].
\end{aligned} \tag{C.9}$$

After simplification the expression becomes

$$\rho^{(2)}_{(\mathrm{dia})} + \rho^{(3)}_{(\mathrm{dia})} + \rho^{\mathrm{intra}}_{(\mathrm{para})} = \int_{p,\mu} (V_p^2 - v_p^2)\sin^2\beta_p \left(\underline{n}'_{1p} + \underline{n}'_{2p}\right). \tag{C.10}$$

The remaining piece $\rho_{(\mathrm{dia}-1)}$ can be combined with the interband paramagnetic contribution $\rho^{(\mathrm{inter})}_{(\mathrm{para})}$

$$\rho^{(1)}_{(\mathrm{dia})} + \rho^{(\mathrm{inter})}_{(\mathrm{para})} = -\int_{p,\mu} (V_p^2 - v_p^2)\sin^2\beta_p \frac{\underline{n}_{1p} + \underline{n}_{2p} - 1}{\xi_p}. \tag{C.11}$$

It is clear now that we indeed obtain the total superfluid density from the main text:

$$\begin{aligned}\rho = \rho_{(\text{para})} + \rho_{(\text{dia})} &= \left(\rho^{(2)}_{(\text{dia})} + \rho^{(3)}_{(\text{dia})} + \rho^{\text{intra}}_{(\text{para})}\right) + \left(\rho^{(1)}_{(\text{dia})} + \rho^{(\text{inter})}_{(\text{para})}\right) \\ &= -\int_p (V_p^2 - v_p^2)\sin^2\beta_p \left[\frac{\underline{n}_{1p} + \underline{n}_{2p} - 1}{\xi_p} - \underline{n}'_{1p} - \underline{n}'_{2p}\right].\end{aligned} \tag{C.12}$$

C.2 Finite Γ effects on superfluid density

Here we analyze more closely the superfluid density in the vicinity of the superconducting transition. In order to explore the region $\Delta \ll \Gamma$ we would like to phenomenologically include the effects of finite dissipation Γ. Therefore we write:

$$\rho \cong N_S v^2 \int_k \frac{4\Delta^2 E_k}{\left(E_k^2 + \Gamma^2/4 + \Delta^2\right)\left(4E_k^2 + \Gamma^2 + \gamma_*\Delta^2\right)} \tag{C.13}$$

Furthermore the self consistency equation becomes

$$1 = 2N_S V_{\text{int}} \int_k \frac{E_k}{\left(4E_k^2 + \Gamma^2 + \gamma_*\Delta^2\right)}, \tag{C.14}$$

which after the integration gives

$$1 = \frac{\pi V_{\text{int}} N_S}{2\sqrt{2}\kappa_+} \times \left(\frac{\Gamma^2 + \gamma_*\Delta^2}{4\kappa_+^2}\right)^{-1/4}, \tag{C.15}$$

From this expression we obtain that for superconductivity to exist we must have that

$$V_{\text{int}} > \frac{2\sqrt{\kappa_+\Gamma}}{\pi N_S} \equiv V_{\text{min}}. \tag{C.16}$$

We then get for $V_{\text{int}} \geq V_{\text{min}}$ and $|V_{\text{int}} - V_{\text{min}}| \ll V_{\text{min}}$

$$\begin{aligned}\rho &\cong N_S v^2 \int_k \frac{4\Delta^2 E_k}{\left(E_k^2 + \Gamma^2/4\right)\left(4E_k^2 + \Gamma^2\right)} \\ &= N_S v^2 \Delta^2 \frac{1}{\kappa_+^3} \cdot \frac{\pi}{4\sqrt{2}} \left(\frac{\Gamma^2}{4\kappa_+^2}\right)^{-5/4} \\ &= v^2 N_S \Delta^2 \frac{1}{\Gamma^2\sqrt{\kappa_+\Gamma}} \cdot \frac{\pi}{4\sqrt{2}} \\ &\simeq \frac{\Delta^2}{2\sqrt{2}\Gamma^2} \frac{v^2}{V_{\text{min}}},\end{aligned} \tag{C.17}$$

the result presented in the main text.

C.3 Off-diagonal element of the distribution function

Finally, throughout the third chapter we assumed that we deal with a pure quasiparticle state. The general form of the distribution function in the quasiparticle basis,

$$\begin{pmatrix} n_{\underline{1}k} & \mathrm{OD} \\ \mathrm{OD}^* & 1-n_{\underline{2}k} \end{pmatrix} = \widehat{U} \begin{pmatrix} n_k^{11} & s_k^{12} \\ s_k^{12*} & 1-n_{-k}^{22} \end{pmatrix} \widehat{U}^\dagger, \tag{C.18}$$

have an offdiagonal element OD. We implied that OD = 0. Here we show that this statement is true. Using the definition of OD above, we get

$$\mathrm{OD} = \frac{1-n_{-k}^{22}-n_k^{11}}{2}\sin\beta + s_{12}\cos^2\frac{\beta}{2} - s_{12}^*\sin^2\frac{\beta}{2}. \tag{C.19}$$

Making use of the equations (3.19) and (3.20),

$$\begin{aligned} \mathrm{OD} = \frac{1}{4E^2+\Gamma_{12}^2+\gamma_*\Delta^2}\frac{N_{\mathcal{S}}}{2E_\Delta}\big(&-\Delta(4E^2+\Gamma_{12}^2)+ \\ &+4E^2\Delta+\mathrm{i}\Gamma_{12}\Delta\big), \end{aligned} \tag{C.20}$$

so that the offdiagonal element is indeed vanishingly small for energies larger than decay rate Γ_{12},

$$\mathrm{OD} = \frac{-\Delta\Gamma_{12}^2+\mathrm{i}\Gamma_{12}\Delta E_\Delta}{2E_\Delta(4E^2+\Gamma_{12}^2+\gamma_*\Delta^2)}N_{\mathcal{S}} \underset{\Gamma_{12}\to 0}{\to} 0. \tag{C.21}$$